Small-scale Fracture and Size Effects in Bioinspired Nanoarchitected Materials

Zainab S. Patel

A dissertation

submitted in partial fulfillment of the

requirements for the degree of

Doctor of Philosophy

University Of Washington

2024

Reading Committee:

Lucas R. Meza, Chair

Dwayne Arola

Eleftheria Roumeli

Marco Salviato

Program Authorized to Offer Degree:

Materials Science and Engineering

University Of Washington

Abstract

Small-scale Fracture and Size Effects in Bioinspired Nanoarchitected Materials

Zainab S. Patel

Chair of the Supervisory Committee:
Lucas R. Meza
Department of Mechanical Engineering

How do we make any material tough?

Fracture or premature failure is a pervasive issue across industries, materials, and length scales. While modern engineering approaches have developed effective methodologies to create damage-resistant materials, there remains a lack of fundamental understanding regarding the enhancement of a material's fracture resistance. Natural materials, composed of diverse and readily available constituents, exhibit exceptionally high damage tolerance and serve as model systems for understanding mechanisms of toughness amplification. However, true utilization of bioinspired strategies requires evaluating fracture behavior at the appropriate (small-scale) architectural length scales, a task that has not yet been thoroughly addressed. This work aims to bridge this gap by developing fundamental design principles that govern both intrinsic (material) and extrinsic (architectural) fracture size-effects, that can then be applied to imbue any material with enhanced fracture resistance.

This is accomplished by first developing a methodology to fabricate and test small-scale nanoarchitected materials via a combination of two-photon lithography, plasma etching, and in-situ nanomechanical testing. We first study how fracture behavior changes with sample size in polymers with varying degrees of crosslinking (DC) and find that ductility emerges

when the sample width approaches a characteristic fracture length scale, independent of DC. Subsequently, various nanoarchitected materials were developed, utilizing small-scale constituents and exhibiting increasing architectural complexity. Layered materials with 1D stiffness heterogeneity showed increased fracture energy and stable crack propagation with increasing layer spacing, without significant loss in strength and stiffness. Bouligand-style materials comprising polymeric nanofibers demonstrated enhanced toughness due to size-enhanced ductility and nanoscale stiffness heterogeneity. Lastly, interpenetrating lattices, composed of ductile and brittle sub-lattices, exhibited improved toughness and resistance to crack propagation, underscoring the role of feature size in exploiting size effects to create materials with unprecedented properties. This work demonstrates the creation of fracture-resistant nanoarchitected materials through nanoscale toughening mechanisms and highlights the potential for re-investigating the origins of fracture toughness and cascading damage mechanisms in hierarchical architectures to develop highly tough, damage-tolerant materials with properties akin to natural structural materials.

DEDICATION

To those who dare to step out and to the ones who have their backs

ACKNOWLEDGMENTS

The last six years have had some of the most fulfilling moments of my life, and it has been possible due to the collective efforts of a great many. First and foremost, I want to thank God for blessing me with this incredible life and the opportunity to pursue something so intellectually satisfying.

I am honored to be a part of the University of Washington, a remarkable institution where I've had access to some incredible resources and opportunities and the privilege to meet some amazing people. My time here was pivotal in forming the person I am today, and I am truly indebted to this beautiful place that I've been lucky to call my home.

My deepest gratitude goes to my advisor, Professor Lucas Meza for being such an incredible mentor and advisor. When I first talked to Lucas about joining his lab, I had very little understanding of the scientific world and could not really comprehend Lucas's stellar achievements, but what really struck me was his curiosity and kindness, and I am glad to say that has still not changed. Thanks for teaching me so much about how to do good science and for the freedom and support to pursue things that were meaningful to me. I admire your passion and dedication to doing rigorous science while being caring and conscientious. I leave your lab not just as a better scientist, but also as a better human being.

I am extremely grateful to Prof. Dwayne Arola, Prof. Eleftheria Roumeli, Prof. Marco Salviato, and Prof. David Bergsman for agreeing to serve on my thesis committee and for their time and feedback on my work. I am particularly grateful to Prof. Salviato, who has been so generous with his time and deep knowledge of fracture mechanics. Your timely

advice and input have made my work richer. Special thanks to Prof. Roumeli for always being such a great supporter and mentor, your enthusiasm and grit will continue to inspire me for years.

So much of what I have been able to do during my time here would not have been possible if so many people weren't so willing to help. I would like to thank the excellent staff at the Molecular Analysis Facility, Washington Nanofabrication Facility, and the Clean Energy Institute: Scott, Ellen, Micah, Jean, Sarice, Mark, and all the other people I've gotten help from over the years. Thanks to Tia for always promptly solving my hundred thousand payroll problems. Thanks to Karen for all your time and advice and for including me in so many department opportunities, I appreciate your commitment to being a great resource for all graduate students in the department. Thanks to Dr. Bryan Kaehr, Dr. Benjamin White, Dr. Brad Boyce, and Ian Good for being great collaborators and helping enhance the breadth and depth of our work I would also like to acknowledge the different funding sources that have made this work possible: UW Department of Mechanical Engineering, Center for Integrated Nanotechnologies Sandia National Labs (CINT), UW Molecular Engineering Materials Center (UW MEM-C), and the National Science Foundation (NSF).

Thank you to Prof. Vipin Kumar and Dr. Krishna Nadella for being great mentors when I first joined the UW and for their continued support over the years. Krishna, your grit, determination and the willingness to help everybody is inspiring and thanks for teaching me so much of how to be a good team player. Prof. Kumar, I appreciate the faith you have shown in me and thanks for being a great mentor and cheerleader all these years. To say that I am glad you saw something in me to select me for a research internship even after my denial of going to graduate school would be an understatement, it has changed the course of my life and I am incredibly grateful for that. Thanks also to Prof. Sudhir K Jain, Prof.

Reinhall, and Prof. Kumar for their time and efforts in keeping the IITGN-UW Summer internship program running for so many years, it has had an incredible impact on so many of us.

I want to thank all of my past teachers and mentors for helping me get to where I am today. Thanks to Giri Sir and Nirmal Sir for teaching with so much rigor and humor. Thanks to Professors Superb Misra, Amit Arora, and Manas Paliwal for not just teaching everything cool in MSE but also for being incredible mentors to step out into the world. Rita Ma'am, I don't quite have the words to express my gratitude to you. I can only say that I have reflected on everything you have taught me during my time at IITGN, and so much of it has helped me make sense of who I am. Thanks to Prof. Ambika Aiyadurai for introducing me to birding and laying the early groundwork for environmental conservation in my life. I'm beyond indebted to you.

It has been great to be part of the Meza group, and I want to thank all past and present members for their camaraderie. Thanks to Caelan, Robert and Kevin for creating such a fun environment when I first joined the group. Thanks to Nishita for being an amazing friend and lab partner through the dark COVID years, it was so great discuss anything and everything with you. Thanks to Aziz and Kush for being great collaborators and helping take our understanding of the nanotough world forward and special thanks to Aziz for helping me do those crazy marathon experiments, I still can't believe we managed to do as much as we did in a matter of 2 months!

Thanks to Sairandhri for ALWAYS being there for me from any corner of the world, having a friend like you makes life all the different. Thanks to Jan for helping me get out of the lab every weekend and for listening to all my long and short, interesting and sometimes pointless stories. You have been such a great friend, supporter, and cheerleader, my time

in Seattle has been so much better because of you. Thanks to Jugal and Ankita for being my second family here, so much of my love for MSE is because you two are in it. Thanks to Prasanna, Ekta, Rashmi, Chinmay, Akshay, Gaurav, Abbie, and Giang for helping make Seattle home. Special thanks to Kumud Aunty for the love, humor, and delicious food over the years.

Thank you to my family for their continued love, support, and encouragement. Thanks Pappa for always standing by me and motivating me to pursue challenging things. Thanks Mummy for teaching me to be brave and perseverant while enjoying life. Thanks Saku for being the best sister ever, and your belief in me makes all the difference. And while there is so much to say, I will only say that I could not have done this without all of your love and blessings, and this is as much your success as it is mine.

Finally, thanks Vasu for being my partner in everything. I cannot imagine this journey without you. From being my 'code troubleshooter' to 'what should I do for dinner' to 'should I just do this next week?', you somehow managed it all. I am grateful for your existence every single day.

Coffee, I love you and thanks for doing all of this work.

PUBLISHED CONTENT AND CONTRIBUTIONS

Chapter 2 has been adapted from:

1. Patel, Z. S., and Meza, L.R. "Toughness Amplification via Controlled Nanostructure in Lightweight Nano-Bouligand Materials." *Small* 19.50 (2023): 2207779.

   Contributions: Participated in the conception and design of the project, designed and fabricated samples, conducted experiments, analyzed data, and wrote manuscript.

Chapter 3 has been adapted from:

2. Patel, Z.S., Alrashed, A.O., Dwiwedi, K., Salviato, M., Meza, L.R., "Rethinking ductility—A study into the size-affected fracture of additively manufactured polymers." *Additive Manufacturing* (2024): 104113.

   Contributions: Participated in the conception and design of the project, designed and fabricated samples, conducted experiments, analyzed data, and wrote manuscript.

Chapter 4 has been adapted from:

3. Patel, Z.S., Alrashed, A.O., Good, I., Meza, L.R., "Tough, Strong and Lightweight Architected Materials from fracture size-effected constituents" (*In Preparation*)

   Contributions: Conceived the idea and designed the project, designed and fabricated samples, conducted experiments, analyzed data, and wrote manuscript.

Chapter 5 has been adapted from:

4. Patel, Z.S., Alrashed, A.O., Kaehr, B., White, B., Boyce, B., Meza, L.R., "Anistropic Fracture in Ductile and Brittle Nanoarchitected Interpenetrating Lattices" (*In Preparation*)

   Contributions: Participated in the conception and design of the project, designed and fabricated samples, conducted experiments, analyzed data, and wrote manuscript.

Not directly adapted in this dissertation:

5. D. Oki, K. Yamakawa, N. Paranjapye, L. Meza, C Wong, **Z. Patel**, G. Huang "Tensile forces in the neurovascular bundle: a contributor to orthodontic relapse?", *Orthodontics & Craniofacial Research*, 2023

   Contributions: Participated in the developing the experimental setup to conduct experiments, developed protocol for experiments, conducted preliminary experiments.

6. Wisont, C., Verdoes, R., Mulastham, A., Patel, Z., Meza, L., "Nanoarchitected Glassy Carbon Tensegrities with Controllably Introduced Prestress" (*In Preparation*)

   Contributions: Conducted experiments.

TABLE OF CONTENTS

LIST OF FIGURES

LIST OF TABLES

Chapter 1

INTRODUCTION

Fracture toughness characterizes a material's energetic resistance to growing an existing crack and defines a material's durability, flaw tolerance, and capacity for long-term use. Advanced technologies demand materials that are not only strong and stiff but also lightweight, multifunctional, and, most importantly, tough since poor material toughness negatively impacts technologies from biomedical implants [116, 99, 101] to renewable energy applications like solar cells, thermoelectrics, and batteries [38, 77, 82]. In principle, increasing toughness corresponds with increasing the number of ways a material can 'spend' its energy during deformation, also referred to as 'toughening mechanisms'. From a materials engineering perspective, this is often achieved by turning to composite materials that can activate new mechanisms to increase the energetic cost for a crack to grow through a material (Figure 1.1), a strategy routinely exemplified by Natural structural materials. Developing the next generation of advanced materials using biology as a model system first requires understanding how we define fracture and what governs deformation in such complex material systems.

1.1 A Brief History of Fracture Mechanics

Fracture mechanics studies how cracks propagate in a material and has its origins in Griffith Theory (1920/1924) [49, 50]. When faced with premature failure in glass at stresses ∼100x lower than its strength, Griffith ascribed this behavior to invisible defects in glass and derived a theory for the brittle fracture of solids. Given the mathematical challenges of stress singularity (the state of infinite stress) at the crack tip, Griffith adopted an energetic ap-

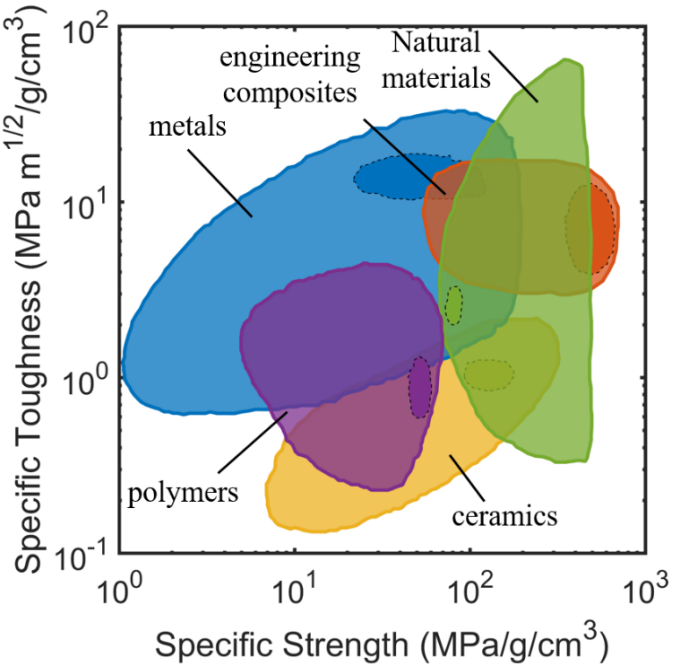

Figure 1.1: Ashby plot showing the strength and fracture properties of common engineering and natural materials. Adapted from [78].

proach and proposed that the toughness of material under loading is a competition between the decrease in the stored elastic energy and the energy gained by creating new surfaces from a preexisting flaw or crack. Irwin and others[1] found that this toughness, defined as the strain energy release rate ($G = 2\gamma$), where γ is the surface energy, only applies to brittle materials and falls short for ductile materials [61, 103]. This is because ductile materials develop a non-negligible inelastic zone ahead of the crack tip that dissipates energy during fracture that is not accounted for in Griffith's proposed expression. In the late 1940s, Irwin and Orowan included this energy dissipation to derive the strain energy release rate and also reformulated the stress singularity problem at the crack tip by introducing the stress

[1]This is a very condensed history highlighting the contributions of a select few. To get a more comprehensive understanding, I refer the reader to this excellent review by B. Cotterell, 'The past, present, and future of fracture mechanics' [35]

intensity factor (K). This provided an alternative approach to describe crack propagation: crack growth occurs when K, defined by the magnitude of the local stress (σ) and the size of the flaw(a) ($K = \sigma\sqrt{2\pi a}$), exceeds a critical value of the stress intensity factor, denoted as K_{ic}, a material property, laying the foundation of today's linear elastic fracture mechanics (LEFM).

One key requirement for this proposed LEFM definition to work was that the sample be significantly larger than the size of the inelastic deformation zone so that the bulk of the material could still be treated as purely elastic. In the years that followed, Rice (and others) addressed LEFM's shortcomings to account for the significant plastic deformation in front of the crack and in 1968 formulated a generalized energy release rate for nonlinear material behavior: a *J-integral* [117, 118]. The *J-integral* is another way to determine the strain-energy release rate by using a contour path integral that is independent of the path around the crack. Similar to G, it could be utilized to describe the stress state at the crack tip for any elastic-plastic material, leading to the development of elastic-plastic fracture mechanics (EPFM). Together, these works build the foundation of standards developed for fracture toughness and the design of damage-tolerant components that are still used to date.

Since the majority of EPFM-based fracture mechanics was developed for ductile metals, the inelastic zone was considered to be equivalent to the plastic zone (PZ). But observations in size-affected changes in failure behavior even in materials typically considered to be brittle, led to the development of another kind of fracture mechanics, called quasi-brittle fracture mechanics (QBFM), in the 1980s. Quasi-brittle fracture primarily describes fracture in materials that have a finite fracture process zone (FPZ), where the material is undergoing strain softening not accounted for by EPFM and where this FPZ is significantly larger than the PZ.

It is important to note here that despite the fact that EPFM and QBFM now account

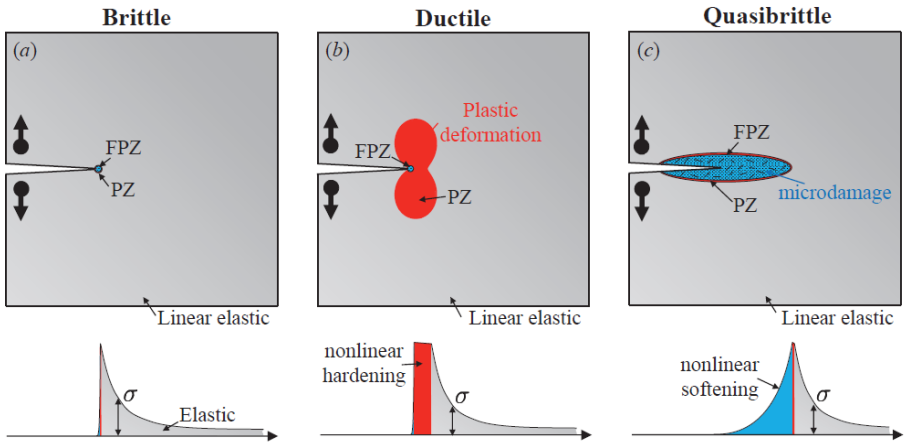

Figure 1.2: Types of Fracture Behaviors. Adapted from [25]

for a considerably sized inelastic zone ahead of the crack, they still require structures to be larger than the size of these inelastic zones to accurately quantify toughness. For structures smaller or comparable to this inelastic zone, J or G only represent a fraction of the plastic work. Thus, fracture of small-scale [2] structures is not well quantified and even less well understood, a point we will come back to repeatedly in this dissertation. **It will suffice to say for now that this presents an enormous opportunity to exploit these unique fracture phenomena in the design of new materials.**

1.2 Natural Structural Materials

We now turn to the world of natural materials to understand what salient features result in their exceptional properties. Natural materials in both plant and animal species are known to have unique combinations of strength and toughness despite being made from a limited selection of available materials [72, 120, 130, 47, 46]. They achieve this using com-

[2] Here, small does not refer to the absolute length. It can be read as sufficiently small, meaning the structure size is smaller than the size of the inelastic zone. For ceramics, this can be on the order of 10-100 nm, 0.5-500 μm for polymers, and several mms for metals.

plex, multi-material, hierarchical architectures that have controlled features spanning from the nanoscale to the macroscale [58, 134, 96]. For instance, bone, a characteristic example of a load-bearing biological structural composite, combines low weight, high strength, high toughness, and self-healing capability. At the nano-molecular length scales, it is composed of collagen molecules, which combine to form helicoidal tropocollagen fibrils reinforced with nanocrystalline hydroxyapatite. The fibrils combine and form fiber bundles, which then form a microscale lamellar structure with a mineralized matrix as seen in Figure 1.3 [72]. Typically, ceramics are associated with high strength but low fracture toughness and polymers are associated with low strength but high fracture toughness. Natural materials like bone combine small volume fractions of high-strength crystalline phases with large volumes of high-toughness (and lightweight) polymeric phases in complex architectures to obtain effective properties greater than predicted by the rule of mixtures [78]. Upon application of a load, structural components at every length scale resist damage and deform to dissipate a significant amount of energy before fracture It is this hierarchical design of natural materials from the nanoscale up that enables them to utilize the intrinsically high strength of nanomaterials and introduce various intrinsic and extrinsic toughening mechanisms across multiple length scales.

One notable class of tough natural materials explored in this dissertation is the exoskeletons of arthropods such as lobsters, crabs, and mantis shrimp, which consist of highly aligned chitin nanofibril laminae reinforced with nanocrystalline hydroxyapatite [106, 133, 34]. The laminae are arranged in a Bouligand stacking [27] wherein each layer is rotated by a fixed angle with respect to the layer below it to produce a helicoidal microstructure. Nanoindentation experiments have revealed extensive crack twisting as the crack propagates through the periodic region of the mantis shrimp. Helicoidal stacking creates a much larger surface area per unit crack length in the main direction of propagation, hence amplifying the total energy

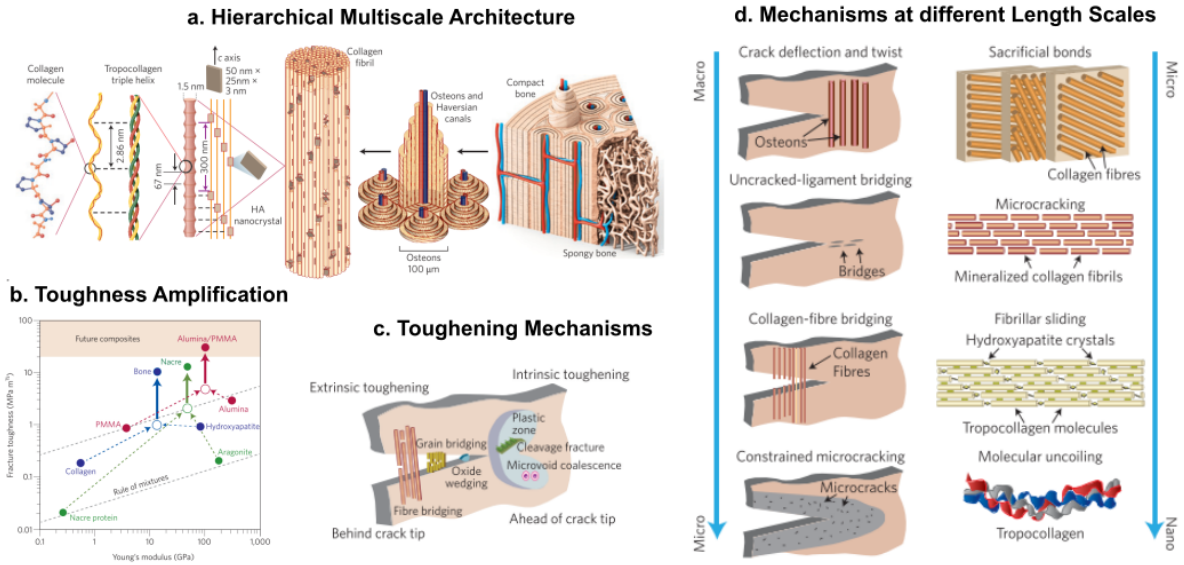

Figure 1.3: **Architecture, composition, and emergent toughening in Natural Materials:** (a) Complex hierarchical architecture in a bone specimen from the nanoscale up [32]. (b) Ashby plot illustrating increment in toughness beyond the rule of mixtures [134]. (c) Intrinsic and extrinsic toughening mechanisms due to nanoscale materials and architecture in natural materials[119]. (d) Mechanisms of toughening at different length scales depending on hierarchy [72].

dissipated during impact and crack propagation. Crack deviating from a helicoidal path into the neighboring layers encounters an elastic modulus oscillation (anisotropic stiffnesses) which provides an additional protection against damage. These exoskeletons also contain many pores, either in the form of tubules that run through their thickness [34] or as elliptical voids between fiber bundles [145]. Another notable material is the egg case of swell sharks, which is one of the toughest permeable membranes known and consists of Bouligand-like nanoribbon lamellae that are part of a larger nanolattice architecture [47]. In all these materials, the angular misorientation between layers, modulus mismatch between constituent materials, and the presence of voids, pores, or tubules activate toughening mechanisms like crack twisting, crack blunting and crack arrest, making them extremely damage-tolerant

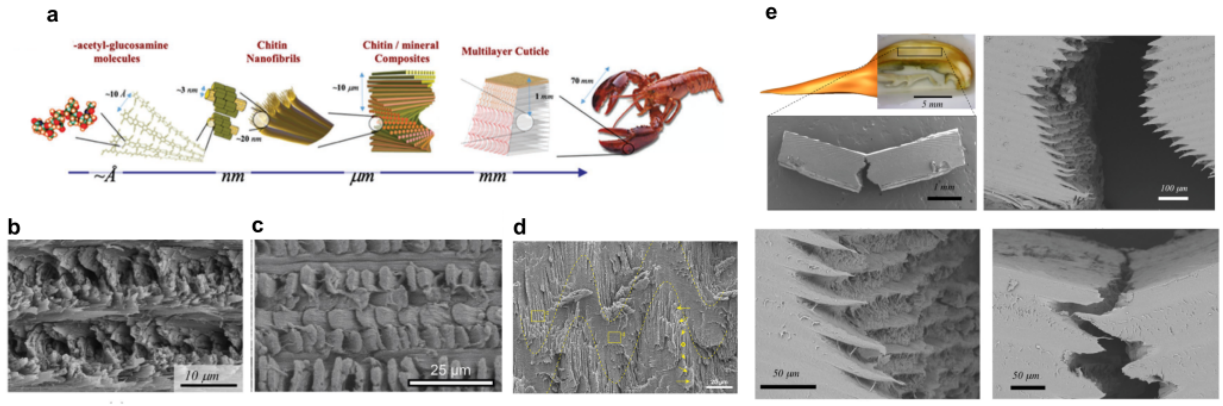

Figure 1.4: **Bouligand Architectures in Nature** (a) Hierarchical architecture in the dactyl club of the mantis shrimp [100]. (b),(c) and (d) are the single, double and herringbone bouligand architectures respectively, as found in different sea organisms [133, 146, 144]. (e) Extensive crack twisting observed in the dactyl club of a mantis shrimp [128].

[133, 97].

There are multiple structural variants of the bouligand style architecture, of which we are focusing on the single, double and herringbone architectures, where the latter two are modifications of the former. The double bouligand structure is much rarer and found in the elasmoid scales of Chordata fish [146]. It uses the orthogonal bilayer as a unit to further form the twisted plywood structure. The array of fibrils perpendicular to the laminate structure, mainly along the thickness direction, called the interbundle fibrils, holds the structure together and keeps the bilayers from separating. The herringbone bouligand, on the other hand, has wavy, double sinusoidal fibers. Triaxial stress states in both the double bouligand and the herringbone structures give rise to complex crack growth morphologies and increase the total energy dissipated during fracture.

1.3 Tough Bioinspired Architected Materials

Modern fabrication techniques and testing methods have enabled the design and characterization of engineering materials with features similar to natural materials. Techniques like multi-material additive manufacturing, freeze casting, and self-assembly have been used to create bio-inspired architectures like topologically interlocked lattices or tiles [92, 53], nacre-like (brick and mortar) microarchitectures [95, 29], soft/weak inclusions or defects [79, 91] and twisted (Bouligand) architectures [128, 146] (Figure 1.5). These materials activate toughening mechanisms like crack-twisting, crack-deflection, fiber pullout, and constrained microcracking [128, 30, 80, 91, 53], akin to natural materials [3], and can be considerably tougher than their constituents.

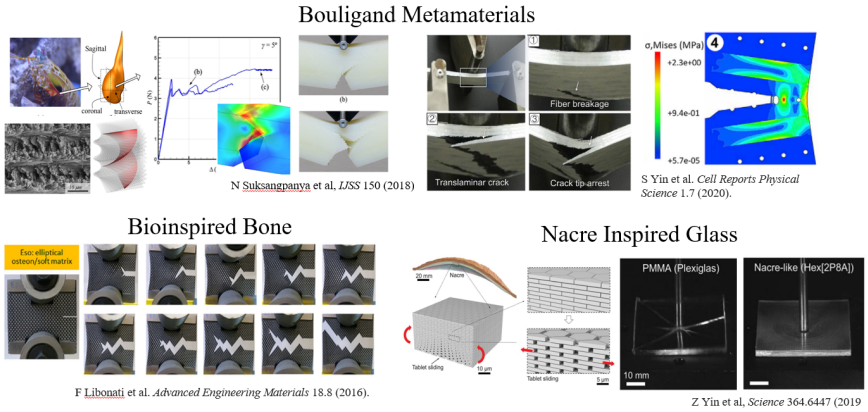

Figure 1.5: **Bioinspired Toughness:** (a) Crack twisting with increasing bouligand twist in multi-material polymer bouligand structures and glass fiber composite beams [128, 146]. (b) Bone-inspired materials showing crack deflection [79]. (c) Nacre inspired glass showing distributed micro-cracking and damage tolerance [91].

While they draw inspiration from nature, they largely ignore the role of length scale on fracture. A key constituent for the exceptional behavior of natural materials is hypothesized

[3] Interested readers are referred to 'Advanced Structural Materials by Bioinspiration' [78] by F. Libonati and M. Buehler for a more comprehensive understanding.

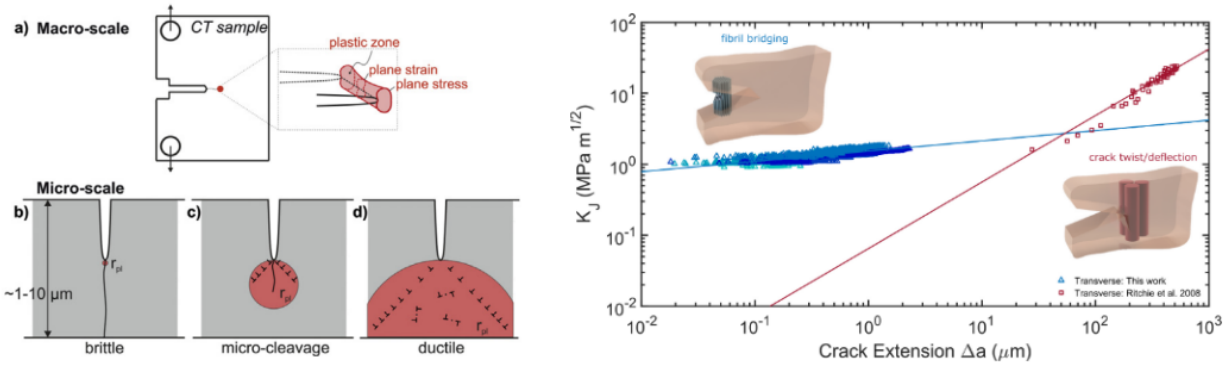

Figure 1.6: **Microscale Fracture and Size Effects.** (a) Shape and size of the plastic zone ahead of the crack tip in different materials and it's implications on microscale fracture testing [8]. (b) Scaling of Toughness in bone hierarchy showing toughness amplification at the nanoscale due to fibril bridging [129].

to be its nanoscale building blocks, which utilize unique size-affected material properties. Moreover, since fracture processes at different length scales contribute differently to the effective toughening of the material, true bioinspired design necessitates bottom-up fabrication with comparable feature sizes and fracture characterization at appropriate length scales. On the fabrication end, for a long time this was limited by the lack of suitable techniques. Emerging micro and nanoscale additive manufacturing methods in combination with thin film deposition and pyrolysis techniques have now been used to create novel nanoarchitected materials that utilize enhanced strength at the nanoscale to make incredibly strong, lightweight and flaw tolerant materials [87, 64, 14, 94, 147, 111]. This successes in high-strength and tough-architected materials, now demands a systematic investigation into the role of nanomaterials and nanoarchitecture in toughness at small length scales.

1.4 Small-scale Fracture

Fracture experiments are standardized for the macroscale, where sample dimensions can be significantly larger than the characteristic fracture process zone (FPZ) and plastic zone (PZ) sizes, and linear elastic fracture mechanics (LEFM) assumptions like K-field dominance can be made. Fracture analysis at the micro/nanoscale is complicated by the inherent material length scales and size effects involved in fracture processes [22, 113, 8]. At the microscale, sample sizes can approach or become smaller than the FPZ or PZ size of the material, especially in metals and polymers. This makes it complicated to perform analysis, let alone adapt new standards, for toughness measurements [65, 109, 9]. Fracture testing has been reported on notched microscale beam samples, but asymmetric loading conditions at the notch tip of individual cantilevers limits the viability of these techniques, especially for heterogeneous materials [3, 140, 9, 123]. The development of reliable experimental and theoretical frameworks to measure small-scale fracture properties will help to verify size effects in fracture that have been studied either theoretically or at the macro-scale [22, 26, 131]. It is also significant for understanding spatially varying properties of natural, heterogeneous materials, such as in recent work by Tertuliano et al. [129] showing the effect of nanoarchitecture on flaw tolerance in bone.

1.5 Outline and Objectives

This dissertation focuses on the intrinsic length scales that govern fracture in different materials and explores how they can be utilized in bioinspired architectures to develop the next generation of damage-tolerant materials.

Chapter 2 focuses on quantifying the individual roles of nanomaterials and nanoarchitecture on toughness. We fabricate a novel nanoarchitected material made with a Bouligand stack of nanofibers (nano-Bouligand) with minimum feature sizes and architectures compa-

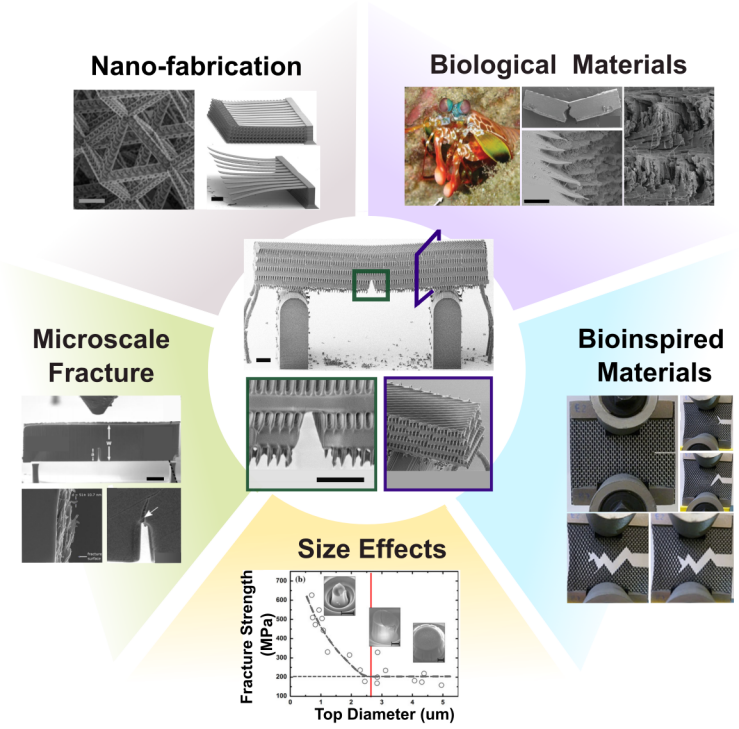

Figure 1.7: Strategy to develop the next generation of damage tolerant materials [133, 128, 80, 131, 129, 89, 51].

rable to those found in natural materials and develop a methodology to mechanically test small-scale toughness and elucidate the emergent nanoscale toughening mechanisms. We show that the size-enhanced ductility of isolated nanofibers in low-density materials, along with the nanoscale stiffness heterogeneity in twisted materials, both act as independent toughening mechanisms. More broadly, toughness at the nano/microscale is not an "intrinsic" material property, but it can be affected by molecular or nanoscale heterogeneity in a unique and controllable way.

Chapter 3 focuses on understanding the mechanistic origins of enhanced ductility at small scales. We fabricate μ-scale beams with varying degrees of polymer crosslinking and study how fracture behavior changes. This is combined with an elastic-plastic-damage numerical

model and size-effect experiments to quantify the length scales at which ductility is activated in different materials. We show that ductility is a size-induced property that occurs when features are reduced below a characteristic fracture length scale and that strength, stiffness, and toughness alone are insufficient predictors of ductility.

Chapter 4 focuses on utilizing the idea of size-enhanced ductility to create size-controlled architected materials. We develop μ-layered polymeric beams with features smaller than the material's fracture yielding zone and study how fracture changes with increasing architectural complexity. We show that architecture enables the preservation of size-effects and that architected materials with sufficiently small feature sizes not only show significant toughness amplification but also prevent catastrophic failure.

Chapter 5 focuses on toughening in nano-interpenetrating lattices, primarily to explore how materials with different fracture-yielding zones can be combined to enhance toughness. We develop nano-interpenetrating lattices with features smaller and larger than the fracture-yielding zone and study how fracture changes. We show that the creation of an interpenetrating architecture prevents catastrophic failure, but similar to the layered materials in Chapter 3, the creation of sufficiently small interpenetrating lattices fundamentally enhances damage tolerance.

Chapter 6 offers a concise summary of the investigations of this dissertation, as well as an outlook and other research directions in the size-controlled bioinspired design of tough materials.

Chapter 2

NANO-BOULIGAND ARCHITECTED MATERIALS

This chapter has been adapted from:

Patel, Zainab S., and Lucas R. Meza. "**Toughness Amplification via Controlled Nanostructure in Lightweight Nano-Bouligand Materials**." Small 19.50 (2023): 2207779.

Contributions: Designed and fabricated samples, conducted experiments, analyzed data, and wrote manuscript.

2.1 Chapter Summary

The enhanced properties of nanomaterials make them attractive for advanced high-performance materials, but their role in promoting toughness has been unclear. Fabrication challenges prevent the proper organization of nanomaterial constituents, and inadequate testing methods have led to a poor knowledge of toughness at small scales. In this chapter, we quantify the individual roles of nanomaterials and nanoarchitecture on toughness by creating lightweight materials made from helicoidal polymeric nanofibers (nano-Bouligand). Unidirectional (θ = 0°) and nano-Bouligand beams (θ = 2° - 90°) were fabricated using two-photon lithography and designed in a micro-single edge notch bend (μ-SENB) configuration with relative densities $\overline{\rho}$ between 48% to 81%. Experiments demonstrate two unique toughening mechanisms. First, size-enhanced ductility of nanoconfined polymer fibers increases specific fracture energy by 70% in the 0° unidirectional beams. Second, nanoscale stiffness heterogeneity created via inter-layer fiber twisting impedes crack growth and improves absolute fracture

energy dissipation by 48% in high-density nano-Bouligand materials. This demonstration of size-enhanced ductility and nanoscale heterogeneity as coexisting toughening mechanisms reveals the capacity for nanoengineered materials to greatly improve mechanical resilience in a new generation of advanced materials.

2.2 Background

Structural materials must not only be strong, stiff, and lightweight but also resistant to fracture (i.e., tough), properties that are difficult to obtain simultaneously. Nanomaterials are known to have unique properties such as size-enhanced strength, flaw tolerance, and ductility [44, 48, 6, 105, 37], but there are few engineering examples where nanomaterials engender both strength and toughness in a material. Natural materials in both plant and animal species have noteworthy combinations of strength and toughness despite being made from a limited selection of available materials [72, 120, 130, 47, 46]. It is hypothesized that their hierarchical architectures comprising precise nano-, micro-, and meso-structures enables them to utilize the high strength of nanomaterials while introducing toughening mechanisms across multiple length scales [58, 134, 96]. One notable class of tough natural materials is the exoskeletons of arthropods such as lobsters, crabs, and mantis shrimp, which consist of highly aligned chitin nanofibril laminae reinforced with nanocrystalline hydroxyapatite [120, 106, 133, 52, 145, 137]. The laminae are arranged in a Bouligand stacking [27] wherein each layer is rotated by a fixed angle with respect to the layer below it to produce a helicoidal microstructure. Similar architectures can be found in soft materials, e.g. the egg cases of swell sharks [47]. The angular misorientation between layers, modulus mismatch between constituent materials, and the presence of voids, pores, or tubules activate toughening mechanisms like crack twisting, crack blunting and crack arrest, making them extremely damage-tolerant. While these materials serve different functions – shells have a higher min-

eral content for increased strength, and egg cases have a low density to be semi-permeable; it is apparent that their architecture enables extreme flaw tolerance and activates toughening mechanisms across multiple length scales. Work on the fracture and impact behavior of bioinspired Bouligand materials has successfully replicated toughening mechanisms like crack twisting and blunting, demonstrating the high fracture resistance of this architecture and providing a mechanistic understanding of the key design features contributing to this enhanced damage tolerance [138, 112, 146, 93]. This principle of architected toughness thus has great promise for guiding the design of novel high-strength, fracture-resistant materials, but implementing it first requires understanding how structural hierarchy, particularly at the nanoscale, affects toughness.

2.3 Bioinspired Design

We develop a new class of nanoarchitected materials comprising polymeric nanofibers that exploit both nanomaterials and nanostructure to enhance their toughness. To decouple the unique contributions of nanomaterial size-effects and nanoarchitecture, we create two distinct nanostructural designs. First, we created beams with unidirectional fibers and varying inter-fiber distances. The altered fiber spacing causes fibers to either bridge (i.e. join together) or remain separate, allowing for control over the nanoconfinement in each layer and thereby controlling the material level ductility. Second, we introduced a Bouligand-style architecture, where the fibers in each layer are twisted by a fixed angle from the adjacent layer. These helicoidal stacks of twisted polymeric nanofibers enable the creation of a complex 3D spatial variation of material stiffness with minimum feature sizes and architectures comparable to those found in natural materials (Figure 2.1)

Microscale beams were designed with Unidirectional and Bouligand-type nanoarchitectures that have a controllable relative density ($\overline{\rho}$) and twist angle between layers (θ) [28].

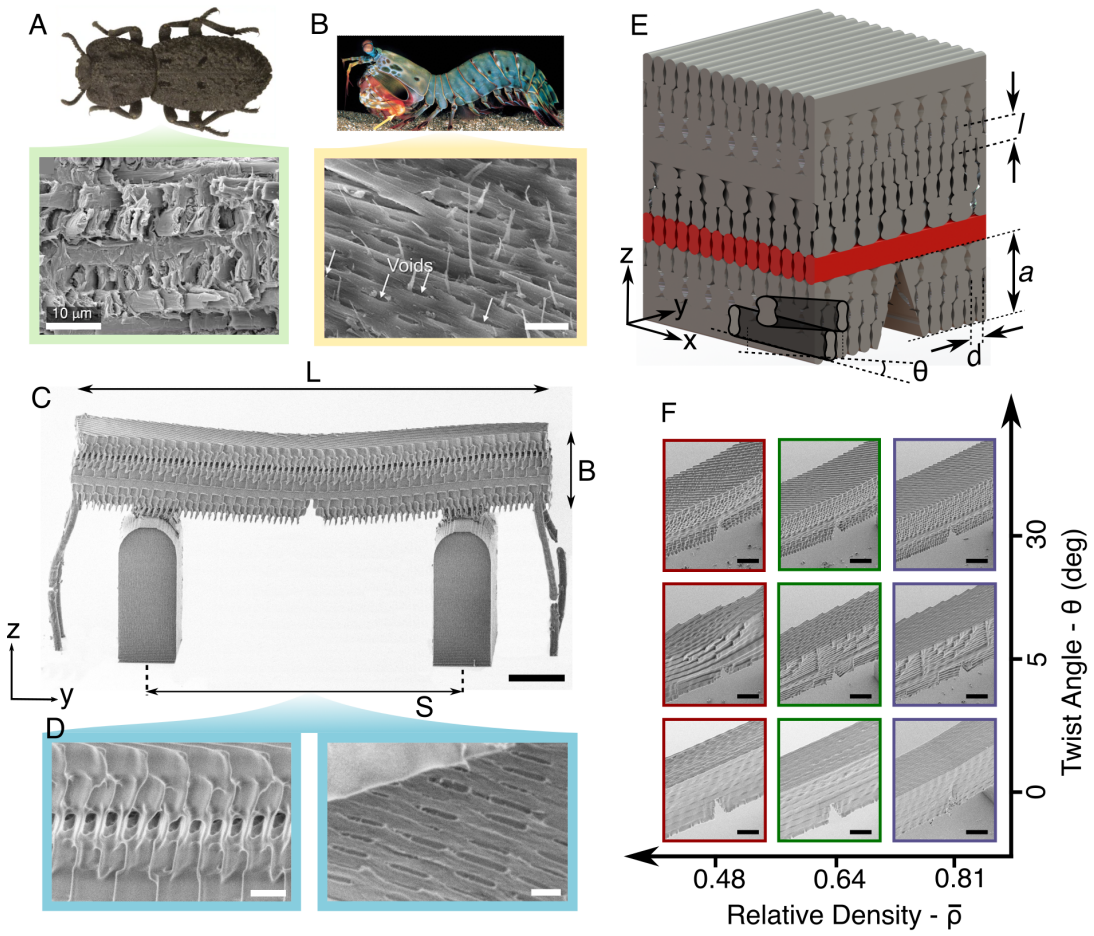

Figure 2.1: **Design of Nanobouligand beams.** (A) Scanning electron microscope (SEM) image of the endocuticle of the diabolical ironclad beetle, showing helicoidal fibre orientation with a ∼30–60° rotation per layer [120] (Scale bar: 10 μm). (B) SEM image of the cross-section of a 'smasher-type' mantis shrimp dactyl club showing microscale voids [106, 145] (Scale bar: 2 μm). (C) SEM image of a free-standing μSENB specimen of a LD-30° beam(Scale bar: 10 μm). (D) Close-up of the nano-Bouligand architectural features made in this study, similar in design and scale to natural materials shown in (A) and (B). (Left) Front view of a LD-30° beam. (Right) Fracture surface of the MD-0° beam with elliptical voids (Scale bar: 2 μm). (E) Computer-aided design (CAD) of the nano-Bouligand beam showing the hatching (d), layering (l), and twist angle (θ) design parameters. (F) Design space showing SEM images of beams of varying relative density and twist angle (Scale bar: 5 μm).

The nanofibers that make up these materials have a major and minor axis equal to ∼1650 nm and ∼480 nm, respectively. The high laser exposure during fabrication results in the voxel having a slightly hyperbolic (peanut-shaped) cross-section rather than an elliptical one, as has been shown in other work [15]. The center-to-center distance between layers (l) is set equal to 1500 nm in all beams, creating a minimum overlap (δ) equal to 150 nm between two layers, as seen in Figure 2.1. In plane center-to-center distances between the fibers (d) = 600 nm, 800 nm, and 1000 nm were used, resulting in beams with relative densities of $\overline{\rho} \approx 81\%$, 64%, and 48%, respectively. For simplicity, these densities will be referred to as High-Density (HD), Medium-Density (MD), and Low-Density (LD), respectively. The twist angle (θ) is explicitly defined for each layer, and beams of every relative density are written with θ = 0°, 2°, 5°, 15°, 30° and 90°. Taken together, samples will be referred to using a '$\overline{\rho}$-θ' designation, meaning an 'HD-30' sample would have an 81% relative density and a 30° twist angle. Relative density calculations were made using CAD renderings of the material. Modeled voxel dimensions were measured from SEM images and bridging zones were incorporated to account for the additional cross-linking at layer intersections that occur due to proximity effects. Given the voxel size uncertainty and variation in bridging zone size, it is estimated that the calculated relative densities have a variance of ±5%, and introducing a twist causes less than 0.8% variation in the relative density.

Specimens were designed in a single edge notch geometry and written in a 3-point bend configuration for testing. All beams consisted of 9 twist layers, giving a total beam thickness B=13.5 μm. Beam dimensions were determined based on the required specimen aspect ratio defined in ASTM E1820-20b [59], where $1 \leq W/B \leq 4$ and $S = 4W$, where W is the specimen width and S is the span length. Notches were directly written into the beams during the printing process to avoid introducing any focused ion beam (FIB) milling damage during specimen preparation [8]. The notches were written in the first three layers of the beams,

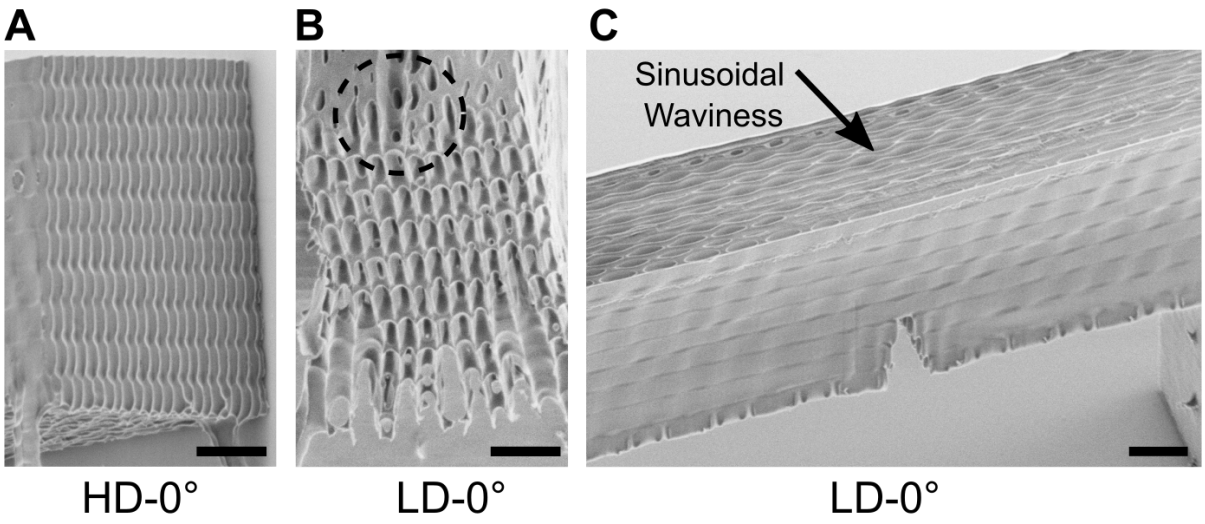

Figure 2.2: **TPL artifacts in the nano-Bouligand beams.** (A) Side view of the HD-0° beam. (B) Side view of LD-0° beam showing fiber overlap between layers-helping in maintaining the integrity of the structure. (C) Front view of the LD-0° beam showing sinusoidal waviness produced due to system vibrations. (Scale bar in all images: 5 μm)

causing them to have a length of $a \approx 4.5$ μm. All beams were designed such that the 0° layer intersects the tip of the notch; which allowed the results from different architectures to be compared directly.

2.4 Methods

2.4.1 Fabrication

The entire three-point bend assembly and the nano-Bouligand beams are designed in Python and imported into Photonic Professional DLW system (Nanoscribe GmbH). Specimens were fabricated on silicon substrates, which were first etched for 5 minutes in oxygen plasma (Plasma Etch - 25 system) and then functionalized using 3-(Trimethoxysilyl) propyl methacrylate to improve adhesion and prevent peeling off of supports during fracture tests. Subsequent writes were done using two-photon lithography (TPL) direct laser writing (DLW) system

(Nanoscribe, GmbH). A proprietary acrylate-based resist, IP-Dip (Nanoscribe, GmbH), was used with a 63x objective to obtain high-precision sub-micron resolution writes.

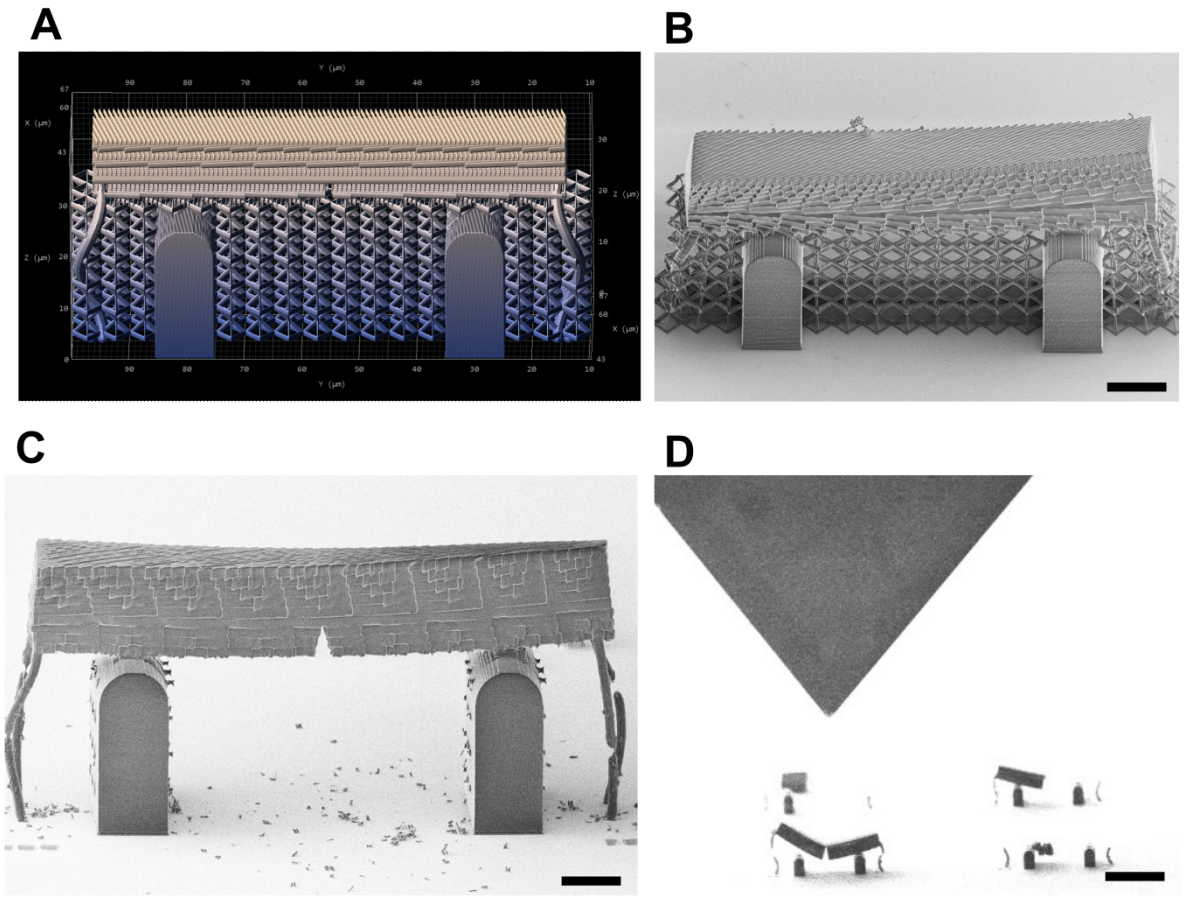

Figure 2.3: **Fabrication procedure to produce free-standing micro-single edge notch bend (μSENB) specimens with nano-Bouligand beams.** (A) DeScribe rendering of the nano-Bouligand beam setup designed using a custom Python script. (B) As printed sample with support lattices and solid springs (Scale bar: 10 μm). (C) Post etching and FIB milling of springs (Scale bar: 10 μm). (D) In-situ nanomechanical testing with the conductive diamond wedge tip (Scale bar: 50 μm).

Nano-Bouligand samples were written using a slower piezo-control mode which gives high-precision writes. Laser power and scanning speeds were adjusted to 56 mW and 50 μm/sec,

respectively to obtain a final voxel width of 480±50 nm width and 1650±50 nm height. The three-point bend supports and springs were written using the faster galvanometric scan mode with a finer hatching and layering to produce stiffer structures. The support lattices were written using the piezo mode with the lowest laser power (6 mW) to ensure faster etching. Printed structures were immersed in a propylene glycol monomethyl ether acetate (PGMEA) solution for 20 mins, then in ultrapure IPA for 30 mins followed by critical point drying (Autosamdri-931 system Tousimis). These were subsequently etched in a downstream oxygen plasma etcher (YES CV200 RFS downstream etcher) at 45°C with 65 W power, a pressure of 760 millitorr, and 100 SCCM O_2 flow [51]. Springs supporting the beam were milled using a focused ion beam (FIB) (FEI XL830) at 70 pA beam current for 30 seconds to produce free-standing three-point bend specimens. Figure S2 illustrates the fabrication method to produce free-standing micro-single edge notch bend (μSENB) specimens.

2.4.2 Nanomaterial Properties

The mechanical properties of any photopolymer depend strongly on the degree of conversion (DC) of the material, i.e, the amount of cross-linking between polymer chains. In a TPL process, this cross-linking density varies both through the part and across the width of an individual voxel, resulting in complex spatial property gradients that depend on the degree of laser exposure and the hatching and layer spacing of the voxel lines. The effect of DC on feature size, voxel shape and mechanical properties of the acrylate-based resist used here has been thoroughly characterized in work by Bauer et al. [15]. The size of the voxel depends roughly on the power that the material is exposed to and, for the materials and process used here, can vary from 150nm-650nm in width. The shape of a single voxel made using TPL has an elliptical cross-section at low powers but can shift to a slightly hyperbolic (peanut-shaped) cross-section at higher powers.

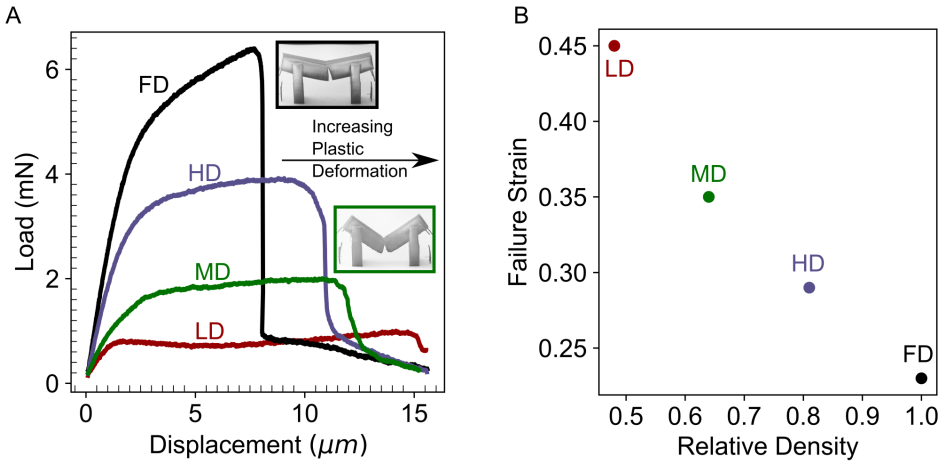

Figure 2.4: **Variation in Plastic deformation with beam density**. (A) Load vs displacement data from bend tests on un-notched FD, HD, MD and LD-0° beams showing 2x increase in flexure strain in the LD-0° beam. (B) Failure strain vs relative density demonstrating ≈ 2x increase in strain to failure in LD samples with isolated nanofibers as compared to fully dense samples with fully bridged fibers.

In this work, the higher laser power used results in this type of hyperbolic voxel and causes fibers to bridge toward their ends, forming a weakly cross-linked bridge between layers (Figure 2.1). The relationship between Young's modulus and yield strength on DC have been measured to be as $E = (9.52 * DC - 0.56)$ GPa and $\sigma_y = (170.36 * DC - 0.84)$ MPa [15]. Based on the parameters used here, this corresponds to a stiffness and strength of the fiber core (center of the voxel) of $E_{max} \approx 3.9$ GPa and $\sigma_{y-max} \approx 79$ MPa, while the weakly cross-linked bridges may have properties of $E_{min} \approx 1.3$ GPa and $\sigma_{y-max} \approx 35$ MPa. It should be noted that within a single voxel, the cross-linking density can vary by as much as 30% in a 100nm distance [66], resulting in significant local property gradients. We additionally conducted direct bend measurements on Unidirectional beams to quantify the strain to failure of the layers (Figure 2.4). We found a strong dependence of the failure strain on the relative density, with $\varepsilon_f \approx 0.23$ for the fully dense beams and $\varepsilon_f \approx 0.45$ for the

low-density beams with more isolated fibers. This nanoconfinement induced ductility is a key feature that bestows toughness to the low-density materials studied here.

2.4.3 Mechanical Testing

In-situ fracture tests were performed using the displacement-controlled mode in an Alemnis ASA nanoindentation system. Specimens were tested either to complete fracture or to a displacement of 14 μm and video data was captured for each test, representative stills of which are shown in Figure 2.5. Instantaneous load line stiffness was calculated using the unloading slope of the CSM data, and crack initiation was determined as the point where the unloading stiffness began to decrease. Crack lengths were obtained using a compliance calibration procedure [55] by correlating the crack initiation point with the instantaneous stiffnesses thereafter. The tool was installed in a Thermo-Fisher Scientific Apreo SEM, and testing was done with a 2 μm radius conductive diamond wedge tip. A loading rate of 20 nm/sec was used and beams were taken to 14 μm piezo displacement. A sinusoidal signal of amplitude 40 nm and frequency 4 Hz was superimposed to perform continuous stiffness measurement (CSM) and thereafter compute instantaneous crack lengths. All test videos were recorded using a 300 ns refresh time and 2 frame integration.

Load measured during nanomechanical testing always contains some thermal drift, which increases with time. To account for this, we kept the nanoindenter assembly installed for a time greater than 12 hours prior to testing for the drift to stabilize. We additionally added 'out-of-contact' segments before and after the compression step where the tip is not in contact with the sample to correct for any drift in the system. Thermal drift showed linear correlation with time for short experiment times (less than 30 minutes) and was subsequently subtracted from the load data during data processing. μ-SENB nano-Bouligand samples were soft and their peak load was close to the load limit of the tool, hence the CSM data was noisy,

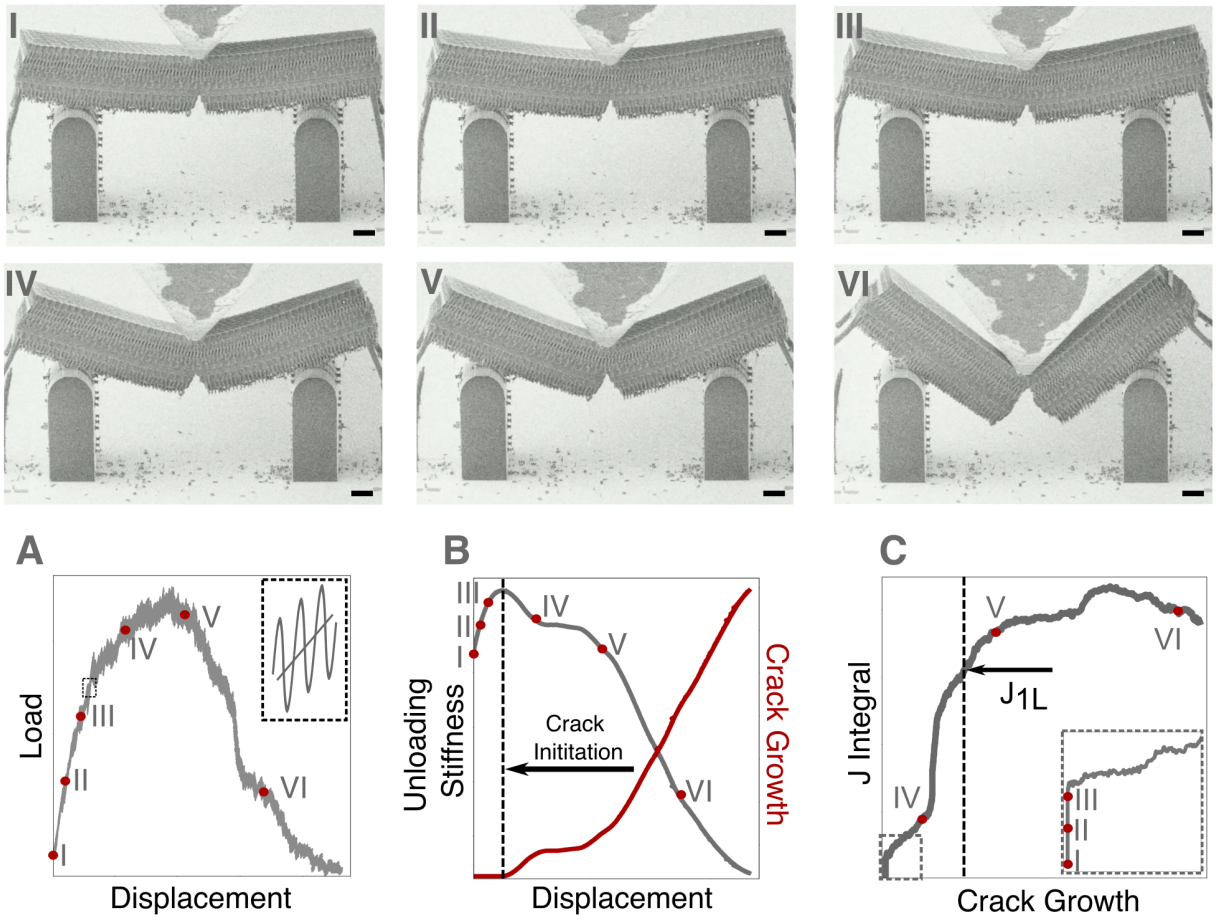

Figure 2.5: **Representative crack growth and J-integral data**. *I-VI* are representative stills from an in-situ fracture test on an MD-30° beam showing crack initiation and propagation with increasing tip displacement (Scale bar: 5 µm). (A) Load-displacement data with inset showing the applied sinusoidal displacement for CSM. (B) Unloading stiffness (gray) calculated from the unloading slopes of the CSM data and the corresponding crack lengths (red) obtained via compliance calibration. Crack initiates after III, as seen by the drop in stiffness. (C) J-integral calculated using [59] exhibits a rising behaviour indicative of extensive toughening.

particularly for the LD samples. Since the noise in the CSM data can significantly affect the computation of crack lengths and J-curves, an amplitude based Fast Fourier Transform (FFT) noise filtering algorithm was applied on the load-displacement data. Subsequent CSM

Data was smoothed using the Savitzky-Golay filter by fitting a third order polynomial for every 300-400 data points.

2.4.4 Crack Growth Tracking

Accurate measurement of crack lengths in microscale fracture tests is challenging. The compliance calibration procedure correlates crack initiation with a drop in stiffness, where the point of crack initiation is the point of the maximum stiffness of the CSM curve [59], but the video data may not show an initiated crack at that displacement/time. This is because crack growth is non-uniform across the specimen thickness and a crack initiated at the center of the beam width may not be visible at the face of the sample right when the CSM value drops. For all other time instances thereafter, the crack lengths generated from compliance calibration represent an average crack length for a given specimen. Although this works reasonably well for the stiff HD and MD samples, for the LD samples, there wasn't a notable peak in the CSM stiffness, which created ambiguity around the crack initiation point detected by the compliance calibration procedure. To understand the discrepancy in our compliance calibration vs video data as well as to obtain an alternate set of crack length values for the LD beams, we utilized the in-situ video data. A Python script was developed which first smoothed the image frame within the given threshold values and then utilized edge detection functions to detect the crack tip, corners and the bottom edge of the beam. Polynomial fit functions were utilized to approximate the base of the beam and then the distance between the base and the tip of the crack was measured and plotted with the crack lengths obtained from the CSM data. In general, we found good agreement between the compliance calibration and video data, and therefore used the crack lengths generated by the compliance calibration procedure to calculate subsequent J-integral crack growth resistance curves.

2.4.5 Plastic Zone Size

A simple approximation of the plastic zone size for acrylate-based materials can be obtained by using the relationship $r_p = 1/(K_{ic}/\sigma_y)^2$ where K_{ic} is the fracture toughness and is equal to 1.5 MPam$^{1/2}$ [74], σ_y is the yield strength and is equal to 45 MPa [15], giving $r_p \sim 354$ µm, significantly larger than both the size of the sample and the fiber. This means that all samples undergo large-scale yielding with damage zones much larger than the sample size. With increasing twist angle, increased inhomogeneity of the architecture delays damage further, indicating a larger damage/fracture process zone. This also means that the J_{1L} values are significantly lower than the actual fracture energy of the sample.

2.4.6 J-R curve Measurement

An elastic-plastic Mode-I J-integral was used to determine the fracture behavior and crack growth resistance (J–R curve) of the samples as defined in ASTM E1820-20b. Presently, there is a lack of standard procedures to define the critical fracture toughness (J_q or J_{ic}) from crack resistance curves in microscale fracture tests [110]. Efforts have been made to adopt macroscale standards for microscale tests [65, 123, 8], however, these strongly depend on the size of the sample, type of material being tested, and the material's plastic behavior at relevant length scales. Thus, to meaningfully quantify fracture energy, we compare the J value at a crack growth equivalent to one layer crack extension, which is at $\Delta a \approx$1.5 µm and is denoted here as J_{1L}. This definition of J_{1L} allows for a direct comparison of the fracture energy of the nano-Bouligand materials at a consistent amount of crack growth. Note that this is not meant to serve as a standard method for calculating material fracture energy, it is simply a useful metric for analyzing the materials in this work, and a more fundamental investigation is needed to ascertain how fracture energies at the microscale can be extrapolated to macroscopic material properties. Specific fracture energy, i.e., fracture

energy normalized by relative density ($\overline{J}_{1L} = J_{1L} \ / \ \overline{\rho}$), is also calculated to compare the energy dissipated by the nano-Bouligand beams per unit solid volume. Figure 2 shows the crack propagation process in the nano-Bouligand beams along with a representative J–R curve obtained from testing. Non-linear fracture mechanics based Mode-I J-integrals were computed using the following equations:

$$J = J_{elastic} + J_{plastic}. \tag{2.1}$$

Here J is the total J-integral value and $J_{elastic}$ and $J_{plastic}$ are its elastic and plastic components. The instantaneous elastic component can be expressed as:

$$J_{el(i)} = \frac{K_i^2(1-\nu^2)}{E} \text{ and } K_i = \left[\frac{P_i S}{(BB_N)^{1/2} W^{3/2}}\right] f(\frac{a_i}{W}). \tag{2.2}$$

Here K_i is the stress intensity factor for a given crack length a_i, E is the Young's modulus, and ν is the Poisson's ratio. P_i is the instantaneous load, S is the span length, B is the beam thickness, W is the beam width, B_N is equal to B, and $f(\frac{a_i}{W})$ is the geometry factor specified for the SENB geometry in [59]. The instantaneous plastic component can be further expressed as:

$$J_{pl(i)} = [J_{pl(i-1)} + (\frac{h_{pl(i-1)}}{b_{(i-1)}})(\frac{A_{pl(i)} - A_{pl(i-1)}}{B_N})]* \quad [1 - \gamma_{pl(i-1)}(\frac{a_i - a_{(i-1)}}{b_{(i-1)}})], \tag{2.3}$$

where b is the length of the uncracked ligament and A_{pl} is the area under the load-displacement curve. The quantity $A_{pl(i)} - A_{pl(i-1)}$ is the increment of plastic area under the load-displacement curve between lines of constant plastic displacement at points *i-1* and *i*.

$\eta_{pl(i-1)} = 1.9$, and $\gamma_{pl(i-1)} = 0.9$ as defined for SENB geometry [59].

2.5 Results

2.5.1 Load-Displacement Behavior

Load-displacement data and post-fracture images of all nano-Bouligand beams are shown in Figure 2.6, but for sake of brevity only unidirectional and $\theta = 5^\circ$ and 30° nano-Bouligand beams will be discussed. As is expected, the bending stiffness and peak load scale proportionally with sample density and inversely with interlayer twist angle.

The proportional scaling with density is clearest in unidirectional samples, where the HD-, MD- and LD-0° beams have bending stiffnesses of 0.73 N/m, 0.58 N/m, and 0.44 N/m, respectively, obtained from the slope of the straight line fits in the linear elastic part of the load-displacement response as seen in Figure 2.6. A similar trend is observed in the 0° sample peak load, which are 2.1 mN, 1.4 mN, and 0.9 mN, respectively. An increased twist angle results in nanofibers that are rotated away from the bending axis, thereby reducing the effective bending strength and stiffness of the samples. This is most pronounced in the MD and LD samples due to their lower transverse layer strength and stiffness. Irrespective of density or twist angle, all samples show a gradual softening after the onset of failure, indicating a stable crack growth.

2.5.2 Crack Initiation, Propagation and J-R Curves

J-Integral calculations reveal a varying fracture behavior that is dependent on both density and interlayer twist angle. Notably, all samples had a clear rising J–R curve, so the J_{1L} values provided an important distinction in fracture behavior. The effect of density is again most apparent in the unidirectional samples, wherein the fracture energy of all densities of beams was nearly identical with $J_{1L} \approx 42$ J/m^2. This means that there was no observed

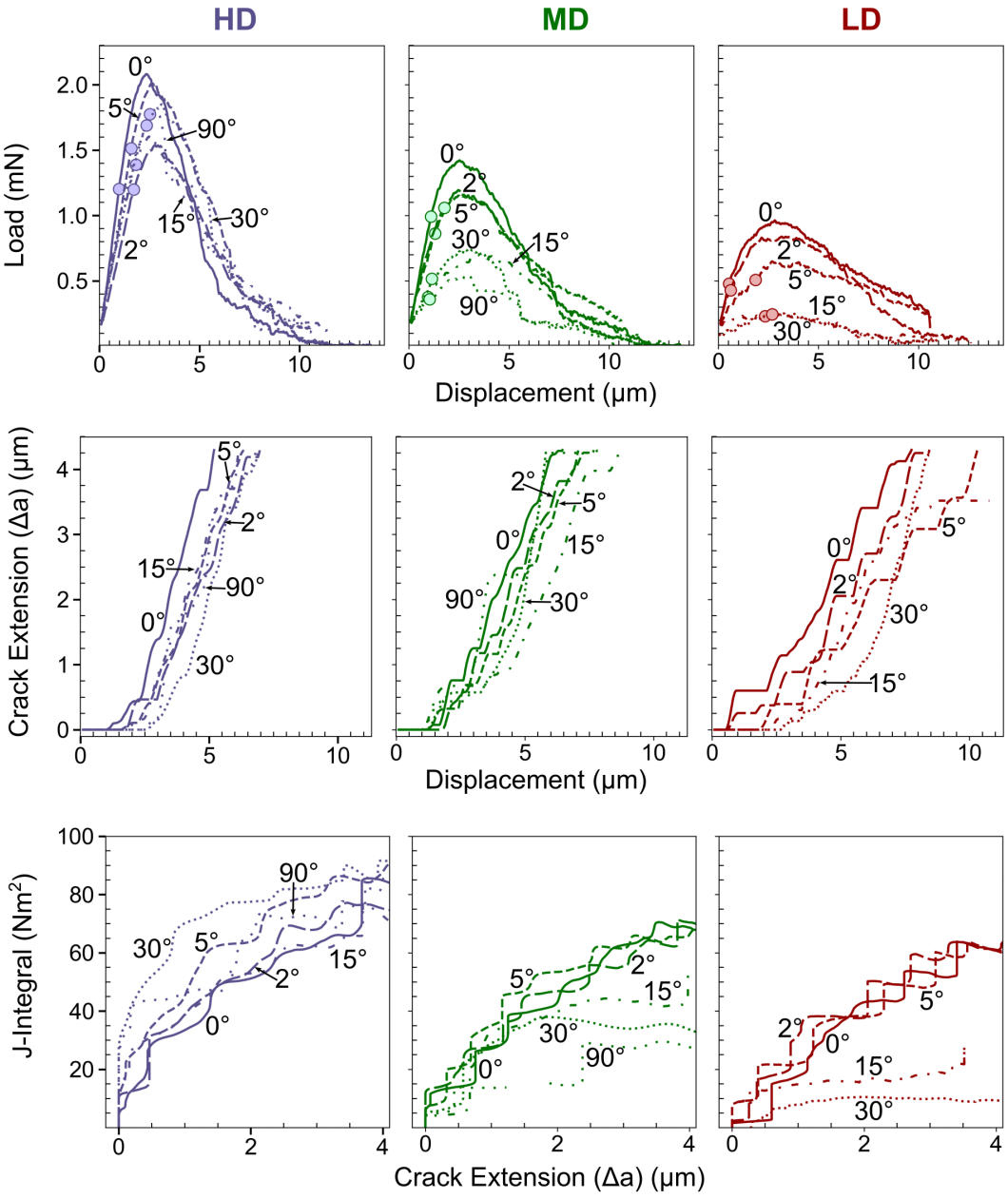

Figure 2.6: **Nanomechanical test data and corresponding crack growth resistance curves.** Load displacement, crack extension, and J-integral plots of the 0°, 5°, 15°, 30° and 90° twist angle beams corresponding to each tested relative density.

fracture energy scaling with density. Cracking in the unidirectional samples initiated at a beam displacement of ~1.2 μm, and cracks extended rapidly through the beam cross-section. The final crack fronts appear smooth and straight (Figure 2.7 and movie S1, S4, S5), and cracks penetrated through the entirety of the unidirectional beams.

The toughness of the twisted nano-Bouligand beams was highly dependent on relative density. The HD samples showed an increase in J_{1L} with increasing twist angle and had steeper J–R curves. The HD-30° beams correspondingly had the highest fracture energy ($J_{1L} \approx 67$ J/m^2) of all the specimens tested in this study. The fracture energy of the LD samples showed the opposite trend and had an inverse correlation with twist angle. The LD-30° beam only reached a value of $J_{1L} \approx 25$ J/m^2, the lowest among all specimens tested in this study. There was no clear trend in J_{1L} in the MD samples with twist angle. The J–R curve of all 30° twist angle beams plateaued after a crack growth of ~2 layers, indicating no new mechanisms were activated after a small amount of crack propagation.

Interestingly, the displacement of the beams prior to the onset of fracture did not follow the above trends and instead was strongly dependent on twist angle. This was most dominant for beams with $\theta = 30°$, which had up to a ~2x greater displacement prior to crack initiation than the unidirectional beams (Figure S5 and movie S3, S6). The final crack fronts of samples with higher twist angles were rougher and had wavy edges (Figure 3), qualitatively indicating an increased energy dissipation. This disconnect between the observed crack roughness and the J_{1L} value, along with the varying trends between twist angle and density, indicate that the fracture energy is significantly altered by the sample porosity. It should be noted that crack propagation in all samples was approximately straight and did not deviate significantly as has been observed in other Bouligand materials [127].

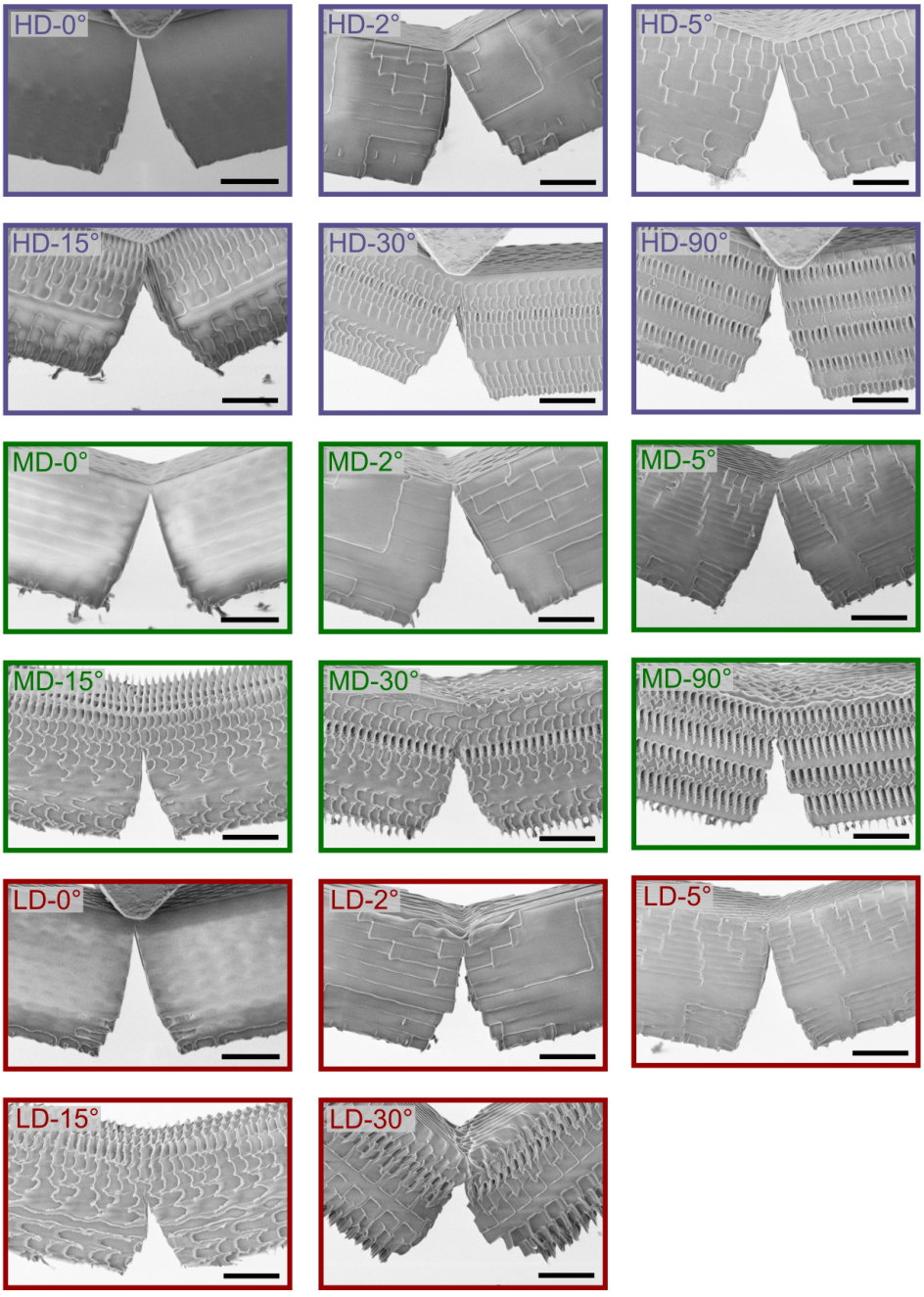

Figure 2.7: **Post Fracture SEM Images of nano-Bouligand beams.** Final images of the fractured beams of every twist angle and relative density tested. All scale bars: 5 μm.

2.5.3 Fracture Surfaces

Post testing, nano-Bouligand beams did not separate into two halves, rather, the crack closed as the tip was withdrawn from the sample. This made imaging the fracture surface of the beams a significant challenge. Images below were taken either when the fracture surface was visible after tilting/rotating the sample in the SEM or beams were knocked down with a thin gauge wire and imaged thereafter (Figure 2.8). We see a relatively smooth fracture surface for beams with low twist angles and a rough, jagged surface with pulled fibers for beams with higher twist angles.

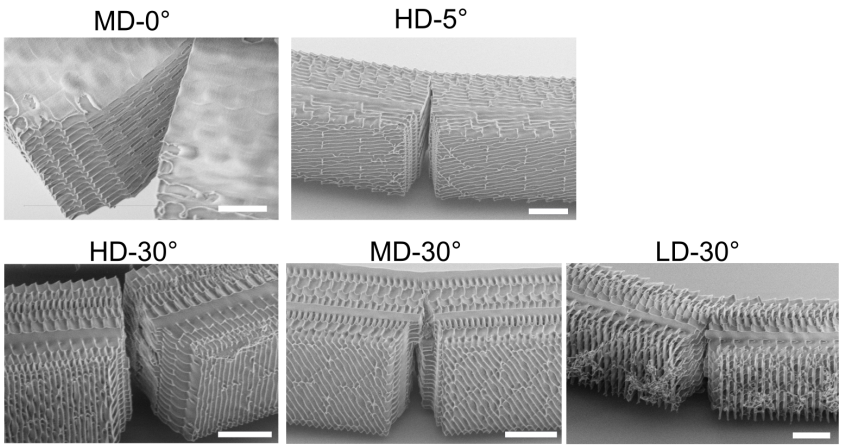

Figure 2.8: **Fracture Surfaces of nano-Bouligand beams.** Transition from smooth surface in low twist angle beams to a rough surface with broken and pulled fibers in the high twist angle beams.

2.5.4 Work of Fracture

Considering the high plasticity, small sample size and the lack of estimation of the plastic zone and fracture process zone size of the nano-bouligand materials in this study, it is possible that the J integral calculated using EPFM underestimates the fracture energy of the material,

since the J-contour will be inside the non-linear zone. For completeness, the fracture energy is additionally characterized as work of fracture. It is computed as $W_f = A_{curve}/B(W - a_o)$ [57] and plotted with the corresponding J_{1L} values in Figure 2.9. Here A_{curve} is the area under the load-displacement curve, B is the specimen width, W is specimen thickness and a_o is the initial crack length.

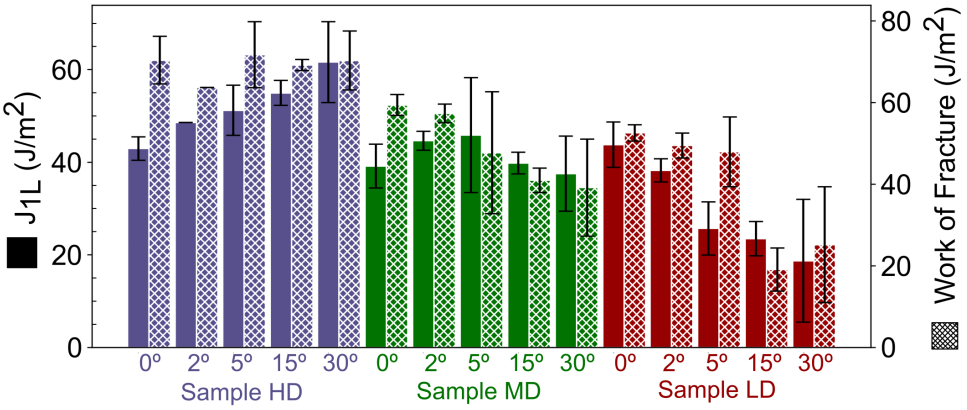

Figure 2.9: **Fracture Energy and Work of Fracture for nano-Bouligand beams.** Comparing fracture energy dissipated after 1 layer (J_{1L}) with total work of fracture. Error bars represent standard deviation values from three runs on each specimen type.

We see that the fracture energies calculated using work of fracture have the same order of magnitude as the J_{1L} values. However, it doesn't show the same trends as the computed J1L values. This might be because the area under the curve comprises the fracture energy of the entire sample whereas J_{1L} is just one layer. It is also interesting that the J_{1L} and W_f values for all the 30° beams are almost equal, which might be because the J for 30° plateaus after an initial rise. In the 0° samples, the J-curves continue to rise, so the W_f is higher than the J_{1L}, and probably the actual fracture energy of the sample might be much higher if we have a greater sample thickness for the J curve to plateau.

2.6 Toughening Mechanisms

In the unidirectional and nano-Bouligand materials studied here, we find two distinct toughening behaviors. First, the $\overline{J}_{1L}$ of the unidirectional beams increases with decreasing relative density. Second, we see that the HD samples progressively toughen with an increasing twist angle. These trends indicate the activation of specific energy dissipation mechanisms that amplify material toughness. Both of these mechanisms are discussed in detail below.

2.6.1 Nanomaterial Effect: Toughening due to Nanoconfinement

Absent any changes in mechanism, fracture energy (G_c or J_c) of low density materials should scale with relative density [7]. In linear elastic fracture, the dissipated energy is proportional to relative density, i.e. $G_c \propto \overline{\rho}$, because it depends on the amount of solid material involved in the fracture process. This scaling relation may not strictly hold for high relative density materials or in elastic-plastic fracture analysis, but it is reasonable to assume an approximately linear relationship between fracture energy and density for most porous materials. Increasing a low density material's fracture energy thereby requires the activation of new energy dissipation mechanisms. While this type of mechanism activation is found in both engineered and natural composite materials, it is unusual to find new mechanisms activated in a single material system. The fracture energy scaling of the 0° unidirectional samples is thus in direct contrast with predictions from traditional fracture mechanics for porous materials [75] (Figure 2.10A). The 0° beams have minimal crack deflection during fracture and the constant z-axis spacing makes property gradients comparable despite the different densities, meaning the only energy dissipation mechanism in the 0° beams is the plasticity of the polymer itself. As the density of the beams decreases, the amount of free surface between fibers increases, creating nanoconfined nanofibers (Figure 2.10C). For the IP-Dip material used here, it has been observed that the tensile toughness (unnotched tensile energy

dissipation) can approximately double between the bulk and nanoconfined polymer due to a large increase in strain to failure [15]. This increased tensile ductility was confirmed in this work using three-point bend tests on unnotched specimens, where failure strain was found to increase ∼2x in the lowest density beams over that of the fully dense beam (Figure 2.4). The increased plastic energy dissipation of the nano-Bouligand beams is, therefore, *due to a size-enhanced change in plastic energy dissipation in the nanoconfined polymer*, which counteracts the predicted scaling of J_{1L} with density and directly improves the specific energy dissipation $\overline{J}_{1L}$ as seen in Figure 2.10A.

2.6.2 Nanoarchitecture Effect: Toughening due to Nano-heterogeneity

The effect of nanofiber twist angle on toughness and thereby toughening mechanisms is highly dependent on the nano-Bouligand beam density. Crack twisting, which is attributed as a dominant toughening mechanism observed in natural materials with Bouligand architectures, occurs due to the high modulus mismatch between constituent materials [133, 137, 90]. Previous work on bioinspired Bouligand materials at the macroscale similarly utilized stiff fibers and soft matrix materials comprising at least two full Bouligand stacks [85] and successfully reproduced crack twisting, demonstrating reduced damage propagation and enhanced damage tolerance [138, 112, 146, 93].

While the nano-Bouligand beams here have an extreme layer stiffness anisotropy – especially in the LD beams – and exhibit demonstrably rougher fracture surfaces with higher twist angles (Figure 2.8), we do not observe crack twisting or deflection in any of the samples tested here. Fabrication limitations on the overall sample size of the nanoarchitected beams prevented the creation of multi-stack Bouligand beams in this study, and it is possible that there are too few layers to develop a twist, but it is unclear from these experiments alone. Despite this absence of crack twisting, the increase in the J_{1L} value of the HD nano-

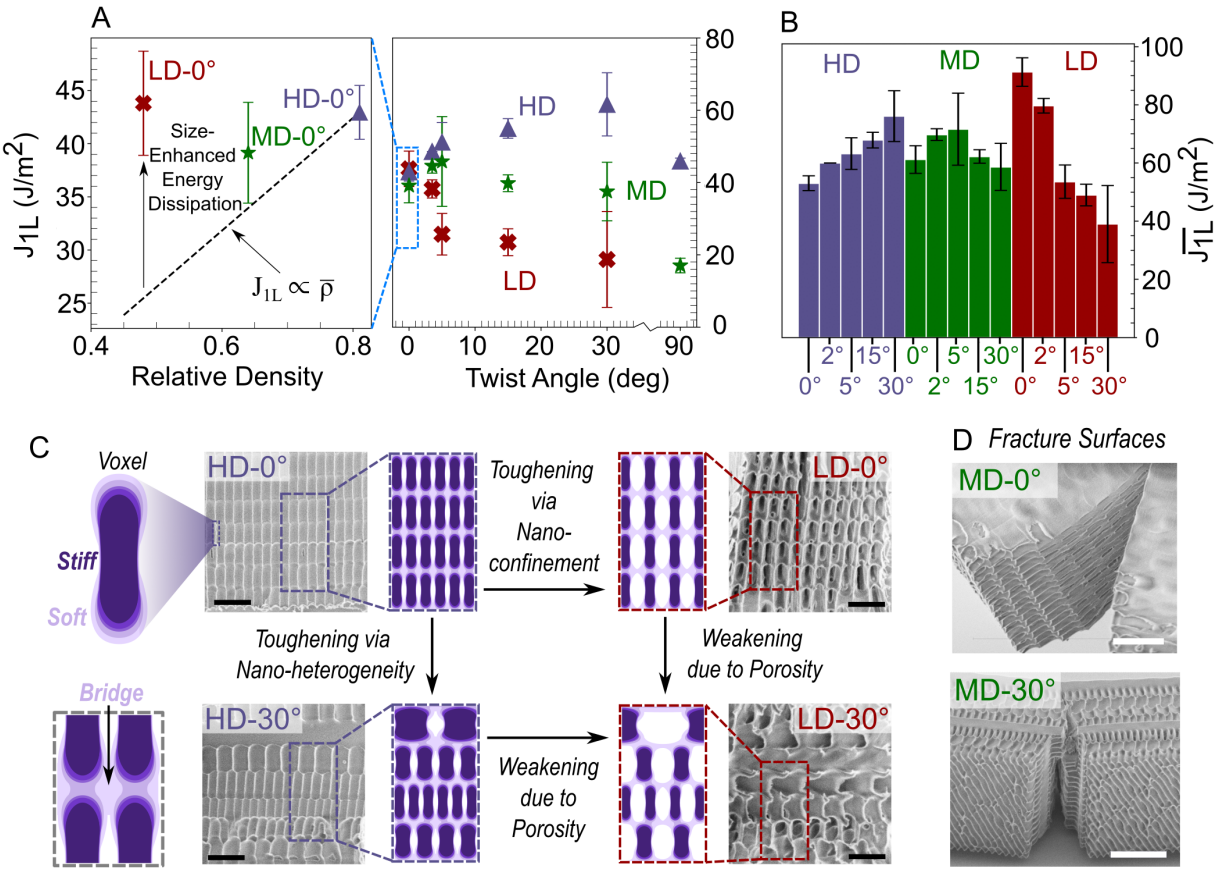

Figure 2.10: **Fracture Energies and Stiffness Gradients of nano-Bouligand beams**. (A) Left-Fracture energy J_{1L} vs relative density for the 0° twist angle beams. Error bars represent standard deviation values from three runs on each specimen type. Right-Fracture energy J_{1L} vs twist angle for all the '$\bar{\rho}$-θ' beams tested in this study. (B) Specific fracture energy ($\bar{J}_{1L}$) of all the '$\bar{\rho}$-θ' beams, showing the amplification in fracture energy of the LD-0° beam. (C) Representative SEM images of the HD- and LD-0° and 30° beams along with a schematic illustrating the stiffness variation through the beam cross section. The dark region represents the stiff core of the nanofiber, and lighter regions show the gradually decreasing stiffness towards the outer edge of the fiber. The lightest regions represent the weakly cross-linked bridging between fibers that arises due to proximity effects, and the white regions depict voids. All scale bars are 3 μm. (D) Fracture surfaces of the MD-0° and 30° beams showing increasing roughness with increasing twist angle.

Bouligand beams (Figure 2.10A) clearly indicates the activation of a toughening mechanism with changing twist angle, a trend that is reversed in the LD beams.

Toughening can therefore be understood in the context of heterogeneous stiffness distributions. Kolendik et. al. propose that the crack tip driving force (J_{tip}) directly depends on stiffness inhomogeneity as
$J_{tip} = J_{far} + C_{inh}$, where J_{far} represents the driving force due to the applied load and C_{inh} represents the driving force induced by the inhomogeneity [68]. The C_{inh} term can drive or resist crack propagation depending on location; crack growth will accelerate in a stiff/soft transition ($C_{inh} > 0$), and cracks will slow down at a soft/stiff transition ($C_{inh} < 0$). This periodic variation in stiffness can enhance fracture resistance over homogeneous materials depending on the number of stiff/soft interfaces present and the average value of C_{inh}, meaning toughening can occur in twisted fiber structures even in the absence of crack twisting [42].

In the nano-Bouligand materials here, the center of the nanofiber – i.e. the middle of the line write path – is the stiffest part of the material ($E = E_{max}$), the midpoint between nanofibers is the most compliant ($E = E_{min}$), and the void regions around the fibers have zero stiffness ($E = 0$) (Figure 2.10C). These spatial gradients in stiffness create a complex network of crack shielding and anti-shielding regions that become more inhomogeneous with increasing twist angles. In the HD nano-Bouligand beams, this inhomogeneity has an aggregate crack shielding effect ($C_{inh} < 0$) and leads to a delayed crack initiation, thereby causing both a higher initiation toughness and a higher J_{1L} with increasing twist angles (Figure 2.6). In the MD and LD beams, there is an even greater gradient between the layers, which should also create a crack shielding effect, but the high porosity significantly reduces the material activated during fracture and enables the crack to easily propagate along the zero-resistance void regions ($C_{inh} > 0$), resulting in a lower J_{1L}. It should be noted that all the materials in

this study have a 3D spatial variation in stiffness (Figure A.1), meaning this J_{tip} analysis is overly simplified but provides a useful qualitative description of the observed phenomenon.

The significant variation in fracture behavior between the nano-Bouligand beams of different relative densities and twist angles show that a knowledge of local variation in material properties is critical to fully understand the operative toughening mechanisms. In the nano-Bouligand materials studied here, these spatial variations occur over length scales $\sim$ 50 nm - 100 nm, which is comparable to the nanostrucutral length scales observed in natural materials [58]. The stiffness gradients that arise from the TPL process blur the line between a single material and a multi-material system, requiring a close investigation of the boundary between material and architecture. Further improvement in our understanding of the underlying toughening mechanisms will require the development of better theoretical models of TPL voxel interactions at the molecular scale as well as nanoscale resolution characterization methods like tip-enhanced raman spectroscopy [66] to understand the 3D spatial variation of material properties.

We demonstrate the creation of fracture resistant nanoarchitected materials that acquire their enhanced properties through nanoscale toughening mechanisms. By isolating and changing the orientation of materials comprised of twisted polymeric nanofibers, we show that toughness is significantly improved by the activation of size-enhanced plastic energy dissipation and nanoscale heterogeneity. We further show that nanostructure in materials can be generated explicitly using fiber architecture or indirectly via spatial property gradients, and both of these can drastically alter toughening behaviors.

This work has direct implications for the printing of any additively manufactured material, particularly materials that are lightweight and made using a TPL process. There are inherent gradients in all materials, but additive manufacturing enables the intentional introduction of gradients based on print paths and layer thicknesses. It is now apparent that

any internal stiffness gradient in a material can be beneficial for crack growth resistance and should be carefully considered in part design. While it is challenging to create high-density nanofibrous materials using the TPL process here due to proximity effects, other fabrication methods that allow for the creation of dense, separated nanofibers could also have marked improvements in toughness. More broadly, toughness at the nano/microscale is not an "intrinsic" material property, but it can be affected by molecular or nanoscale heterogeneity in a unique and controllable way. There is, therefore an enormous potential for fundamentally re-investigating the origins of fracture toughness and our ability to engineer crack resistance at any scale.

2.7 Preliminary Explorations of the Herringbone Architecture

The study of nano-Bouligand architectures illustrated the impact of material property gradients on fracture and energy dissipation. Extending that idea, in this study we tried creating materials with 3D spatial distribution of properties by means of a herringbone bouligand architecture, and understand the emergent fracture behaviour of these materials. By utilizing wavy, out-of-plane fibers, we can create dense beams with highly tortuous crack paths, fundamentally engineering toughness via nanoscale gradients and architecture.

2.7.1 Design and Fabrication

We designed microscale beams with herringbone bouligand-type architecture that have a controllable relative density ($\overline{\rho}$) and twist angle between layers (θ). The Herringbone architecture consists of wavy-double sinusoidal fibers, where the waviness is defined by *f(x,y)*, where

$$f(x,y) = A\left(\frac{sin\ 2px}{l}\right)\left(\frac{sin\ 2py}{l}\right) \tag{2.4}$$

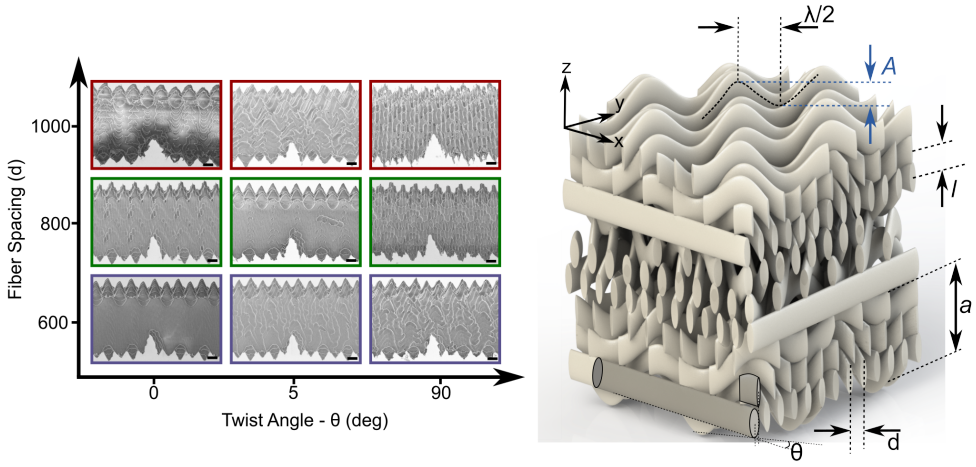

Figure 2.11: **Design Space of herringbone nano-Bouligand Beams.** (Left) Design space showing SEM images of beams of varying d and ϑ (Scale bar: 5 μm). (Right) Computer-aided design (CAD) of the herringbone nano-Bouligand beam showing the hatching (d), layering (l), twist angle (θ), herringbone wavelength (λ) and amplitude *(A)* design parameters.

λ is the wavelength and A is the amplitude of the wave, both equal to 6μm, giving a A/λ ratio equal to 1 as seen in Figure 2.11. Specimens with A/λ ratios between 0.5-1.2 were also fabricated, keeping λ constant. The individual fibers that make up the herringbone nano-Bouligand beams have an elliptical cross-section with major and minor axis equal to ∼1650 nm and ∼480 nm, respectively. The center-to-center distance between layers (l) is set equal to 1500 nm in all beams, creating a minimum of 150 nm of overlap between two layers. The relative density of the beams is controlled by changing the center-to-center distance between the fibers in the plane (d). Hatching distances of d = 600 nm, 800 nm, and 1000 nm were used similar to the nano-Bouligand beams, but relative density is yet to be determined. These will similarly be referred to as High-Density (HD), Medium-Density (MD), and Low-Density (LD), respectively. The twist angle is explicitly defined for each layer, and beams of every relative density are written with θ = 0°, 5°, 15°, 30° and 90° as seen in Figure 2.11.

Taken together, samples will be referred to using a '$\overline{\rho}$-θ' designation.

Specimens are designed with a single edge notch geometry and written in a 3-point bend configuration for testing. All beams consist of 10 twist layers, and beam dimensions are determined based on the required specimen aspect ratio defined in ASTM E1820-20b [59], where $1 \leq W/B \leq 4$ and $S = 4W$, where W is the specimen width and S is the span length. Notches are directly written into the beams during the printing process; this is done to avoid introducing any focused ion beam (FIB) milling damage during specimen preparation [8]. The notches are written in the first three layers of the beams, causing them to have a length of $a \approx 4.5$ μm. Specimens were fabricated using two-photon lithography (TPL) direct laser writing (DLW) (Nanoscribe, GmbH) out of a commercial acrylate-based IP-Dip resist using the same procedure as described previously.

2.7.2 Results

Load-Displacement Behavior

Load-displacement data from μSENB tests on herringbone nano-Bouligand beams with twist angles equal to 0°, 5°, and 30° corresponding to each tested relative density are shown in Figure 2.12. For sample types HD and MD, test data display an initial linear elastic behavior followed by a hardening where the crack has initiated but the load continues to increase, and finally a softening after a distinct peak load when the crack propagates (Figure 2.12). Some waviness can be seen in the softening region of the load-displacement data, which corresponds with the failure of individual layers.

With decreasing density, the load-displacement response does not have a clear peak, and instead, samples show a long-plateau region where the load slowly decreases (Figure 2.12). Surprisingly, beams with $\theta = 5°$ have the highest beam stiffness and peak load for a given relative density.

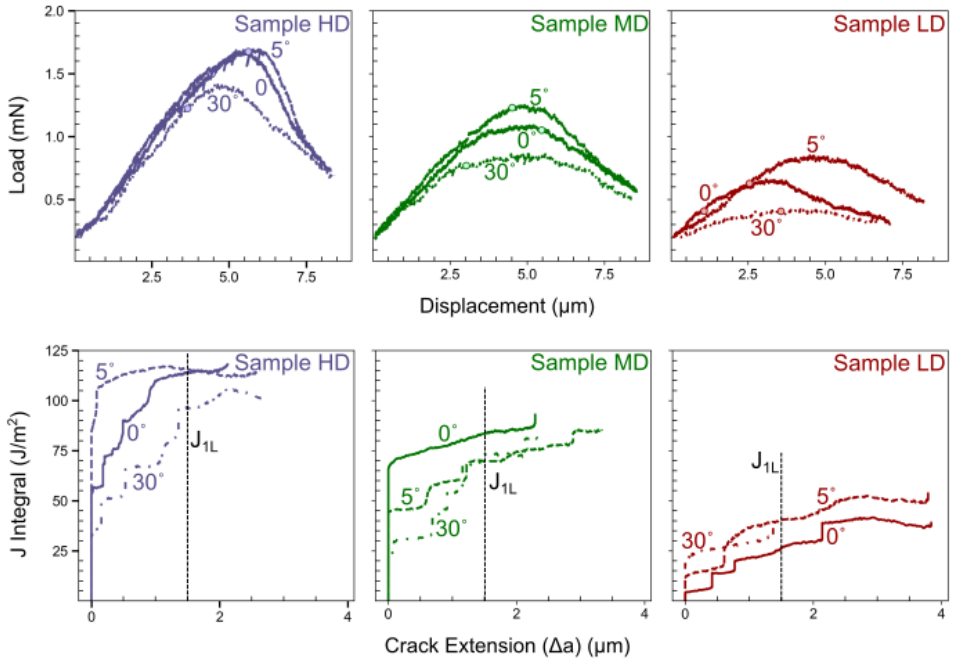

Figure 2.12: **Load-Displacement and J-integral Plots from Nanomechanical Testing.** (Top) Left to right are representative load-displacement response of the herringbone nano-Bouligand beams with 0°, 5°, and 30° twist angles for sample types HD, MD and LD respectively. White circles indicate the point of crack initiation. (Bottom) Left to right shows representative J-integral vs crack extension (J-R curve) plots for sample types HD, MD and LD respectively.

Crack Initiation and Propagation

CSM data and corresponding crack propagation data were obtained using the method described above. In combination with mechanical testing, in-situ video tracking of deforming beams provided salient information about damage propagation and toughening. Significant differences were observed in both crack initiation and propagation between samples of different twist angles and relative densities (Figure 2.13b). Beam displacement at crack initiation, as denoted by the circles in the load-displacement plots in Figure 2.12, was observed to be significantly higher as compared to the nano-bouligand beams in Figure 2.13.

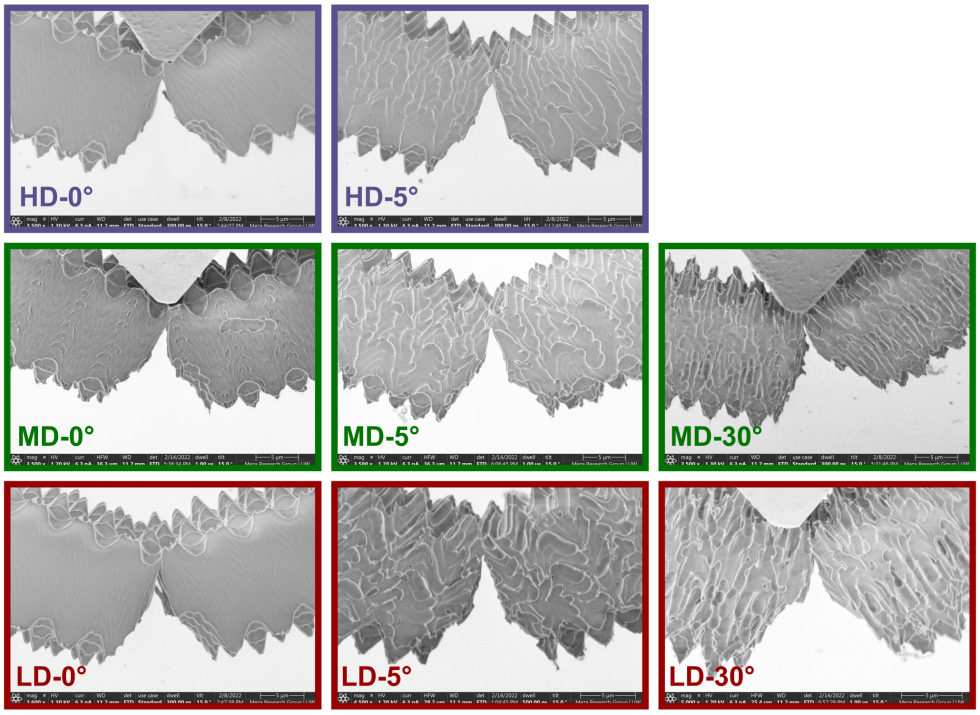

Figure 2.13: **Post Fracture Images of nano-Bouligand beams**. SEM images of the final cracked herringbone nano-Bouligand beams of relative densities types HD, MD and LD and twist angles 0°, 5° and 30°. All scale bars: 5 μm.

Resistance-Curve Behavior

An EPFM based Mode I J-integral was computed for each sample to determine the energy dissipated during fracture as described above. All beams exhibited initially rising J–R curve behavior which eventually approached a plateau state(Figure 2.12), indicating extensive toughening and steady crack extension respectively. Since all the herringbone beams demonstrated significantly delayed crack initiation, we additionally define a , which is the fracture energy at crack initiation and is plotted for all twist angles and relative densities in Figure 2.14. This can additionally be quantified using the J_{1L} value, wherein the HD-5° $J_{1L} \approx 115$ J/m^2, highest among all the specimens tested in this study. In the MD samples,

the J_{1L} values decrease with increasing twist angle, with the rate of increases of the MD-30° sample higher than MD-0° and MD-5° Figures 2.12 and 2.14. In the LD samples, the crack growth resistance is directly correlated with the twist angle. The resistance is maximum for the LD-30° beam, which reaches $J_{1L} \approx 42$ J/m^2, but the LD-0° beam only reaches a value of $J_{1L} \approx 25$ J/m^2, lowest among all the specimens tested in this study. The J–R curve of all the 5° twist angle beams are found to plateau for all relative densities after crack grows through the first layer, indicating that there are no new mechanisms activated after a small amount of propagation.

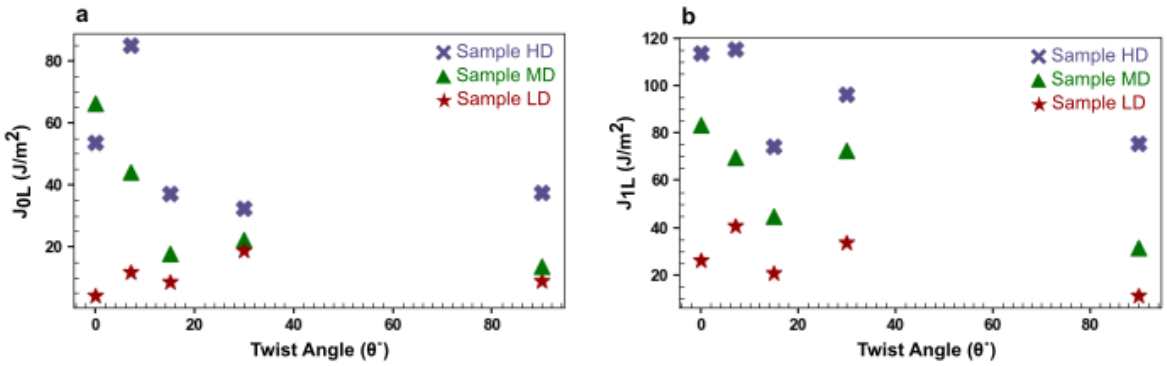

Figure 2.14: **Fracture Energy of Herrinbone bouligand beams.** (Left) Fracture energy at crack initiation (). The HD-5° exhibits the maximum crack initiation resistance with a 85. (Right) Fracture energy after 1 layer crack growth (J_{1L}).

Chapter 3

FRACTURE SIZE EFFECTS IN PURE POLYMER

This chapter has been adapted from:

Patel, Zainab S., et al. "Rethinking ductility—A study into the size-affected fracture of additively manufactured polymers." Additive Manufacturing (2024): 104113.

Contributions: Designed and fabricated samples, conducted experiments, analyzed data, and wrote manuscript.

3.1 Chapter Summary

Ductility, namely a material's capacity for plastic deformation, is a key property for preventing fracture-driven failure in engineering parts. While some brittle materials are known to exhibit ductility at small scales, the underlying mechanics of such behaviors are not well understood. This work identifies size-affected fracture as a key mechanism for the origin of ductility in two-photon lithography (TPL) fabricated polymers. We conducted microscale single-edge notch bend (μSENB) fracture experiments on three distinct specimen sizes and varied the polymer degree of conversion (DC) to be between 17% and 80% by controlling both laser exposure and post-write thermal annealing. For a given specimen size, we find that shifting from low to high DC predictably causes a ∼3x and ∼4x increase in strength and bending stiffness, respectively, but the fracture energy correspondingly drops by ∼6x, from 180 J/m^2 to 30 J/m^2. Notably, this reduced fracture energy was accompanied by a ductile-to-brittle transition (DBT) in the failure behavior. Using a combination of experiments and

finite element analysis, we quantify the fracture yielding zone size (r_p) in these polymers as a function of DC and demonstrate that ductility emerges when r_p approaches the sample width irrespective of the DC. This finding provides a crucial insight that ductility is a size-induced property that occurs when features are reduced below a characteristic fracture length scale and that strength, stiffness, and toughness alone are insufficient predictors of ductility.

3.2 Background

Bend, don't break – materials capable of sustaining deformation without failure are crucial to advanced technologies from semiconductors to aerospace. A material's mechanical resilience depends on its toughness, namely the amount of energy that it dissipates prior to failure. Much of this energy dissipation comes from intrinsic mechanisms like plasticity and internal friction. While materials are often categorized as being ductile or brittle, all materials have energy dissipation mechanisms that occur at some length scale [8, 139, 40]. This may be at the centimeter scale, e.g. for metals, or at the nanoscale, e.g. for ceramics. Understanding the interplay between ductility and the length scale of energy dissipation mechanisms is crucial to creating new materials with enhanced toughness.

Ductility itself quantifies the extent of plastic deformation in a material prior to fracture. Materials with highly active plasticity mechanisms like dislocations in metals or chain sliding in polymers are thought to be more ductile, and processing methods correctly focus on activating these mechanisms to promote ductility [142, 102, 115, 143, 10]. Ongoing efforts in nanomechanical materials testing has demonstrated a unique phenomenon of size-enhanced ductility, and there are numerous experimental and computational studies showing that ductility emerges at small scales in materials that are otherwise considered to be brittle, such as silicon [56, 104, 63], amorphous carbon [2, 148, 126], metallic glass [33] and even quasicrystals [150]. This size-enhanced ductility is generally attributed to modified stress

states at small scales or the activation of new plasticity mechanisms, but the true mechanistic origins of ductility remained unclear.

Ascertaining the origins of ductility first requires an understanding of fracture processes. Prior to fracture, materials will develop a yielding zone of length r_p in front of a crack, which comprises a fracture process zone (FPZ) of length l_{ch} and a plastic zone (PZ) of effective length r_p-l_{ch}. Samples larger than this yielding zone will undergo fracture-governed failure, while samples smaller than this yielding zone will undergo strength-driven failure. In the strength-driven regime, materials with a large PZ and small FPZ will experience ductile fracture, while materials with a small PZ and large FPZ will experience quasi-brittle fracture. Many studies in this field, pioneered by Bažant, have explored the size-affected transition from fracture-driven to strength-driven failure [19, 23, 20, 25], but they often focus on the nominal strength in quasi-brittle materials like concrete and rock and ignore emergent small-scale ductility.

Two-photon lithography direct laser writing (TPL-DLW) provides an ideal platform for studying size-affected fracture due to its exceptional ability to create parts with feature sizes as small as 100 nm [83, 73]. It has been highly successful in creating metamaterials with novel mechanical performance in part because it enables the utilization of size-enhanced nanomaterial properties [88, 18, 17, 141]. Significant work has gone toward understanding the role of process parameters on TPL polymer performance, particularly the relationship between the degree of conversion (DC) – i.e., the extent of cross-linking between polymer chains – and strength and stiffness [15, 16]. While these properties are important, there is currently a lack of information on how TPL process parameters and the resulting characteristic length scales affect fracture performance.

In this study, we use microscale single-edge notch bend (μSENB) experiments to investigate the strength, stiffness, toughness, and ductility of a TPL-DLW polymer as a function

of DC and part size. Experiments reveal that increasing the DC from 17% to 80% increases both strength and bending stiffness by a factor of ∼3x and ∼4x, respectively, but that there is a corresponding ∼6x reduction in the toughness that additionally coincides with a ductile-to-brittle transition (DBT) in the polymer. To understand this DBT, we conduct size-effect experiments and develop an elastic-plastic-damage finite element (FE) model with properties fit to the experimental strength and toughness data. We then demonstrate how changes in both sample size and yielding zone size induce size-affected changes in fracture behavior.

3.3 Methods

3.3.1 Design

Microscale beams with varying degrees of conversion were designed in a single-edge notch bend (μSENB) configuration. Beam dimensions were determined according to ASTM E-1820b [41] with a standard beam thickness of W = 26 μm and span-to-thickness ratio S/W = 2. Notches were directly written into the beams during the printing process to avoid introducing any focused ion beam (FIB) milling damage [8]; these had an initial length a_o = 4.5 μm and an a/W = 0.17. Additional geometrically scaled specimens with thicknesses equal to W, 2W/3, and W/3 were created to characterize the size of the fracture yielding zone and the material fracture energy.

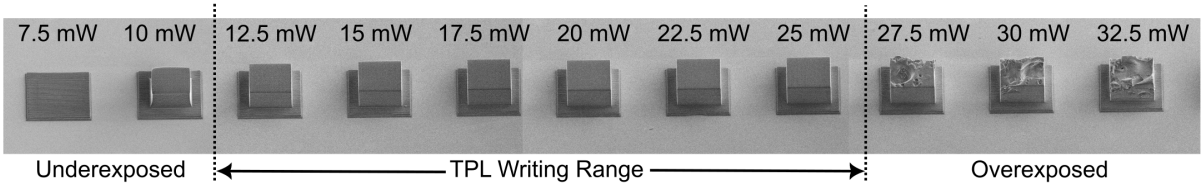

Figure 3.1: **Polymerization range of IP-Dip**. Parameter sweep showing the writing range of TPL resin.

Two separate variables were used to change the polymer degree of conversion: i) laser power (LP) was varied between 11 mW to 25 mW in ∼2.5 mW increments , and ii) annealing temperature (T) was varied between 25°C to 200°C in ∼25°C intervals (Figure 3.2A,B,C and Figure S1). The maximum temperature of 200°C was chosen because it is well below the degradation onset temperature of the photopolymer of ∼250°C [16]. Using temperature as a control variable not only allows samples to have a higher DC than what can be achieved with TPL alone, but it creates an overall more homogeneous material with a uniform degree of conversion through the cross-section. This minimizes any additional toughening due to material heterogeneity effects [108].

3.3.2 Fabrication

Specimens were fabricated on silicon substrates, which were first etched for 5 minutes in oxygen plasma (Plasma Etch PE25) and then functionalized using 3-(Trimethoxysilyl) propyl methacrylate to improve adhesion and prevent peeling off of supports during fracture tests. Printing was done using a two-photon lithography (TPL) direct laser writing (DLW) system (Nanoscribe, GmbH). A proprietary acrylate-based resist, IP-Dip (Nanoscribe, GmbH), was used with a 63x objective to achieve high-precision, sub-micron resolution writes. Writing speeds, specimen hatching, and layering were all kept constant at 10 mm/sec, 100 nm, and 300 nm, respectively, to minimize any heterogeneity from the TPL-DLW process. Support lattices were written in piezo mode with a low laser power (6 mW) to ensure faster etching. After printing, samples were immersed in a propylene glycol monomethyl ether acetate (PGMEA) solution for 20 mins, then in ultrapure IPA for 30 mins, followed by critical point drying (Tousimis Autosamdri-931). These were subsequently etched in an oxygen plasma etcher (YES CV200 RFS) at 65 W power for 25-35 mins until the support lattices were completely removed, producing free-standing fracture specimens, a method first demonstrated

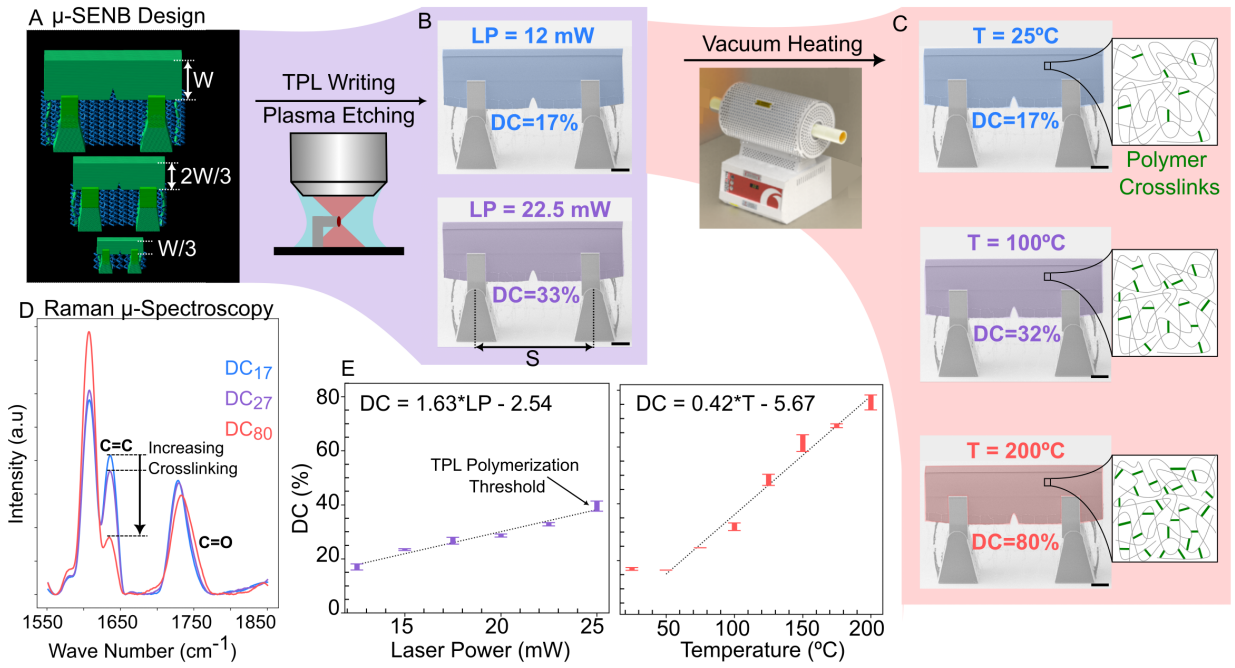

Figure 3.2: **Polymer Degree of Conversion** (DC)**:** A) Graphic rendering of the μSENB design showing the three different beam sizes tested in this study.

B) Specimens with DC values between 17-39% generated using different laser exposures in TPL. C) Specimens with starting DC value = 17% are heated under vacuum to generate specimens with DC values between 17-80%. Insets illustrate increasing cross-linking density. D) Raman spectra for specimens with three different DC values showing the decreasing intensity of the C=C peak, which correlates to increased cross-linking between the polymeric chains. E) Raman data showing the effect of laser power and temperature on DC. All scale bars = 10μm.

by Gross et al [51]. Thermal treatment samples were written with a 15mW laser power, then heated in a high vacuum tube furnace (Carbolite Gero), and maintained at their peak temperature for 1 hour. Large sweeps were written to quantify the polymer degree of conversion as a function of laser power and temperature (Figure S1).

3.3.3 Raman μ-spectroscopy

Raman micro-spectroscopy was performed on printed beam samples to quantify their DC. Raman Spectra were acquired using an inVia (Renishaw plc) confocal Raman microscope with a 50× objective, operated at an excitation wavelength of 785 nm, with a laser intensity of 50% and an exposure time of 10s averaged over 3 acquisitions. DC values were extrapolated from Raman spectra using the relationship $DC = 1 - (\frac{A_{C=C}/A_{C=O}}{A'_{C=C}/A'_{C=O}})$ [11]. Here, $A_{C=C}$ and $A_{C=O}$ are the integrated intensities of the carbon-carbon and carbon-oxygen double bond peaks in the polymerized resin, respectively, and $A'_{C=C}$ and $A'_{C=O}$ are the integrated intensities of the same peaks in the unpolymerized resin.

Raman spectra revealed that DC increases linearly with both laser power and temperature as $DC = 1.629 * LP - 2.54$ and $DC = 0.418 * T - 5.67$, respectively (Figure 3.2D,E and Figure S2). Varying the laser power produced DC values between 17% - 40%, with 40-45% being the upper limit that can be achieved without overexposing the resin. Heating of samples printed with DC=25% had no effect up to 50°C, after which the DC linearly increased to a maximum of 80% at 200°C. The mechanical properties of this resin system can be estimated based on literature data for both as-written samples [15] and for fully cross-linked samples [16], which show Young's modulus and yield strength variation between 1.5-4.3 GPa and 30-80 MPa, respectively, for the range of DC studied here.

3.3.4 Mechanical Testing

Displacement-controlled in-situ μSENB fracture tests with continuous stiffness measurement (CSM) were conducted using a piezo-driven nanoindentation system (ASA, Alemnis AG). Testing was done in a scanning electron microscope (SEM) (Thermo-Fisher Scientific Apreo) with a 2μm radius conductive diamond wedge tip. Quasistatic tests were conducted with a loading rate of 20 nm/sec, and specimens were tested either to complete fracture or to a

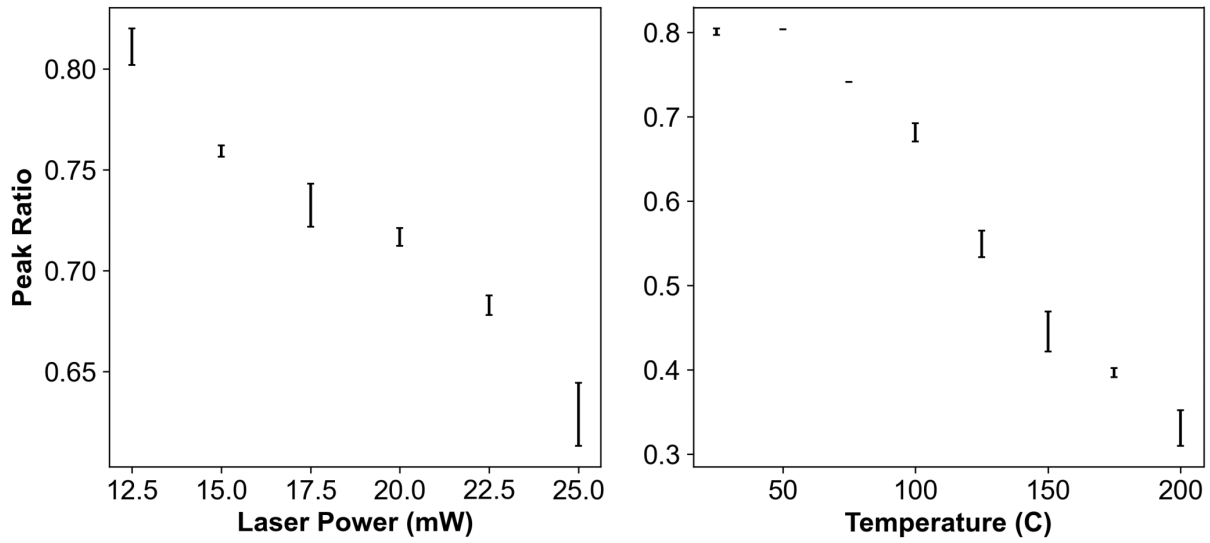

Figure 3.3: **Raman Peak Ratio to calculate** DC. The ratio of the integrated intensities of the C=C peak to the C=O peak for different laser powers (left) and post-write annealing temperatures (right) . This peak ratio is used to calculate the polymer degree of conversion.

displacement of 18 μm. Video data were captured for each test. We note that for the purposes of this study, any strain rate-dependent behavior is ignored. A sinusoidal signal of amplitude 40 nm and frequency 4 Hz was superimposed to perform continuous stiffness measurement (CSM) and thereafter compute instantaneous crack lengths. To account for thermal drift, the nanoindenter assembly was installed in the SEM and allowed to stabilize before testing. We additionally added 'out-of-contact' segments before and after the compression step where the tip is not in contact with the sample to correct for any drift in the system. Thermal drift showed a linear correlation with time for short experiment times (less than 30 minutes) and was subsequently subtracted from the load data during data processing. An amplitude-based Fast Fourier Transform (FFT) noise filtering algorithm was used to remove noise from the load-displacement data. Subsequent CSM Data was smoothed using the Savitzky-Golay filter by fitting a third-order polynomial for every 300-400 data points.

3.3.5 J-R curve Measurement

Instantaneous load line stiffness was calculated using the unloading slope of the CSM data, and crack initiation was determined as the point where the unloading stiffness began to decrease. Crack lengths were obtained using a compliance calibration procedure [55] by correlating the crack initiation point with the instantaneous stiffness thereafter. An elastic-plastic Mode-I J-integral was used to determine the samples' fracture behavior and crack growth resistance as defined in ASTM E1820-20b [41].

Presently, there is a lack of standard procedures to define the critical fracture toughness (J_Q or J_{IC}) from crack resistance curves in microscale fracture tests [110]. Efforts have been made to adopt macroscale standards for microscale tests [65, 8, 124], however, these strongly depend on the size of the sample, the type of material being tested, and the material's plastic behavior at relevant length scales. Thus, to meaningfully quantify fracture energy across all the samples tested, we compare the J value at a crack growth Δ a = 2 μm. This is because the J-curves for DC_{hig} and DC_{med} are seen to plateau by that crack extension, meaning they approach their total fracture energy values. Since the DC_{low} J-curves do not plateau, taking J-values at Δ a = 2 μm for all the samples allows one-to-one comparison at a consistent amount of crack growth. This is not meant to serve as a standard method for calculating material fracture energy; it is simply a useful metric for analyzing the materials in this work. It should be noted that this J_Q value is a severe underestimation of the true fracture energy for these materials. A more fundamental investigation is needed to ascertain how fracture energies at the microscale can be extrapolated to macroscopic material properties.

3.3.6 Numerical Modelling

To account for the significant plasticity and post-failure strain softening exhibited by the TPL polymers, an elastic-plastic-damage model was adopted from Salviato [122] and implemented

as a VUMAT subroutine in ABAQUS/Explicit with C3D8R mesh elements. Beams were modeled to be homogeneous, i.e., without any cross-linking gradients, because the in-plane hatching and out-of-plane layering distances between the voxels were sufficiently smaller than the size of the voxel. Sharp cracks, with a crack tip radius comparable to the size in the fabricated beams ($\sim$ 250 nm), were used, and it was assumed that the cracks would propagate in a self-similar manner. The support structures and the indenter tip were modeled as elastic materials with an elastic modulus and Poisson's ratio of 3.5 GPa, 0.35, and 200 GPa, 0.33, respectively. A frictional penalty contact was defined between the beam and supports, as well as between the beam and the indenter tip. Materials were taken to be elastic-linear hardening with a tension/compression strength asymmetry and damage evolution as a function of equivalent plastic strain using a crack band model [113, 114]. Material properties were first estimated using uniaxial tension and compression data from Bauer et al. [15, 16] and then refined to fit experimental data in this work. The elastic modulus, yield strength, and plastic stress-strain properties were obtained from bend tests on unnotched beams, while the fracture energy was determined from experiments on notched beams (Figure S5).

3.4 Results

3.4.1 Strength and Stiffness

The mechanical response of the different test specimens was found to correlate strongly with the DC regardless of whether samples were tested in an as-written state or were thermally annealed. The peak load and bending stiffness both increased with DC, ranging from 4 mN to 11 mN and 1.2 kN/m to 4.3 kN/m, respectively. There was little variation in strength or stiffness after DC $\approx$ 40%, but specimens with a higher DC showed significantly lower strains to failure. Representative load-displacement data are shown in Figure 3.4, and the complete data set for all samples tested is provided in Figure S3.

We observed three characteristic deformation regimes depending on the DC value, which we will distinguish here as DC_{low} for values between 17-25%, DC_{med} for values between 25-40%, and DC_{high} for values greater than 40%. Beams with DC_{low} showed elastic-plastic behavior with long plastic plateaus and slow, stable crack propagation. In DC_{med} specimens, the mechanical behavior was linear up to peak load, followed by gradual softening and stable crack propagation. In contrast, all DC_{high} specimens showed a linear-elastic behavior up to the peak load, followed by unstable crack propagation and catastrophic failure. Stills from in-situ videos are shown in Figure 3.4, demonstrating the significant change in failure behavior with increasing DC (see Supplementary Movies S1-S3).

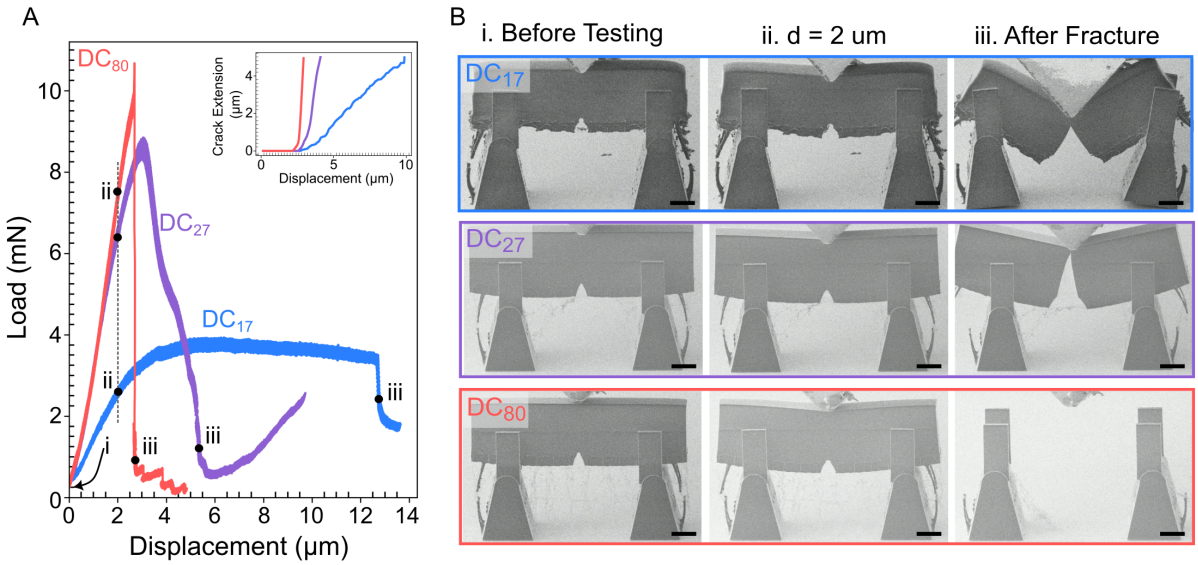

Figure 3.4: **Mechanical Testing Results:** A) Representative load-displacement curves for samples with DC_{low}, DC_{med}, and DC_{high} with inset showing corresponding crack extension vs. displacement. Hollow circles represent the point of crack initiation. B) SEM stills from in-situ videos showing the different failure behaviors observed. Scale bar = 10μm.

3.4.2 Fracture Energy

The load-displacement and CSM data were further analyzed to quantify the fracture properties. Three distinct J-R crack resistance behaviors were observed across the range of DC values studied, as shown in Figure 3.4. In the DC_{low} samples, the moderate softening after the peak load resulted in stable crack propagation and rising J-R curves, with fracture energies as high as $J_Q = 180 J/m^2$, where J_Q is the J value at 2μm of crack extension. In samples with DC_{med}, the greater post-yield softening caused a faster crack propagation, resulting in lower fracture energies of J_Q = 40-60J/m^2. The lower J-R curve slope and near plateau in the J value of the DC_{med} samples indicate that they have a nearly fully developed yielding zone. For samples with DC_{high}, crack growth was unstable, and they had correspondingly lower fracture energies of $J_Q = 30 J/m^2$.

This pronounced ∼6x reduction in J_Q between DC = 17% and DC = 80% specimens is shown in Figure 3.6. Although thermal treatment has been proposed as a homogenization method to eliminate part-to-part property variation and maximize performance [16], these results illustrate that the enhanced strength and stiffness from thermal treatment comes at a significant cost of toughness. The IP-Dip material has a trade-off between strength and toughness, namely toughness decreases as strength increases [119]. An optimal balance between strength and toughness can be obtained for samples with a DC in the range of 20-25%, an important consideration for fabricating parts for structural purposes. Note that the J_Q values here should not be considered true material properties for any test where the J-R curve did not plateau, but they do represent meaningful trends in material properties. The large drop in fracture energy with increasing DC in this work matches well with existing models for polymer fracture energy, which is known to depend strongly on the proportions of cross-linked and entangled chains[70]. Materials with high chain cross-linking density tend

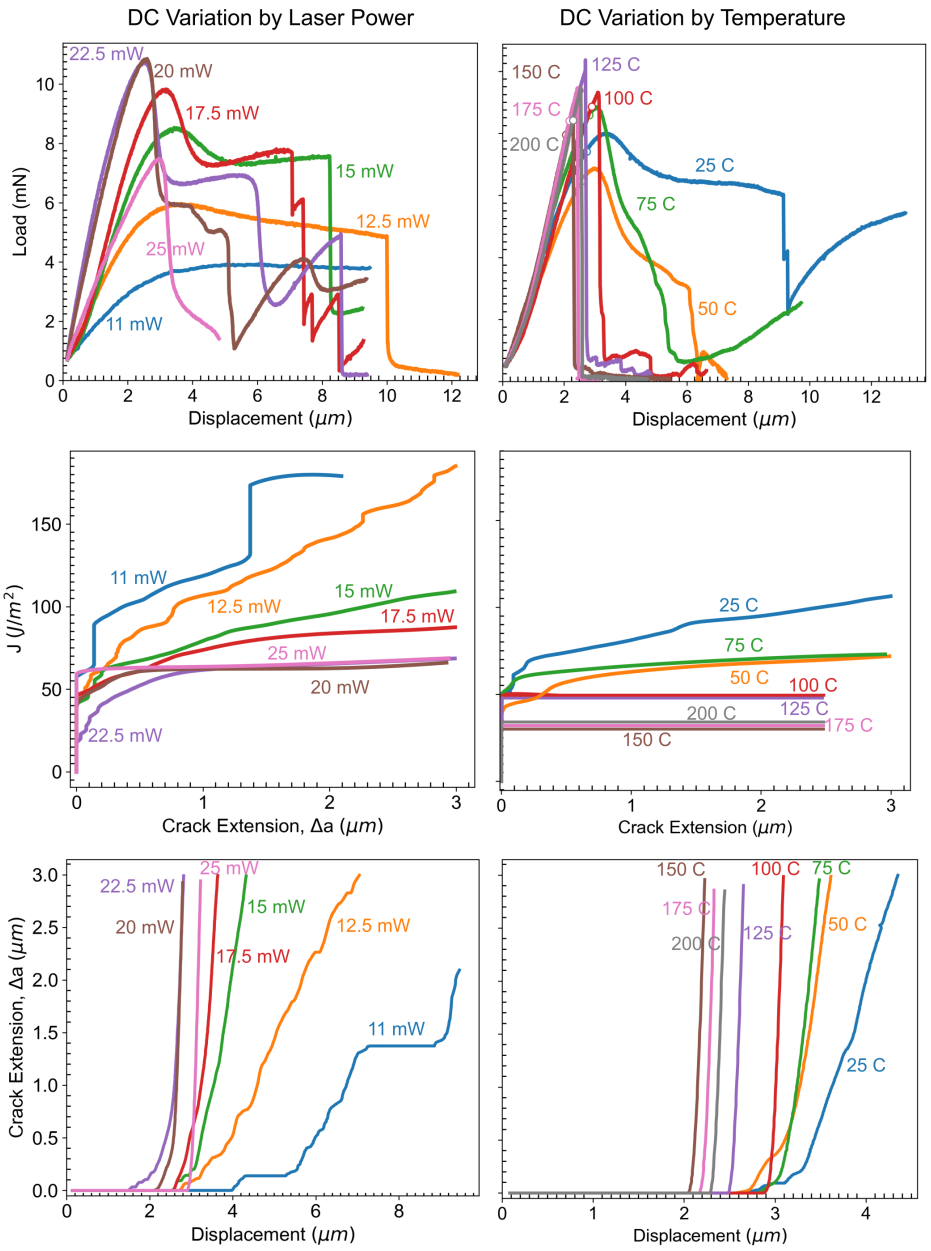

Figure 3.5: **Nanomechanical Response**. load-displacement, J-integral crack extension (Δa) J-R curve, and Δa-displacement curves with varying laser exposures (left) and post-write annealing temperatures (right).

to experience brittle failure via chain scission, while those with high chain entanglement density undergo ductile failure via chain sliding [149, 132, 39]. Various models have been developed to assess the impact of network architecture and defects on fracture energy (G_t) [70, 5, 81], which find that fracture energy scales inversely with chain cross-linking density (v_x) as $G_t \propto v_x^{-1/2}$ in highly elastic materials and $G_t \propto v_x^{-4}$ in elastic-plastic materials [39]. In both cases, lower cross-linking density leads to greater energy dissipation and a corresponding enhanced toughness. However, despite attempts to connect this fracture energy to characteristic length scales [39, 31], there is no mechanistic explanation for the observed ductile to brittle transitions in this or other work.

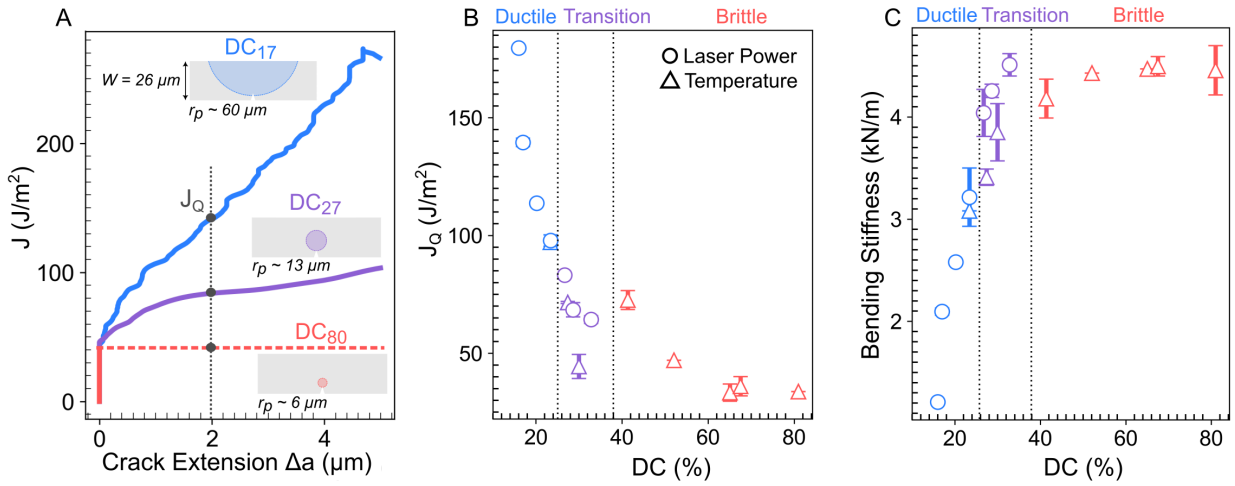

Figure 3.6: **J-R curves, Fracture Energy and Bending Stiffness:** A) Representative J-R curves showing decreasing crack growth resistance with increasing DC. Insets show plastic zone sizes of respective materials. B) Fracture Energy and vs. DC for all samples tested in this study, showing decreasing fracture energy with increasing DC. C) Bending stiffness vs DC for all samples tested in this study, showing increasing sample stiffness with DC. Error bars represent standard deviation values from at least three runs on each specimen type.

3.5 Brief Review of Ductile to Brittle Fracture Transitions

Ductile-to-brittle transitions are well known to occur in various crystalline and amorphous polymers [31, 115, 4]. These transitions have been connected to external factors such as temperature and loading rate and internal factors like molecular weight, density, and microstructure [31]. One essential aspect of these transitions is the ratio of sample size (D) to characteristic fracture length scales. Prior to fracture, a yielding zone of size r_p will develop in front of a flaw. This encompasses a fracture process zone (FPZ) of size l_{ch}, i.e., a damage-driven softening zone at the crack tip, and a plastic zone (PZ) of size (r_p–l_{ch}), i.e., a plastic hardening zone around the FPZ. Standards for measuring fracture toughness generally require specimens to be significantly larger than these fracture length scales (i.e., $D \gg r_p$) to ensure a small-scale yielding condition [41]. In these scenarios, samples will form a small plastic region at the tip of a crack while the rest of the sample remains linear elastic, and brittle failure – i.e., unstable crack growth – will occur when a crack or flaw reaches a critical size.

Small samples with $D \leq r_p$ generally have an enhanced ductility due to energetic size-effects, namely when there is insufficient fracture energy to cause unstable crack growth according to linear elastic fracture mechanics (LEFM). When the PZ is much larger than the FPZ (i.e., $l_{ch} << r_p$), as is the case for many metals, materials will exhibit an increasingly ductile response due to large scale yielding as D is decreased [98]. When the FPZ is much larger than the PZ (i.e., $l_{ch} \approx r_p$), materials will show a quasi-brittle response wherein a large damage zone will develop that suppresses crack propagation, as is the case for most ceramics [23], concrete [19] and polymer nanocomposites [84]. An understanding of ductile-to-brittle transitions is currently lacking for polymeric material systems where both PZ and FPZ can be significant and, at times, comparable. Irrespective of the material and size-effect, samples that are sufficiently large ($D \gg r_p$) will undergo fracture-driven failure, while samples with

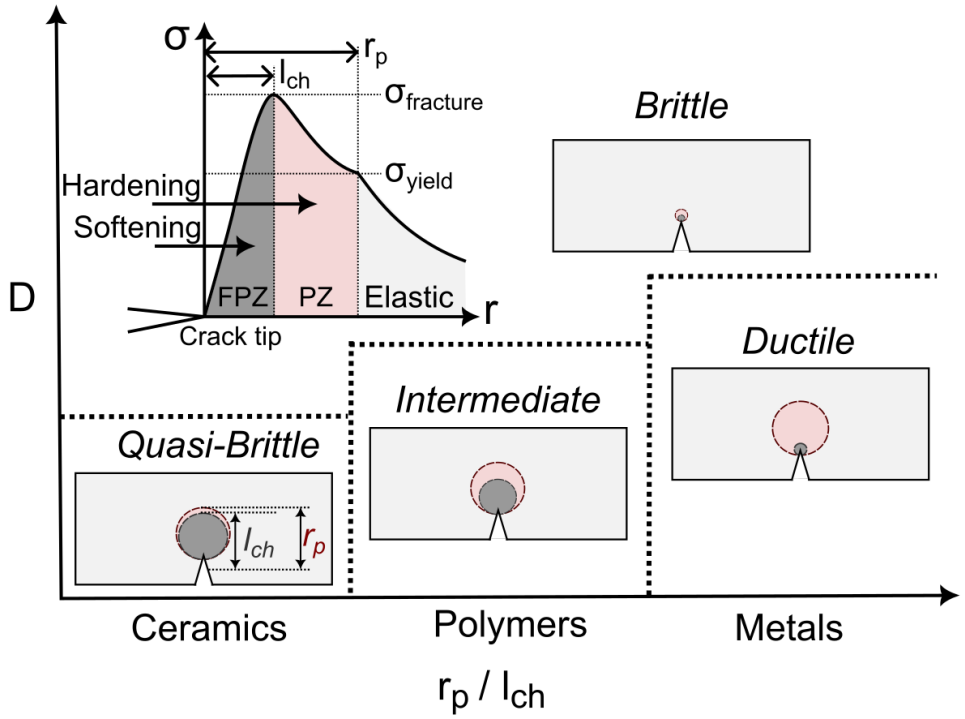

Figure 3.7: **Fracture Transitions** Changing fracture behavior with changing sample size (D) w.r.t to the relative size of the sample yielding zone (r_p) and fracture process zone (l_{ch}).

sizes below the characteristic fracture length ($D \leq r_p$) will experience strength-driven failure [19, 23, 21, 24, 8, 113]. This is illustrated in Figure 3.7.

Bažant-type size effect laws, which quantify changes in nominal strength (σ_N) with sample size are used to analyze energetic fracture size-effects. The size-effect law (SEL) was initially developed for quasi-brittle materials where FPZ $\gg$ PZ [19]. More recently, Nguyen et al. [98] have developed a model for materials whose PZ $\gg$ FPZ, which as a first approximation, is more representative of the materials studied here. This SEL law is expressed as:

$$\sigma_N = \frac{\sigma_o}{\sqrt{1 + D/D_o}}, \tag{3.1}$$

where

$$\sigma_o = \sqrt{E^* G_t / 2r_p}, \text{ and } D_0 = 2r_p / g(\alpha_0). \tag{3.2}$$

Here, σ_o is the maximum material strength, E^* is the effective Young's modulus, G_t is the total fracture energy, $g(\alpha_o)$ is the dimensionless energy release rate, r_p is the size of the yielding zone, and D_o is the characteristic fracture length scale [54, 98]. In the limits of this model, materials with small dimensions ($D \ll D_o$) will experience strength-governed failure with $\sigma_N \propto D$, while materials with large dimensions ($D \gg D_o$) will experience fracture-driven failure with $\sigma_N \propto D^{-1/2}$. Despite the extensive work in this area, there is still a need for better theoretical frameworks when FPZ $\sim$ PZ. More importantly, it is crucial to characterize the relative process zone sizes to understand the underlying causes of ductile to brittle transitions.

3.6 Quantifying Fracture Yielding Zone (r_p)

3.6.1 Simple Estimation

We first assess the size of the yielding zone using a simple LEFM approximation of $r_p = \frac{1}{2\pi}\frac{G_t E^*}{\sigma_y^2}$, where σ_y is the yield strength. It should be noted that this is a generalized expression that does not account for the plastic hardening or the geometry of the structure, both of which can significantly impact the plastic zone [69, 67]. Using the approximate fracture energy dissipation J_Q measured in this study and yield strength values from literature [15, 16], we estimate r_p values of $\sim$60μm, 13μm, and 6μm for DC_{17}, DC_{27} and DC_{80}, respectively, where,

e.g., DC_{17} is a DC of 17%. It is apparent that changes in cross-linking cause a significant change in process zone size, with r_p decreasing by ∼10x as DC changes from 20-80%. The r_p values are illustrated with respect to the beam dimensions in Figure 3.6A.

3.6.2 Size-Effect Law (SEL) Analysis

An SEL analysis was used to obtain a more precise experimental yielding zone size by taking specimens of varying sizes and analyzing changes in their nominal strength with sample size, as described by equations 3.1 and 3.2. Three geometrically scaled DC_{27} and DC_{80} samples with beam thicknesses of 8.5μm, 17μm and 26μm were tested to failure, and their load-displacement data was analyzed using the SEL-based linear regression method to determine G_t and r_p [98]. DC_{17} samples were excluded because the estimated r_p is larger than what could realistically be made using TPL-DLW, meaning the SEL analysis would be invalid. The nominal strength (σ_N), calculated as $\sigma_N = 3P_cS/2tD^2$, where P_c is the peak load, t is the width of the specimens, S is the span between the two supports, and D is the width of the specimens. σ_N can be plotted against the sample size(D), and a linear fit to the data follows:

$$Y = MX + C \tag{3.3}$$

$$\frac{1}{\sigma_{Nc}^2} = \frac{g(\alpha_0)}{E^* G_t} D + \frac{2r_p}{E^* G_t} \tag{3.4}$$

where $X = g(\alpha_0)D$, $Y = 1/\sigma_N^2$, slope $= 1/E^*G_t$ and intercept $= 2r_p/E^*G_t$. Here, E^* is the effective Young's modulus in plane strain configuration, $g(\alpha_0)$ is the dimensionless energy release rate calculated using [54]. As shown in Figure 3.8A,C, good linear fits were obtained

from both the data sets, and the slope and intercept of the fit were used to calculate the total fracture energy (G_t) and effective length of the plastic zone (r_p). These values were then used to obtain the theoretical strength (σ_o) and characteristic length scale (D_o) to obtain the generalized SEL curve as expressed in 3.1.

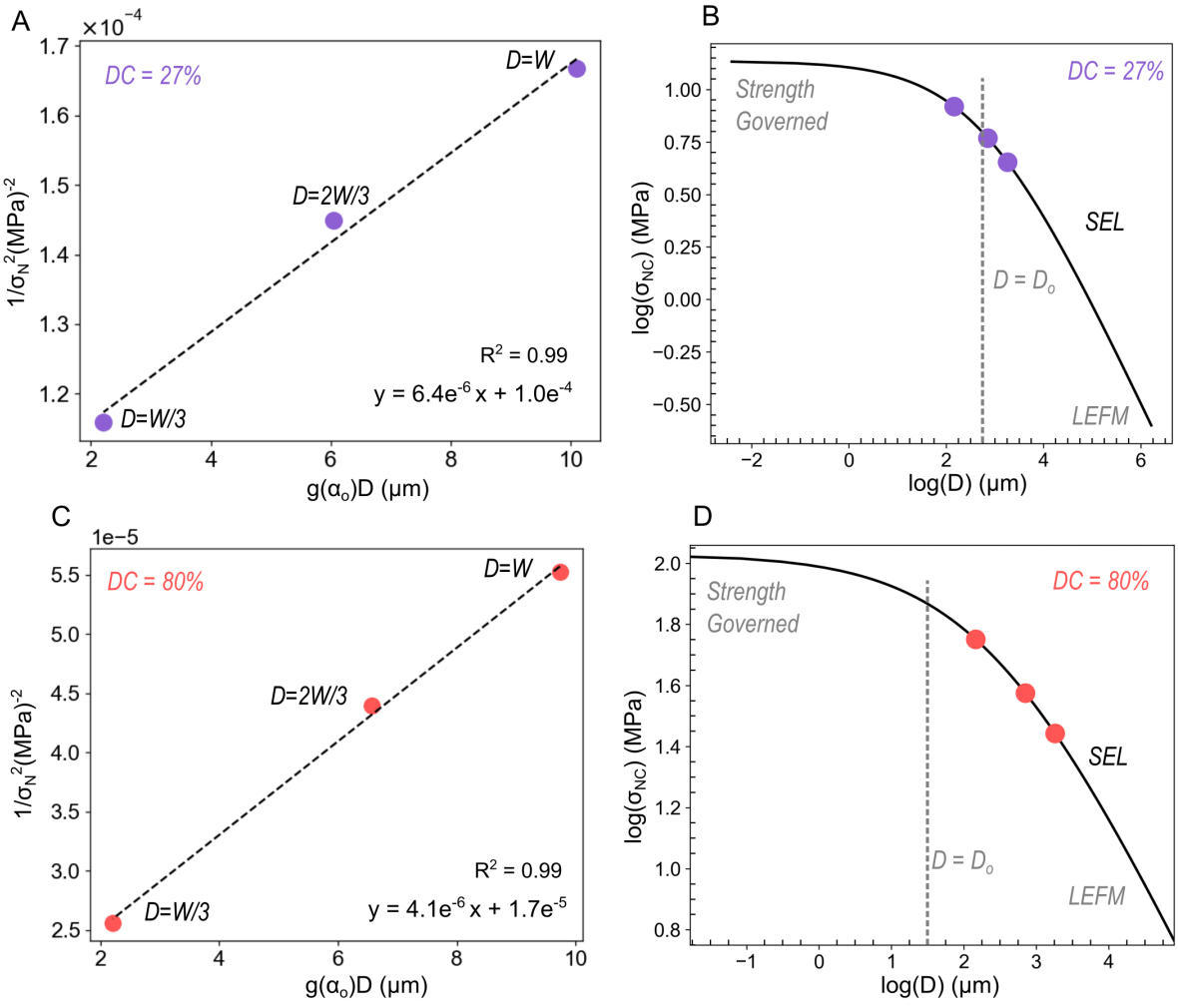

Figure 3.8: **Scaling of strength with structure size:** A,C) Linear regression of experimental data using Equation 3.4 for DC_{27} and DC_{80}, respectively. B,D) Size effect curves showing the transition from LEFM to strength-governed fracture with decreasing specimen size for DC_{27} and DC_{80}, respectively.

Equation 3.1 shows how nominal structure strength (σ_N) varies as a function of sample size (Figure 3.8B,D). These values are also shown in Table 3.1 below. For DC_{80} specimens, even the W/3 specimens fall behind the LEFM to strength transition, but the DC_{27} samples approach the transition point as the $D_o \sim W$. G_t values of $\sim 68 J/m^2$ and $\sim 55 J/m^2$ and r_p values of 8μm and 2μm were obtained for DC_{27} and DC_{80}, respectively. These results demonstrate that the r_p size is reduced by a factor of ∼4x as DC increases from 27% to 80%, and importantly that the r_p for the DC_{27} specimens begins to approach the 26μm sample thickness.

Table 3.1: Theoretical strength (σ_o), characteristic length (D_o), yielding zone radius (r_p), and total fracture energy (G_t) for different degrees of conversion (DC).

DC(%)	σ_o(MPa)	D_o (μm)	r_p (μm)	G_t (J/m^2)
27	98.35	16.06	8.03	68.26
80	242.55	4.36	2.18	55.47

3.6.3 Numerical Quantification

An elastic-plastic-damage FE model [122] was implemented to more thoroughly investigate the yielding zone size and shape, along with the relative sizes of the constituent FPZ and PZ with changing DC. Model properties were fit directly from experimental data, and full details of the model setup are provided in *Materials and Methods* and in the Supplementary Materials. This model allows an estimate of the maximum possible FPZ and PZ size, as well as the fracture energy due to damage (G_f).

In this model, the process zones are considered to be fully developed when i) the first element at the crack tip reaches a stress-free state and ii) the stress gradient does not change as the crack propagates. The crack normal stress (σ_{xx}) at this instant is plotted against the

distance from the crack tip in Figure 3.11. The value of l_{ch} is taken to be the distance from the crack tip to the point of maximum stress or fracture stress ($\sigma_{fracture}$). In DC_{27} and DC_{80} samples, the l_{ch} values are found to be 2.4μm and 1.0μm respectively. In the DC_{17} samples, the small sample size did not allow the FPZ to fully develop, as indicated by the non-zero stress at the tip of the crack. To determine l_{ch}, a 120x scaled-up version of the beam was modeled, revealing an FPZ size of 115μm (Figure S6).

The PZ size is taken to be the distance from the peak stress in front of the crack tip (i.e., the end of the FPZ) to the point where $\sigma_{xx} = \sigma_y$ (Figure **??**). In the 26μm thick beams, plastic zones were found to have a considerable size of 14μm, 11μm, and 5μm for the DC_{17}, DC_{27}, and DC_{80} samples, respectively. It should be noted that the PZ was not fully developed for the DC_{17} sample here, and in 120x scaled simulations for the DC_{17} beam, the fully developed PZ size is found to be 165μm.

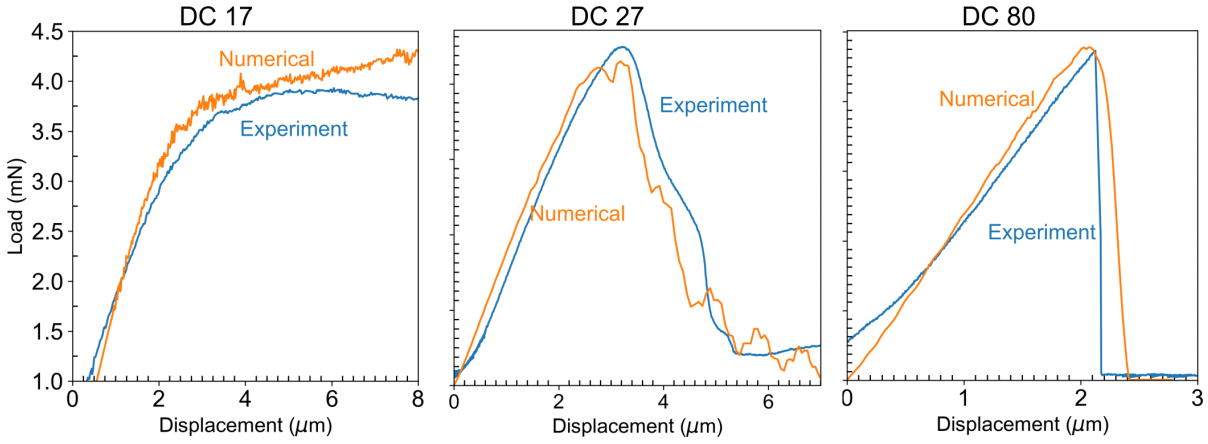

Figure 3.9: Comparison of load-displacement data obtained numerically post-calibration with the experimental data showing a good match between the elastic, plastic, and softening behavior.

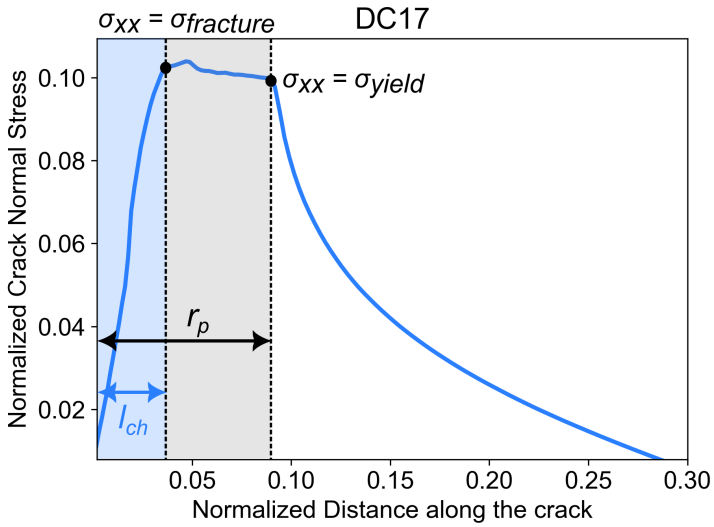

Figure 3.10: Crack normal stress normalized by yield strength as a function of distance from the crack tip normalized by length (120W-a) for DC_{17}, DC_{80}, and DC_{27} beams, respectively. The plots highlight the yielding zone (r_p) and the relative size of the FPZ (l_{ch}).

These results provide critical insight into how fracture behaviors change according to FPZ and PZ size. As the DC decreases from 80% to 17%, the FPZ and PZ size increase by ∼115x and ∼33x, respectively. This substantial size increase is most prominent in the DC_{low} specimens, and the change is more modest between the DC_{med} and DC_{high} specimens. These trends align with observed variations in strength and bending stiffness, which show a similarly steep increase in the DC_{low} regime (Figure **??**). Importantly, these results demonstrate that for the DC_{17} beams, both the FPZ and PZ are significantly larger than the 26µm experimental sample thickness. This indicates that the observed ductility in the DC_{low} specimens is the result of an underdeveloped yielding zone that does not meet the G_t required to cause fracture.

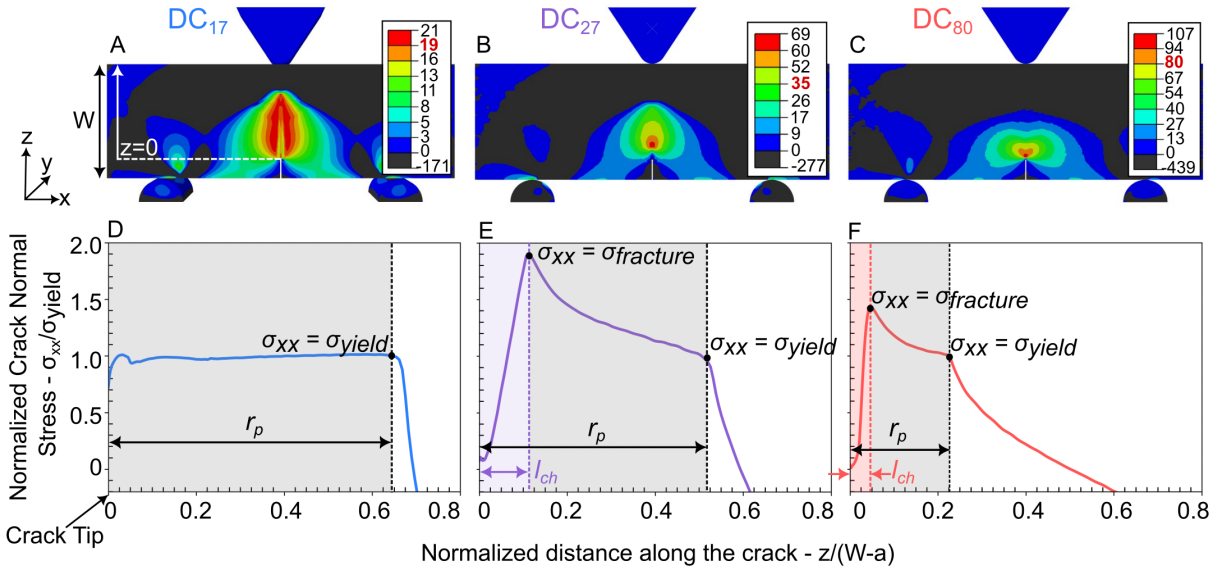

Figure 3.11: **Numerical modeling of FPZ and PZ** A, B, C: Crack normal stress (σ_{xx}) distribution in the mid-plane of DC_{17}, DC_{27} and DC_{80} W=26μm beams, after the yielding zone is fully developed. The bold-red value in the scale bar indicates the yield strength. D, E, F: Crack normal stress normalized by yield strength as a function of distance from the crack tip normalized by length (W-a) for DC_{17}, DC_{27} and DC_{80} beams, respectively. The plots highlight the yielding zone (r_p) and the relative size of the FPZ (l_{ch}).

Table 3.2: Total fracture energy (G_t), damage fracture energy (G_f), plastic fracture energy (G_p), FPZ (l_{ch}) and yielding zone (r_p) for different degrees of conversion (DC)

DC	G_t (J/m^2)	G_f (J/m^2)	G_p (J/m^2)	l_{ch} (μm)	r_p (μm)
17	-	90	-	115	280
27	68	28	40	2.4	11
80	55	18	37	1.0	5

3.7 Damage and Plasticity Governed Fracture

The relative contributions of the FPZ and PZ in the fracture of beams with varying DC can be further characterized by comparing the damage and plastic energy dissipation rate, G_f and G_p, respectively. The plastic energy dissipation rate G_p was determined by subtracting

the damage fracture energy G_f obtained from the FE model from the total fracture energy G_t determined from the SEL experiments (i.e., $G_p = G_t - G_f$), the results from which are shown in Table 3.2. We find that in the DC_{80} specimens, the plastic energy dissipation rate (G_p=37J/m^2) contributes ∼2x that of the energy dissipated via damage (G_f=18J/m^2), despite exhibiting very brittle failure. In comparison, despite an almost comparable plastic energy dissipation rate (G_p = 40J/m^2), the DC_{27} specimens have a slightly higher total fracture energy, mainly due to an increase in the damage energy dissipation (G_f = 28J/m^2). The DC_{17} specimens have a very high damage energy dissipation of G_f=90J/m^2, and likely have an even higher G_p, but it was not possible to estimate this value because SEL experiments were not conducted on these specimens. These relative changes in plastic and damage energy dissipation correlate well with the increased r_p and l_{ch} for lower DC samples.

It is interesting to note that the PZ size is larger than the FPZ size across all the DC values examined in this work. This, along with the consistent trend of $G_p > G_f$ for all the samples, indicates that the fracture behavior is more affected by plasticity than damage. However, this difference is not substantial enough to cause a purely ductile fracture at small scales, as illustrated in Figure 3.7. The fracture behavior of these photopolymers thus falls in an intermediate regime, where both softening and hardening ahead of the crack tip impact crack growth, warranting further analysis to understand the emergent size-affected behavior. This also suggests that the r_p and G_t values calculated using the SEL law in equation 3.1 and 3.2 might not be fully accurate and there is a need for improved SEL models for this intermediate regime that can capture this behavior more comprehensively.

Lastly, we note that the yielding zone sizes determined from the numerical model are comparable to the estimates obtained from the LEFM model for the DC_{med} and DC_{high} specimens,

but the DC_{low} LEFM estimate significantly underestimated the actual r_p size. This result is unsurprising given that the J_Q value obtained from the experiments is an underestimate of the actual G_t, but that the DC_{med} and DC_{high} specimens had a nearly fully developed r_p. The LEFM estimate nevertheless provided a quick and useful estimation of the characteristic material length scale that would be useful for predicting size-affected changes in properties.

3.8 Size-affected Ductility

To comprehensively understand the effect of changing both polymer composition and size, we evaluate the change in sample strength (σ_N) with sample size (D) in the context of an SEL analysis. The parameters to calculate the constituent material strength (σ_o) and transition fracture length (D_o) (equation 3.2), are determined from SEL experiments in combination

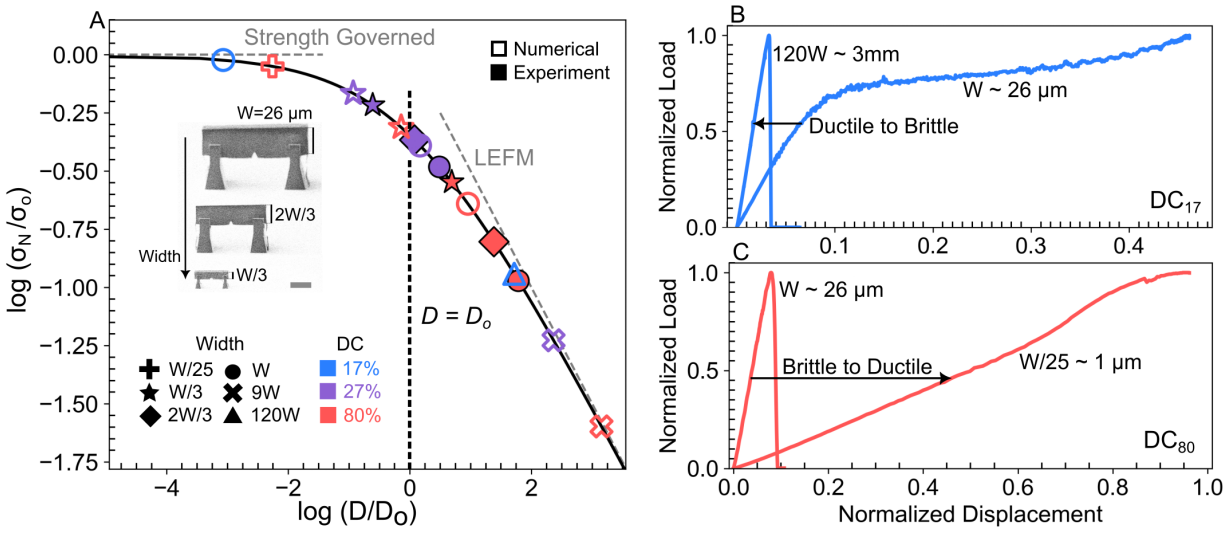

Figure 3.12: **LEFM vs. strength governed failure.** A) A SEL plot of nominal strength (σ_N) normalized by material strength (σ_o) vs. sample dimension (D) normalized by the transition fracture length (D_o). Experimental and numerical results are shown for different sample sizes and degrees of conversion. Scale bar: 10 μm. B) Ductile to Brittle transition in DC_{80} as the sample size is increased from 26 μm to 3 mm. C) Brittle to Ductile transition in DC_{17} as the sample size is decreased from 26 μm to 1 μm.

with numerical models, and normalized SEL data is shown in Figure 3.12. For structures of the same size (D = W = 26μm), comparing the sample strength to the material strength (σ_N/σ_o) revealed that decreasing the DC causes a transition from flaw-based to strength-based failure. For the DC_{80} specimens, the yielding zone is significantly smaller than the sample size ($r_p \ll D$), causing it to fall close to the LEFM-dominated regime of the SEL curve. In the DC_{27} specimens, the yielding zone size approaches the sample size but is still smaller ($r_p \leq D$), causing an observed transition from LEFM to strength-based fracture. The DC_{17} specimens are significantly smaller than the yielding zone size ($D \gg r_p$), falling well into the strength-governed fracture regime. It is clear from these trends that *ductility emerges when* $D \sim r_p$.

For structures of the same composition, the emergence of ductility at sufficiently small sizes and the emergence of brittleness at sufficiently large sizes was confirmed by further analyzing size effect experiments and doing additional numerical simulations for sizes that were not possible to fabricate experimentally. Experimentally scaled down DC_{80} specimens do not show pronounced ductility, possibly because the smallest possible beam thickness (W/3 = 8μm) was still larger than the r_p of these materials, but they do show a slower crack propagation velocity (Figure S7). Numerically modeled DC_{80} beams of size W/25 ($\sim$ 1 μm) exhibit ductility similar to the DC_{17} specimens (Figure 3.12). For DC_{17} specimens, a numerically modeled beam of size 120W ($\sim$ 3 mm) was found to show a characteristic brittle failure, indicating the significantly large r_p of this material. These results illustrate that *irrespective of the constituent material's composition, ductile or brittle fracture behavior can be controlled simply by changing specimen size.*

It should be noted that the slight discrepancy between the experimental and numerical results

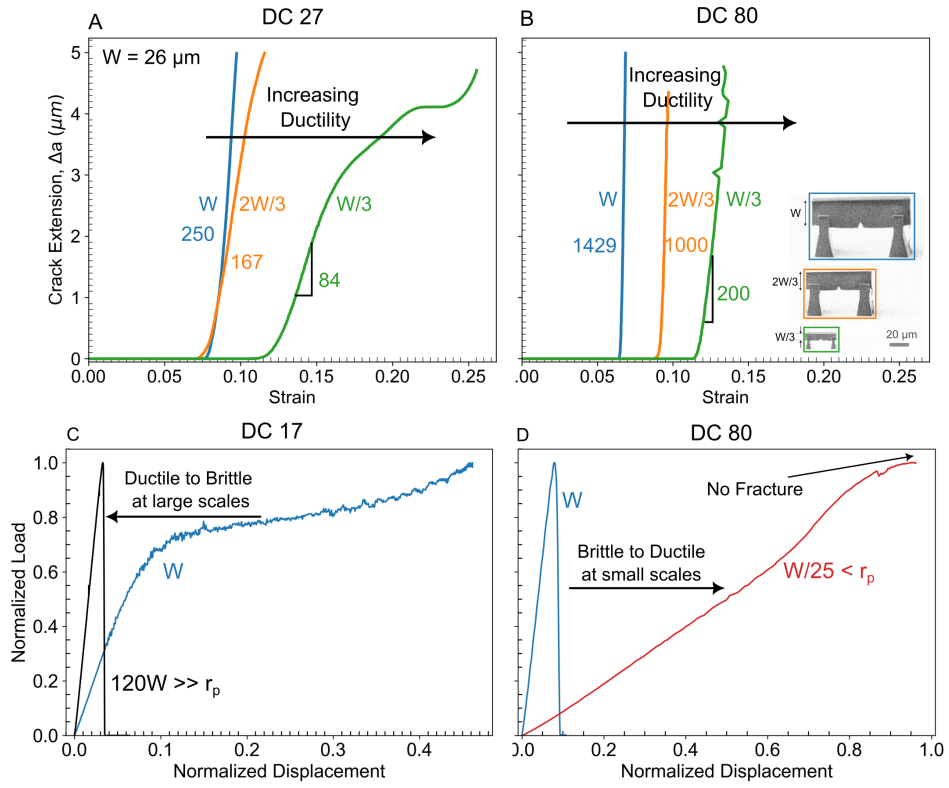

Figure 3.13: **Activating and De-activating ductility with size** A, B. Crack extension vs. strain showing decreasing crack growth rate with decreasing sample size, indicating increasing ductility in DC_{80} and DC_{27} samples, respectively. Values marked under sample size are the slope of the crack extension curve. Inset in B is an SEM image showing three geometrically scaled specimens used for the SEL study. C. Normalized load vs. displacement for DC_{17} samples showing brittle failure in a 120x scaled beam. D. Normalized load vs. displacement for DC_{80} samples showing ductile yielding a 1/25x scaled beam.

on the SEL curve results from different methods used to calculate r_p, namely the SEL method for experiments and a direct measurement for the FE models. Although simple size-effect laws developed from quasi-brittle materials (FPZ $\gg$ PZ) are useful understand the changes in fracture behavior in this study, the need for a full numerical model to quantify fracture energy, FPZ and PZ in these materials highlights the complex interplay between structural dimensions and material properties and reestablishes the need for improved size-effect models for when FPZ$\sim$PZ.

Chapter 4

ARCHITECTURAL LENGTH SCALES FOR MAXIMIZING TOUGHNESS

This chapter has been adapted from:

Patel, Zainab S., et al. "Architectural Length Scales for Maximizing Toughness" (In Preparation)

Contributions: Designed and fabricated the samples, conducted experiments, analyzed data, and wrote manuscript.

4.1 Chapter Summary

Increasing technological complexity demands a plethora of functional properties from materials, but they all need to be tough to survive any type of load and environment. While modern engineering approaches, such as bioinspired architectures and advanced processing techniques, have enabled the creation of tougher materials, they generally overlook the role of length scale and structural size effects on toughness. This work bridges this gap by developing design principles that harness both intrinsic (material) and extrinsic (architectural) fracture size effects to enhance fracture resistance. Using two-photon lithography and post-processing techniques, we develop layered polymeric materials where feature sizes (L) are smaller than the characteristic fracture length scale (r_p) to activate size-enhanced ductility and layer spacing is varied to increase architectural heterogeneity. In-situ nanomechanical testing revealed that increasing layer separation, i.e., creating confined layers, increased fracture energy by ∼5x compared to the parent material, unveiling diverse damage mecha-

nisms: brittle fracture without interlayer spacing, blunting, and deflection with moderately spaced interlayers, and 90° crack deflection with larger spacings. Notably, these materials do not show an appreciable loss in strength and stiffness up to an intermediate layer spacing. Employing material heterogeneity-based toughening models and macroscale tests on layered materials with $L >> r_p$, we systematically separated material and architectural contributions to toughness, highlighting the role of fracture length scale - maximum toughness is achieved only when both architectural feature size and structure size are smaller than their respective fracture yielding zones. These results underscore the pivotal role of architecture in preserving size effects and exemplify how a length-scale guided design approach can confer exceptional toughness and structural tunability, crucial for developing the next generation of advanced materials and understanding the exemplary properties of existing biological structural materials.

4.2 Background

All things break. Fracture is thus a problem across materials, industries, and length scales. Every material is understood to have a toughness and an associated fracture behaviour, for instance ceramics are typically considered to exhibit brittle failure and demonstrate low fracture toughness vs metals that are considered to be ductile and are known to be very tough. A common engineering strategy to escape this envelope is to combine different materials and create effective composite materials that overcome the limitations of the individual materials [119]. Natural materials like bone and bamboo routinely exemplify this strategy by combining a variety of soft and stiff materials in multi-scale hierarchical architectures [71, 68, 91, 130]. This endows them with exceptional strength and toughness, enabling them to serve as model systems for engineering mechanisms of toughness amplification. Although the exceptional properties of natural materials are hypothesized to originate from their small-

scale constituents and hierarchical architectures [58], the precise mechanics that govern the origins of such toughnesses are not understood, hindering complete utilization of bioinspired strategies.

The development of various bioinspired architected materials over the last two decades has significantly advanced our understanding of the mechanics of natural structural materials. Nacre-inspired glass exhibits toughness and ductility [91], bouligand-inspired CFRP composites successfully suppress brittle fracture [86], and bone-inspired composites demonstrate significant crack deflection and branching [79]. These examples show that the principle of architected toughness is really powerful and can help expand the existing material property space, yet there is very little literature on what fundamentally guides the design of such materials. A key missing insight is the length scale of the architectural building blocks used in such bioinspired designs. Natural materials are built over hundreds of years, and current fabrication tools are not sophisticated enough to replicate the precise structural hierarchy they exhibit. Therefore, it is crucial to understand the minimum feature size needed to activate unique toughening mechanisms and overcome the inherent brittleness of the constituents.

Understanding this first requires consideration of how fracture processes are affected by the size of the material [107]. Prior to fracture, materials will develop a yielding zone of length r_p in front of a crack, which comprises a fracture process zone (FPZ) of length l_{ch} and a plastic zone (PZ) of effective length $r_p - l_{ch}$ [98]. Samples larger than this yielding zone will undergo fracture-governed failure, while samples smaller than this yielding zone will undergo strength-driven failure. In the strength-driven regime, materials with a large PZ and small FPZ will experience ductile fracture, while materials with a small PZ and large FPZ will experience quasibrittle fracture. Many studies in this field, pioneered by Bažant, have explored the size-affected transition from fracture-driven to strength-driven failure, but they often focus on the nominal strength in quasi-brittle materials like concrete

and rock [19, 23]. Recent work on microscale polymers shows that both sample size and yielding zone size induce size-affected changes in fracture behavior and that structures smaller than the fracture-yielding zone suppress brittle fracture and exhibit ductility [107]. Further understanding of the preservation of such size effects is imperative to utilize this unique size-affected behavior in the design of real-life structures of any size.

4.3 Design of layered Materials

Layered polymeric materials were designed in a single-edge notch bend (μ-SENB) configuration. To study the role of feature size on the final toughness of an architected material, layer thicknesses (L) in all samples were chosen with respect to the size of the constituent material's fracture-yielding zone ($\mathrm{r_p}$). Small-scale samples made using two-photon lithography and atomic layer deposition had $\mathrm{L} < \mathrm{r_p}$, and large-scale samples made using digital light synthesis had $\mathrm{L} > \mathrm{r_p}$.

Any additive manufacturing technique introduces stiffness gradients based on print paths, which are used in this study as a means to increase architectural complexity. This is because stiffness-based heterogeneity can lead to significant toughening governed by the relationship:

$$\mathrm{f_{inh}} = \Psi(\mathrm{L},\mathrm{h})\frac{\mathrm{E_{max}} - \mathrm{E_{min}}}{\mathrm{E_{max}} + \mathrm{E_{min}}} \tag{4.1}$$

where $\mathrm{f_{inh}}$ is the inhomogeneity factor that relates to the toughness of the architected material $\mathrm{J_f}$ as $\mathrm{J_f} = \mathrm{J_{material}}(1+\mathrm{f_{inh}})$, $\Psi(\mathrm{L},\mathrm{h})$ is a structure geometry factor, and $\mathrm{E_{max}}$ and $\mathrm{E_{min}}$ are the maximum and minimum stiffnesses, respectively. Following this, layers are printed with high in-plane overlaps to minimize stiffness gradients in the layer, but out-of-plane overlapping (S) is varied to create structures with very small to very large stiffness gradients in front of the crack tip.

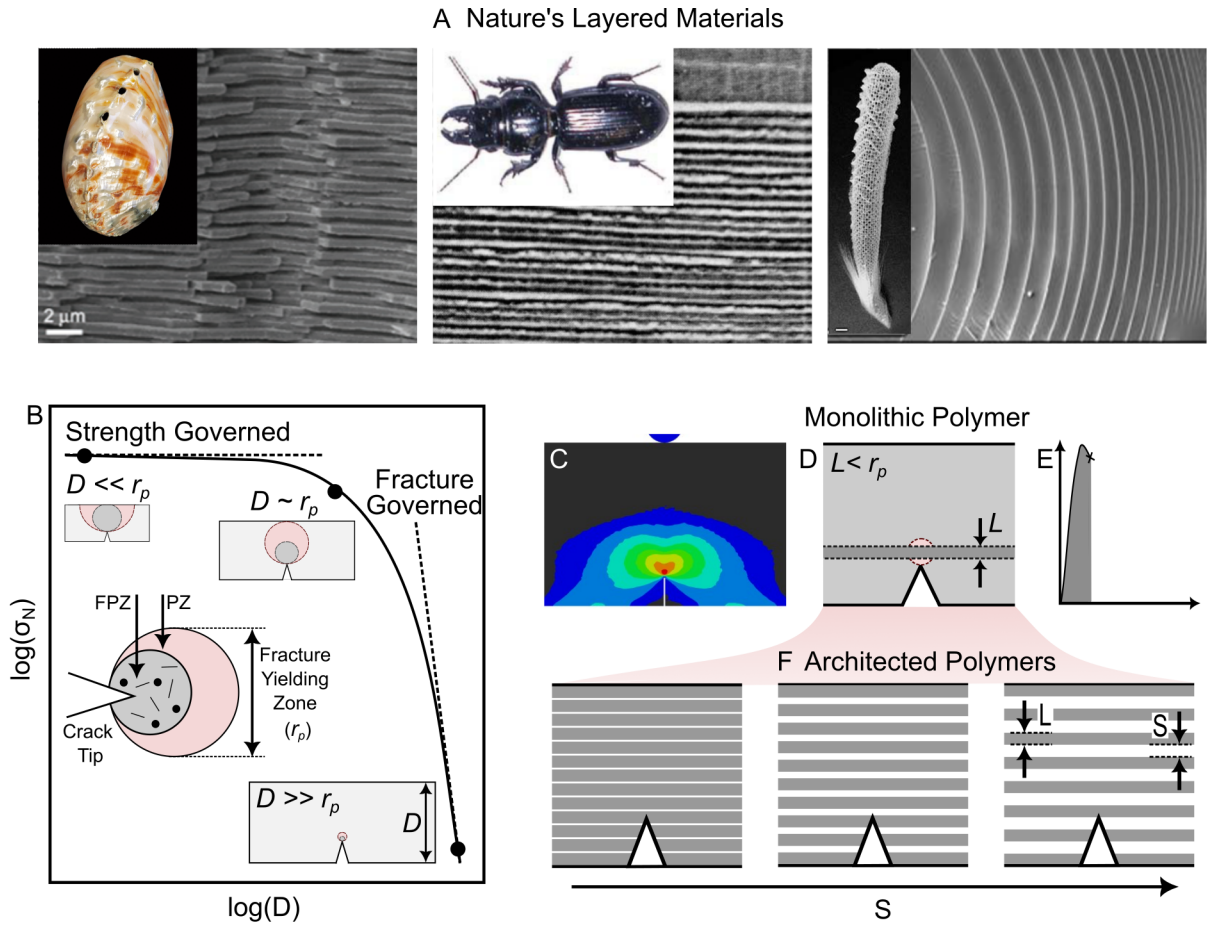

Figure 4.1: **Designing features using fracture size effects** A. Nature's layered materials abalone shells (Nacre) [13], beetle shells [76] and deep sea sponge [1] B. Nominal strength vs. feature size plot showing the transition from fracture-governed to strength-governed failure. C. Size of the fracture yielding zone (r_p) in the parent material. D. Layer thickness (L) smaller than r_p. E. Brittle fracture in the constituent material. F. Architected layered polymers with varying layer spacings (S).

4.3.1 Micro-layered Polymers

Samples were fabricated using two-photon lithography (TPL) direct laser writing and printing parameters were optimized to achieve a final elliptical TPL voxel with width (w) $\sim$ 450 nm and height (h) $\sim$1600 nm. Layer thickness in all samples (L) was chosen to be equal to the height of an individual voxel ($L = h$) so that it is smaller than the fracture-yielding zone of the polymer ($r_p = 5\,\mu m$), which was characterized in a previous study [107] and is shown in Figure 4.1.

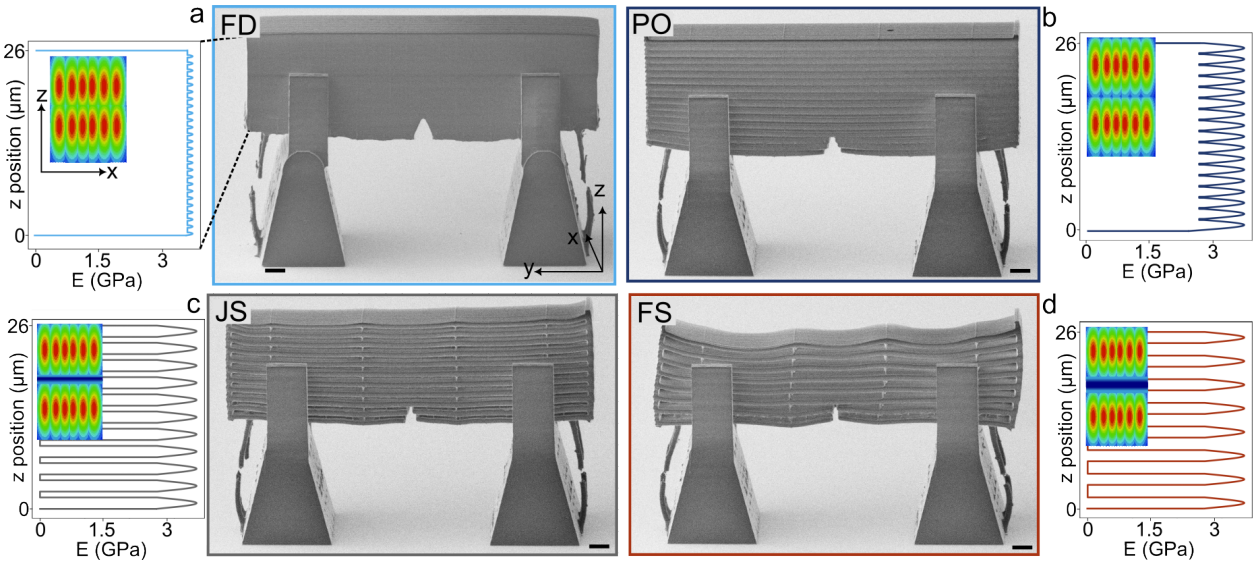

Figure 4.2: Stiffness Gradients in micro-layered beams: A. Fully dense beam with minimal stiffness variation. B. Partially overlapped beam. C. Just separated beam with significant variation. D. Fully separated where layer and spacing is comparable.

TPL voxels typically have a Gaussian power gradient [15], resulting in continuous gradients in polymer crosslinking and stiffness across the voxel. Although the gradients within the voxel can be minimized to some degree by ensuring large laser exposure, in the extreme case, the core of the voxel or the region with the maximum crosslinking has stiffnesses between E_{max} = 3.5-4 GPa, and the outermost edge of the voxel with the least crosslinking

has stiffnesses between E_{min} = 1.2-1.5 GPa. Changes in the in-plane and out-of-plane voxel to voxel overlap, thus resulting in diverse gradients or heterogeneities [108].

To create a controlled 1D stiffness heterogeneity across the thickness of the beam (i.e., in the z-direction), high TPL exposures were used to minimize the power gradients within the voxel, and high in-plane overlap between lines was ensured to minimize in-plane heterogeneity. Out-of-plane spacing (S) was varied from high-overlap (S = *-0.6* μm) to create fully dense homogenous beams (E_{min}/E_{max} = 1) to high-spacing (S = *2.3* μm) to create fully separated layers (E_{min}/E_{max} = 0 - 0.3). It is important to note here that an $S > 0$ does not necessarily imply separated layers in fabricated samples due to memory effects during writing. This causes bridge segments to form between layers, the size of which decreases with increasing S. Based on this, these structures have been split into four categories: fully dense (FD) with S = *-0.6* μm, partially overlapped (PO) with S ranging from *-0.3 - 0.3* μm, partially separated (PS) with S ranging from *0.5 - 1.1* μm, and fully separated (FS) with S ranging from *1.1 - 2.3* μm (Figure 4.2).

μ-SENB beam dimensions were determined according to ASTM E-1820b [41] with a standard beam thickness of W = *26* μm and span-to-thickness ratio S/W = *2*. Notches were directly written into the beams during the printing process to avoid introducing any focused ion beam (FIB) milling damage [8]; these had an initial length a_o = *4.5* μm and an a/W = *0.17*. Four horizontal 'spacers' were printed between layers along the breadth of the beam to ensure separation between highly spaced layers and prevent sagging. These were written with a very low laser exposure to ensure minimal contribution to the fracture of the beam. An additional study was conducted to find the maximum no. of such horizontal support bars that can be printed without significantly altering crack propagation (Figure 4.3).

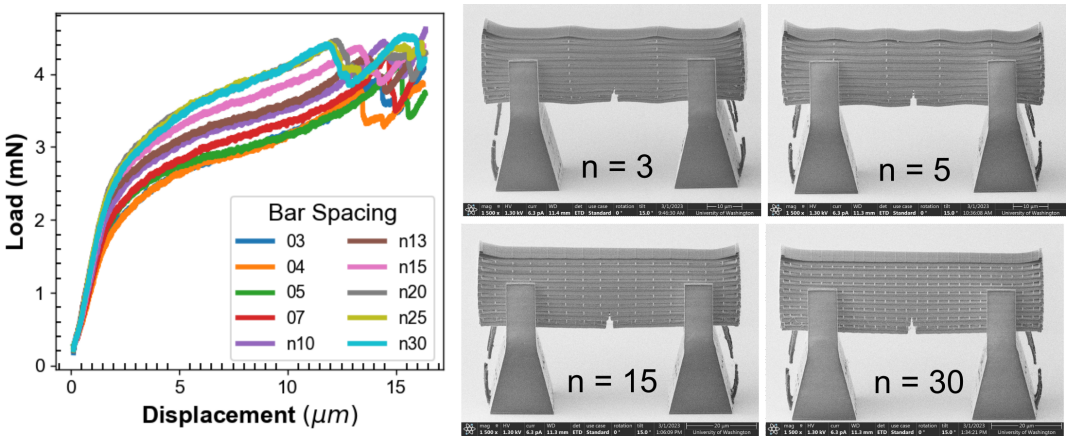

Figure 4.3: Effect of Support Bars on Fracture: (Left) Load vs Displacement plot showing that behavior is not affected when number of bars is less than five. (Right) SEM Images showing fabricated samples.

4.3.2 Macro-layered Polymers

To understand how toughness amplification changes when L >> r_p, large-scale layered SENB samples were fabricated using Digital Light Synthesis (Carbon 3D) with a photoplastic - Loctite IND147 black. This material has a Young's modulus E = 3.2GPa and tensile yield strength σ_{ys} = 67MPa, matching closely with the DC 45 IP-Dip material used to create the microscale beams with L < r_p. The fracture yielding zone for this material was found to be r_p = 60μm, so layers with thicknesses L ∼ 10 ∗ r_p were fabricated to completely eliminate fracture size-affected toughening. Layer-to-layer separation (S) was varied between 0 - 1.2 mm to create structures that are fully dense, partially overlapped and completely separated. A sparse hexagonal interlayer array was used to separate layers and SENB geometry W = 18.5 mm, S/W = 3, a = 11 mm, and a/W ∼ 0.6 was used. Cracks were directly printed into the beam eliminating defects and variations arising from creating a pre-notch.

4.4 Mechanical Testing

Large-scale mechanical testing was conducted on the Instron with a custom-made 3-point bend setup at quasi-static strain rates of 0.2 mm/sec. In-situ fracture experiments for μ-SENB samples were performed using a displacement-controlled mode in a piezo-driven nanomechanical system, details of which can be found in Materials and Methods. Specimens were tested either to complete fracture or to a displacement of 18 μm and video data was captured for each test, representative stills of which are shown in Figure 4.5. Instantaneous load line stiffness was calculated using the unloading slope of the CSM data, and crack initiation was determined as the point where the unloading stiffness began to decrease. Crack lengths were obtained using a compliance calibration procedure [55] by correlating the crack initiation point with the instantaneous stiffnesses thereafter. Determining crack initiation was particularly challenging for the *FS* beams, where no significant drop in stiffness was

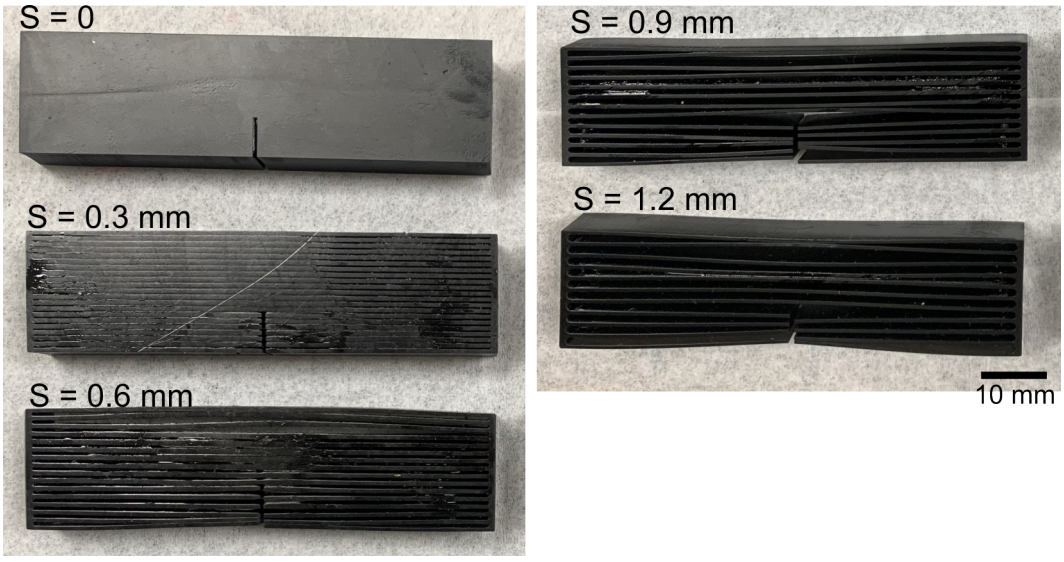

Figure 4.4: **As fabricated Macroscale Samples**: Layer thickness (L) = 0.6 mm and Layer spacing (S) was varied between 0-1.2mm.

observed. Video data was used in this case to approximate a point of crack initiation to calculate initiation fracture energy. An elastic-plastic Mode-I J-integral was used to determine the fracture behavior and crack growth resistance (J–R curve) of the samples as defined in ASTM E1820-20b [41]. To meaningfully quantify fracture energy, we compare the J value at a crack growth equivalent to one layer crack extension and is denoted here as J_{1L}. This definition of J_{1L} allows for a direct comparison of the fracture energy at a consistent amount of crack growth and is not meant to serve as a standard method for calculating material fracture energy.

4.5 Results

4.5.1 Micro-layered Polymers

Representative load-displacement data for μ-SENB tests on FD, PO, JS, and FS beams are shown in Figure 4.5, and data for all tested beams are shown in Figure 4.6. Both bending stiffness and peak load predictably decrease with increasing layer spacing, ranging from 0.5-2.2 kN/m and 3.9-10.5 mN, respectively. As compared to the parent material (FD), the PO samples demonstrate marginal drops in peak load and bending stiffness, whereas the FS samples demonstrate a significant decrease in both.

J-R crack resistance curves are analyzed to understand changes in failure behavior, as shown in Figure 4.5. The FD beams show a high peak load but undergo catastrophic failure, and J-integral curves are seen to plateau at $\sim$ 65 J/m^2. This indicates that the fracture-yielding zone in this material is fully developed, leading to brittle fracture as governed by linear elastic fracture mechanics (LEFM). The PO beams show an $\sim$2x increase in strain to failure with minimal reduction in peak load as compared to the FD beams. These beams demonstrate slower crack propagation as compared to the FD beams, yet they fracture completely. J-R curves rise initially but eventually plateau, meaning that fracture behavior

is starting to deviate from LEFM-type fracture. Toughness increases from $\sim$ 85 to $\sim$200 J/m^2 as layer spacing increases from -0.3 - 0.3 μm. The JS beams show a clear start-stop behavior in the crack growth as the crack stops after propagating through every layer before reinitiating in the next layer. This can be seen clearly in 'step' behavior in the load-displacement and J-R curves, resulting in significant increase in fracture resistance sim 300 J/m^2. These J-curves did not plateau hence, we estimate the total fracture energy of these materials to be significantly higher.

The FS beams show a complex mixed-mode fracture behavior, leading to pronounced toughening. Similar to the JS beams, the crack propagates in a 'start-stop' manner, reinitiating at every interface, but the crack tip also exhibits blunting, and the crack grows in the

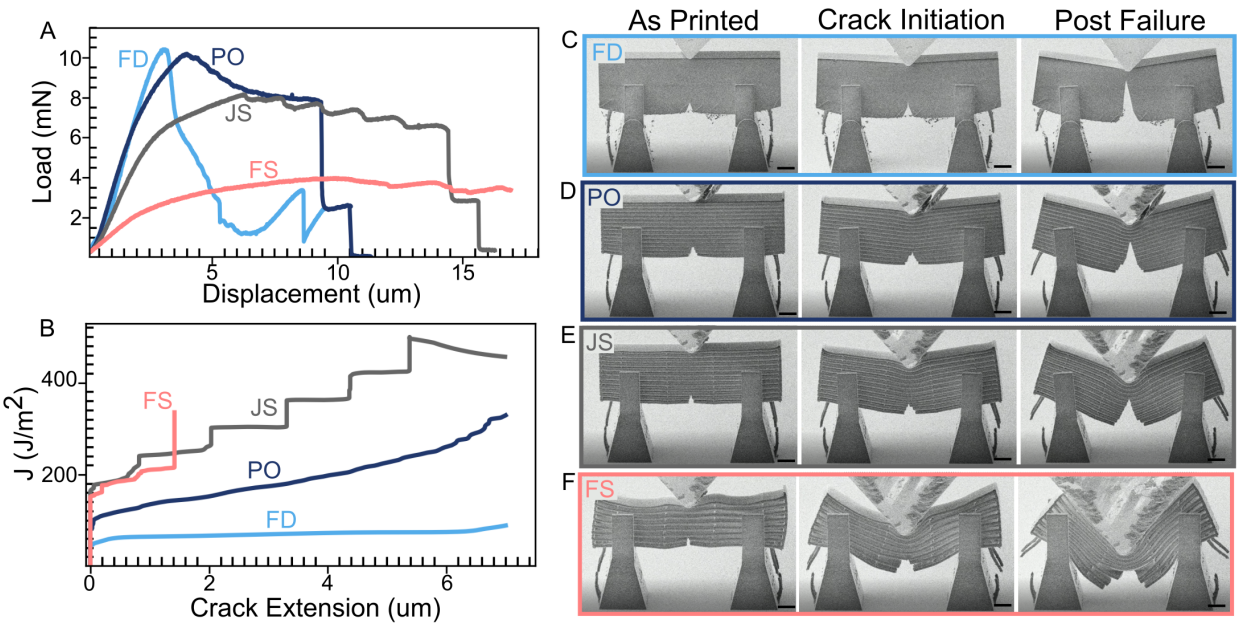

Figure 4.5: **Fracture in Nano-layered Samples**: a. Load vs displacement behavior, b. J-R crack growth curve of FD, PO, JS, and FS samples. c,d,e,f - sequence of images going left to right showing SEM images of the layered beams as printed, after crack has initiated in the first layer and after final fracture for FD, PO, JS, and FS samples, respectively. Scale bar: 10 μm

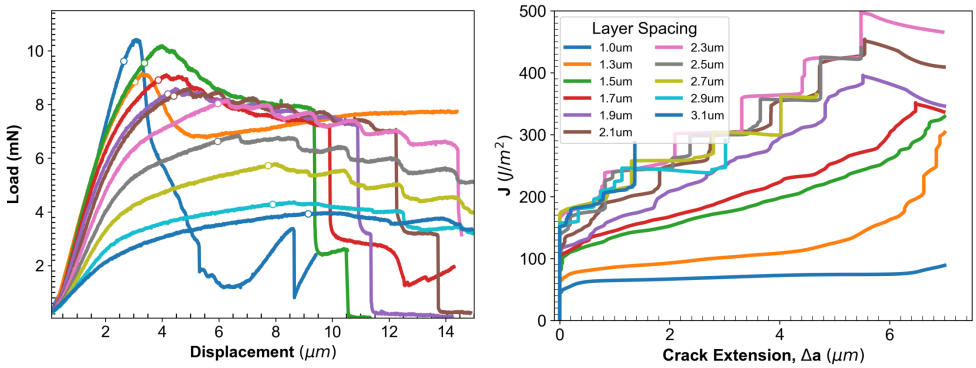

Figure 4.6: **Nanomechanical Data:** Load-displacement and J-R curves for samples with layer spacing (S) between 1 - 3.1 μm.

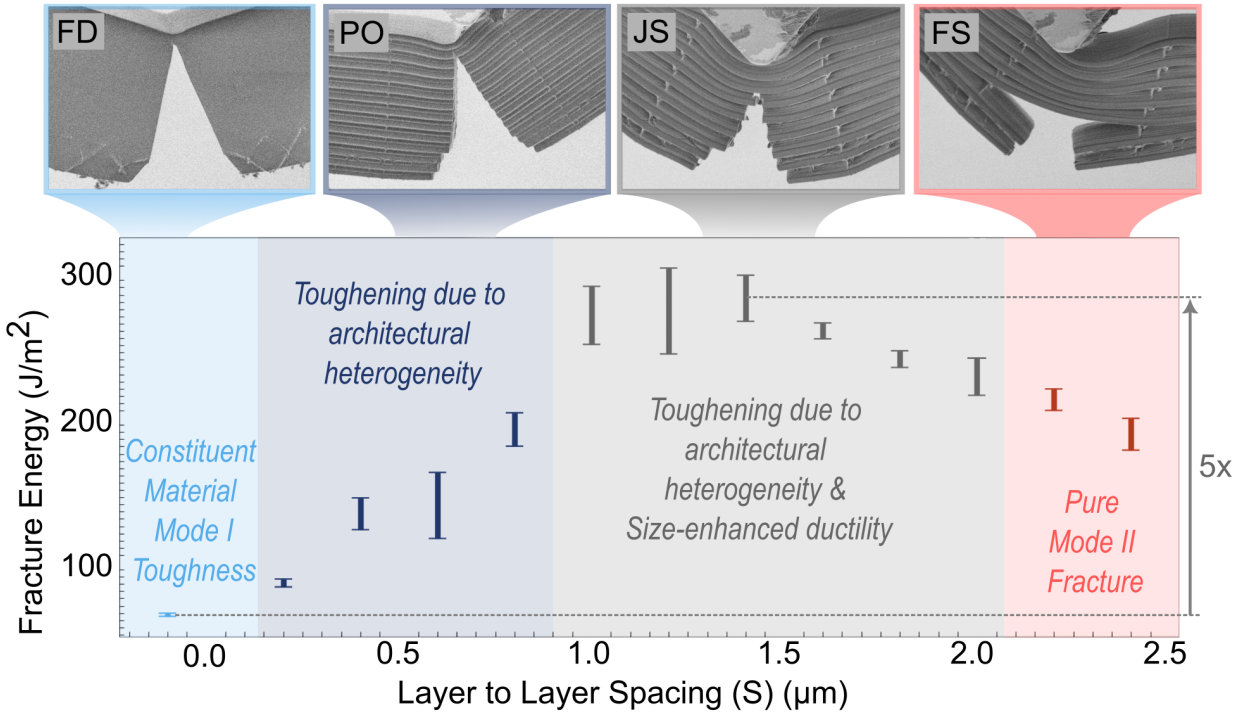

Figure 4.7: **Fracture Energy of micro-layered Materials**: J_{1L} vs S plot showing fracture energy and resultant toughening mechanisms for different μ-layered materials. Insets show representative images of the beam front after test completion.

plane before propagating to the next layer. This blunting behavior is observed to increase with S. In the extreme case where S = 2.1 μm, the large interlayer separation prevents the crack from propagating at all; as a result, the crack completely deflects along the interface and propagates in a pure mode-II manner. All FS samples demonstrate large plastic plateaus with significantly enhanced strains to failure, and at displacements > 18 μm, the sides of the indenter tip start touching the top edge of the beam, at which point the test becomes invalid, meaning that these beams cannot be taken to final fracture with the current specimen geometry.

One notable feature of these micro-layered materials is that the peak load does not drop significantly with increasing layer spacing or decreasing density upto an intermediate layer spacing. An substantial increase in toughness almost always corresponds to a significant drop in the strength of the material, but utilization of size-enhanced ductility helps maintain strength while amplifying toughness.

Comparing the J_{1L} values for all samples, we observe a remarkable ∼5x increase in toughness as compared to the parent material (Figure 4.7). It is important to note that the ∼5x factor is an underestimation of the maximum toughness amplification since the enhanced ductility and mixed-mode crack propagation complicate the J-integral analysis for the JS and FS samples and do not give accurate values. Nevertheless, four distinct toughening regimes are observed. Since the layers are still merged in the PO samples, toughening originates from the creation of stiffness heterogeneity (f_{inh}) ahead of the crack tip, which increases with S [68, 42]. Once the layers separate (i.e., JS samples), we see a jump in the J_{1L} vs. S curve, indicating the activation of another toughening mechanism. We hypothesize this enhanced toughening in the JS samples comes from the activation of size-enhanced ductility in the sufficiently small layers. To discern if the enhanced toughening is due to the size effect or simply an effect of the architecture, we analyze large-scale layered samples where

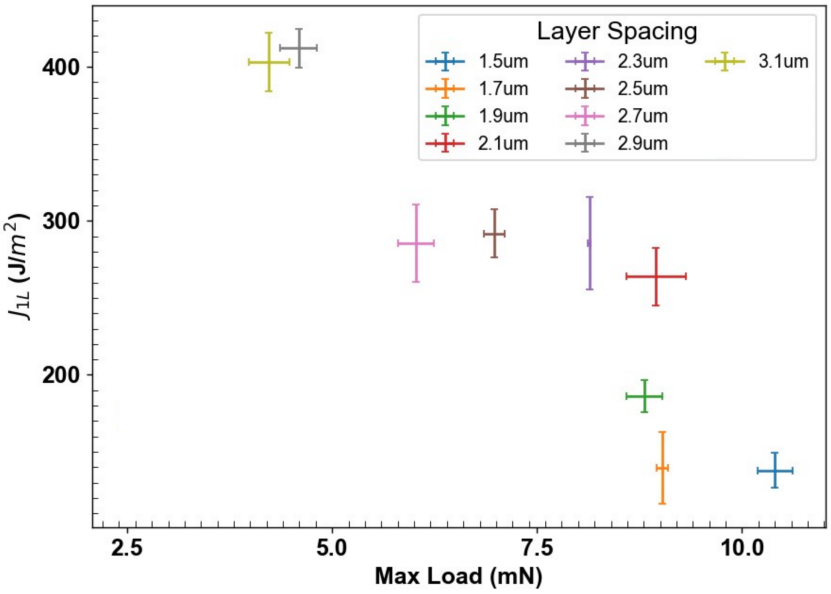

Figure 4.8: Toughness vs max load showing optimization of both strength and toughness with decreasing relative density

size-enhanced ductility is not activated.

4.6 Fracture in Sufficiently Large Layers

To understand how toughness amplification changes when L >> r_p, large-scale layered SENB samples were fabricated using Digital Light Synthesis (Carbon 3D) with a photopolymer - Loctite IND147 black. Fracture experiments reveal trends similar to the samples with L < r_p. Both peak load and stiffness decrease while toughness increases with increasing S. When layers are completely separated, crack growth occurs in a start-stop manner as the crack reinitiates at every interface, resulting in enhanced toughness. However, the key difference was that all samples experienced brittle fracture irrespective of S. In samples with large S values, initial crack propagation was hindered by creation of a layered architecture, but after crossing peak load, the crack instantaneously propagated through the rest of the sample.

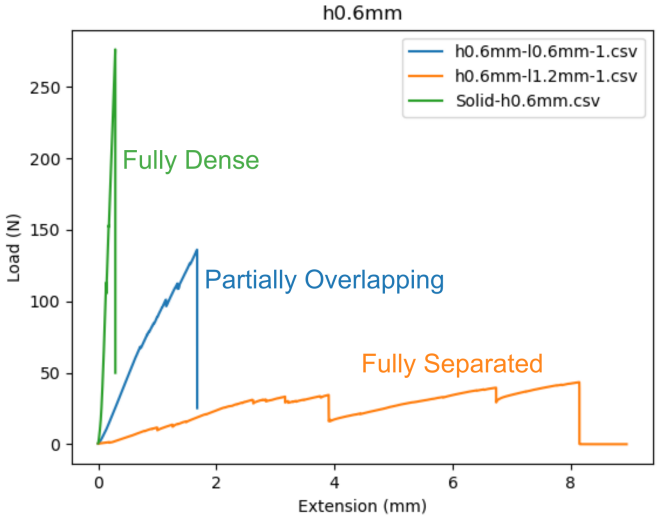

Figure 4.9: **Load vs Displacement Data for Macroscale Layered Materials**: Data for FD, PO and FS samples with L=0.6 mm and S = 0, 0.6 mm and 1.2 mm, respectively, showing emergent ductility but ultimate brittle fracture.

4.7 Size-Affected Material Toughening

For a crack propagating through two dissimilar materials, there are three possibilities when it reaches the interface: propagating through the interface, deflecting at the interface, or getting arrested. Which of these occurs depends on the material and interfacial fracture energy, and the crack will always choose a path of least resistance or lower toughness [90]. In both the macro- and micro- layered materials here, as the layer separation increases, the interface toughness decreases, hence, it becomes easier for the crack to deflect than to penetrate. This deflection amplifies toughness, as already known from analytical studies and from fracture in naturally occurring architected materials [90, 36, 1]. If the toughening in the micro-layered materials was completely due to this architectural effect, we would see comparable toughness amplification between the macro- and micro-layered materials given comparable layer thickness to spacing ratios.

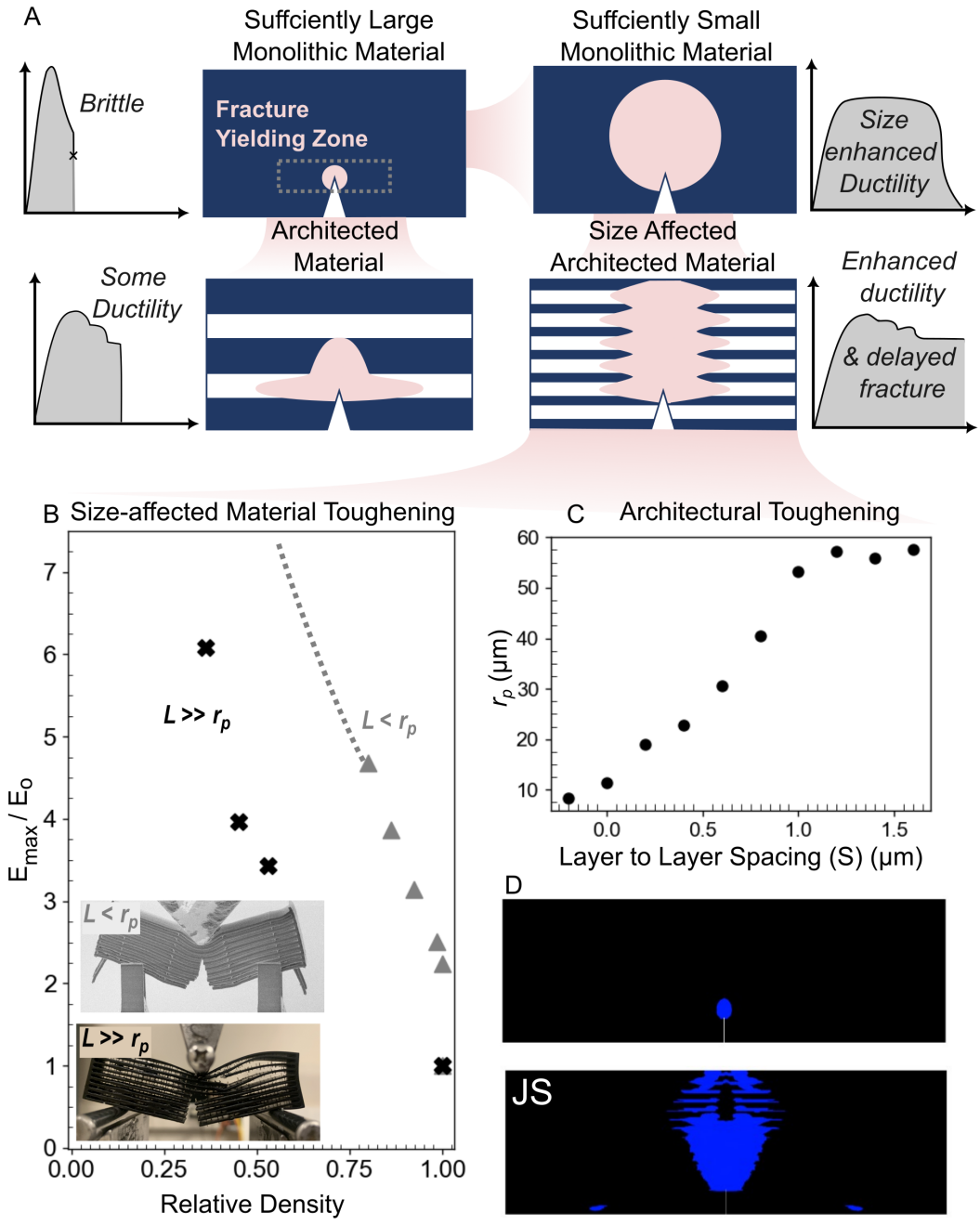

Figure 4.10: **Cascading Material and Architectural Toughening Mechanisms**: A. Illustration showing how designing architected materials at the right feature size enhances ductility and toughness. B. Normalized work of fracture vs relative density for macro- and micro- layered materials. Inset: post-fracture images. C. Effective r_p of micro-layered materials. D. FE images showing r_p in FD and JS samples.

Comparing the work of fracture (E_{max}) of the macro- and micro-layered materials to that of the parent material (E_o) highlights some notable differences. Figure 4.10 reveals that although the creation of an architecture amplifies toughness in both cases, architecture with size-affected constituents shows significantly enhanced toughness and overall delayed fracture. Although the large ductility for many of the low relative density micro-layered samples prevented the quantification of total fracture energy, but the high relative density data points already show how much more toughness amplification is possible simply with the right feature size.

Each fiber can be thought of as a crack-bridging element. For the IP-Dip material comprising the micro-layered materials, we estimate the bridging toughness to increase from 70 J/m^2 to 150 J/m^2 going from bulk to nanofiber, respectively [15, 62]. If the size of the fiber is significantly larger than the size of the fracture-yielding zone ($L >> r_p$), then the toughness of the layered materials will increase with increasing S due to crack deflection, yet it wouldn't utilize the maximum material toughness available from the fibers. When fibers are sufficiently small ($L < r_p$), as the layers get fully separated, toughening doesn't only occur because of crack deflection, but also due to delayed penetration, resulting in larger toughness amplification. *Thus, architecture at the right length scale is key to fundamentally engineering toughness in any material.* Gradually increasing layer spacing suppresses the catastrophic failure and induces ductility in the system. In contrast, in the macro-layered materials with $L >> r_p$, toughness increased with S without significant ductility and overall catastrophic failure.

4.8 Architectural Toughening

Lastly, it is important to comment on the role of architecture on the effective toughness. Using the fracture energies calculated from μ – SENB experiments and yield strength from

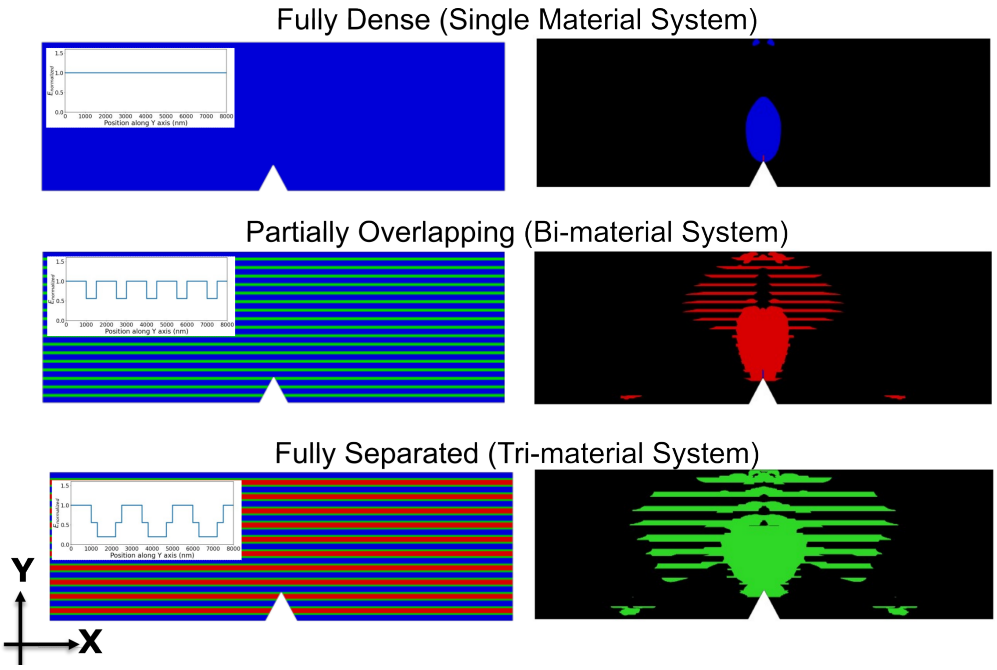

Figure 4.11: **Fracture Yielding Zone of Architected Materials**: Numerical model and resultant fracture yielding zone shape and size of FD, PO and FS samples showing a growing anisotropic r_p with increasing architectural heterogeneity.

three-point bending experiments on unnotched samples, we estimated the effective r_p of the micro-layered materials, as shown in Figure 4.10C. We see that r_p increases with increasing S, approaching and expanding beyond the size of the sample. From a fracture size-effect perspective, the enhanced ductility of samples with larger S could also be understood from the fact that the effective r_p of these materials is larger than the width of the beam. Additional Finite element elastic-plastic-damage modeling was done to understand the shape of these emergent r_ps, as shown in Figure 4.11.

4.9 Origins of Toughness in Natural Materials

This work also helps us understand the remarkable toughness observed in many natural structural materials. For instance, Nacre or abalone shells are primarily composed of brittle aragonite yet exhibit significant damage tolerance. They are composed of layers or tablets of aragonite that are $L \sim 400$ nm thick and stuck together with a soft protein glue. This stiff-soft composition of nacre has long been hypothesized as the primary driver of its remarkable toughness resulting in mechanisms like tablet sliding and crack deflection. Despite understanding the diverse toughening mechanisms, nacre-inspired artificial materials have still not been able to achieve that level of toughness amplification. This is in part because the constituent materials and length scales used in such bioinspired materials design endeavors are usually arbitrary. Using the fracture energy ($J_{IC} = 10$ J/m^2) and yield strength ($\sigma_{ys} = 160$ MPa) reported in previous works [12], we estimate the fracture yielding zone for aragonite to be $r_p \sim 3$ μm, meaning that the nacre tablets are sufficiently small ($L < r_p$) to activate size enhanced ductility and suppress catastrophic failure characteristic of the constituent aragonite. Moreover, if we calculate the effective r_p of nacre ($J_{IC} = 1.5$ kJ/m^2, E = 70 GPa, $\sigma_{ys} = 75$ MPa), we find it to be ~ 3 mm, approaching the typical thickness of nacre shells [12]. Nature thus combines both architecture and material at the right length

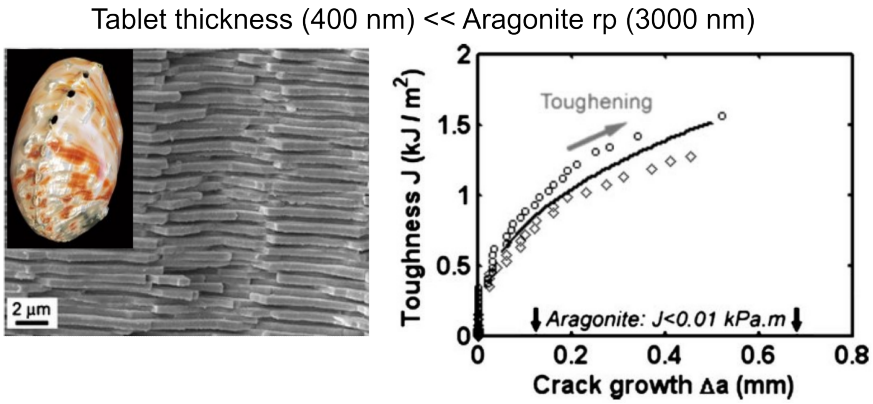

Figure 4.12: **Toughening in Nacre** Nacre microstructure, toughness of constituent aragonite and nacre.

scale to create damage-tolerant structures from any starting material.

4.10 Continuous and Discontinuous Micro-layered Composites

4.10.1 Design

μ-SENB polymeric beams fabricated using two-photon lithography were coated with ALD alumina (E $\sim$ 164GPa) to further alter the E_{min}/E_{max} ratio and understand the change in resulting toughness. Samples were conformally coated with Al_2O_3 using an ALD process (Picosun R-200). The chamber was held at 50°C with a recipe consisting of pulsing H_2O for 15 ms, purging for 20 s, pulsing trimethyl aluminum for 15 ms, purging again for 20 s, and repeating the process for the desired layer thickness. The system was run for 200 cycles (corresponding to 25 nm) with N_2 as the carrier gas at a flow rate of 20 sccm.

4.10.2 Results

Load-displacement data for μ-SENB tests on FD, PO, JS, and FS composite beams are shown in Figure 4.13. Both bending stiffness and peak load predictably decrease with increasing layer spacing, ranging from 0.36-1.9 kN/m and 2.1-10.5 mN, respectively.

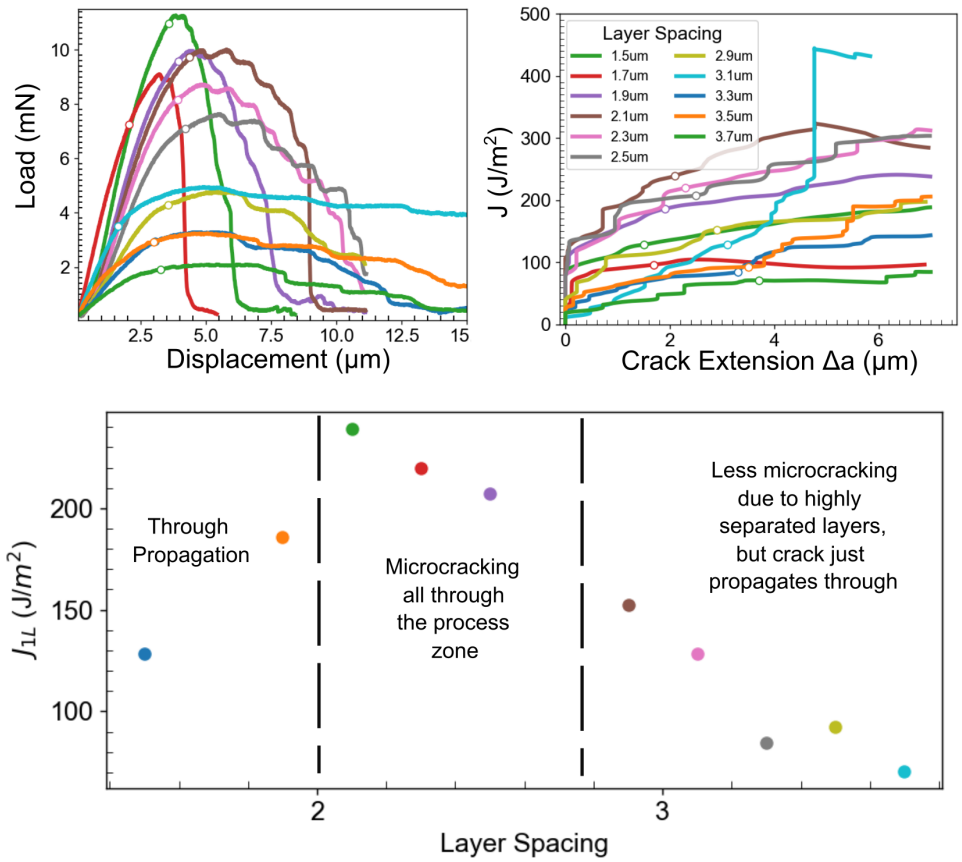

Figure 4.13: **Nanomechanical Behavior of micro-layered composite beams:** (Top left) Load vs displacement for different layer spacings (Top right) J vs crack extension for different layer spacings (Bottom) J_{1L} vs layer spacing showing transition in fracture behavior.

J-R crack resistance curves are analyzed to understand changes in failure behavior, as shown in Figure 4.13. The PO beams break completely, but the fracture is stable, and the crack gradually grows through the beam. J-R curves do not show a rise like the pure polymer PO beams, probably caused by the presence of brittle alumina. Toughness increases from $\sim$ 85 to $\sim$200 J/m^2 as layer spacing increases from 1.0 - 1.9 μm. The JS beams show microcracking around the crack tip and some start-stop behavior in the crack growth, seen clearly in 'step' behavior in the load-displacement curves. This results in rising J-R curves

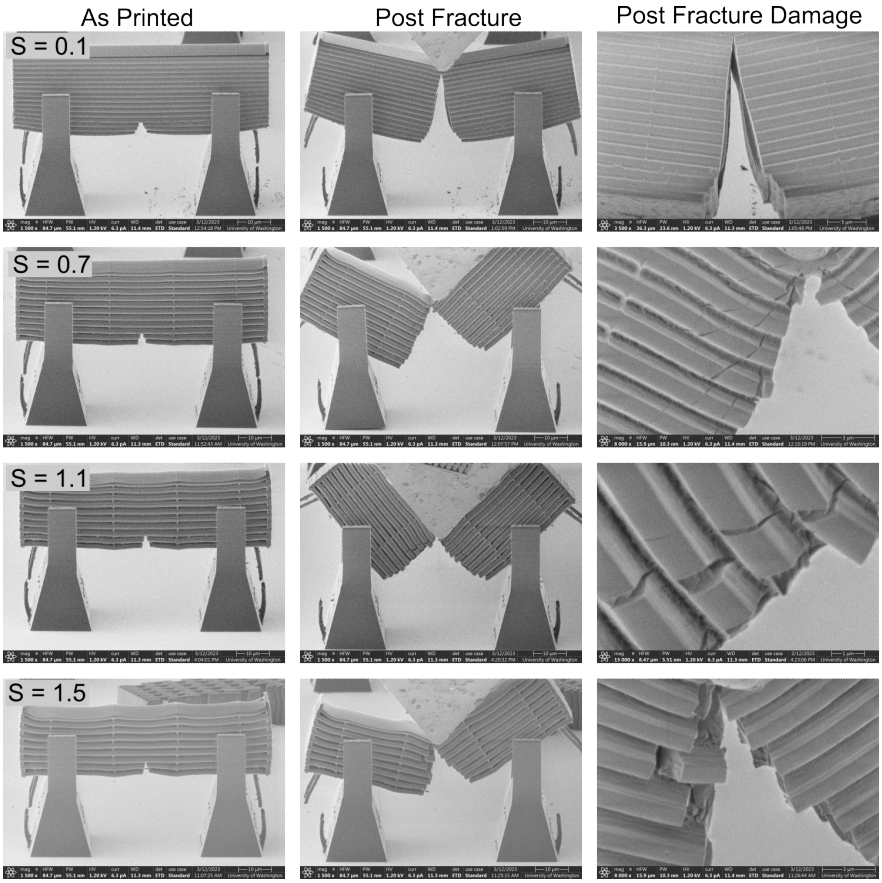

Figure 4.14: **Fracture in micro-layered composites**: SEM images showing before and after testing as well as a magnified view of the crack region in polymer alumina composite beams with S = 0.1, 0.7, 1.1 and 1.5 μm.

which eventually plateau, leading to enhanced fracture resistance ~ 250 J/m^2.

The FS beams show a complex mixed-mode fracture behavior and demonstrate considerable ductility. Unlike the JS beams or the pure polymer FS beams, the crack does not propagate in a 'start-stop' manner. Instead, we observe significant micro-cracking around the crack tip (Figure 4.14), leading to layer fracture, and the entire sample breaks eventually. Further analysis is needed to fully understand the behavior of these multi-material systems.

Chapter 5

TOUGHENING BY INTERPENETRATING LATTICES

This chapter has been adapted from:

Patel, Zainab S., et al. "Anistropic Fracture in Ductile and Brittle Nanoarchitected Interpenetrating Lattices" (In Preparation)

Contributions: Designed and fabricated samples, conducted experiments, analyzed data, and wrote manuscript.

5.1 Chapter Summary

In this chapter, we explore how the idea of size-affected (intrinsic) and architectural (extrinsic) toughening can be applied to traditional lattice materials. Fracture Toughness in lattices decreases with unit cell size and relative density, presenting significant challenges in the development of lightweight damage-tolerant structures. We develop nano-interpenetrating lattices (n-IPLs) by weaving two separate lattices through the same volume and change the constituent composition to create n-IPLs with and without size-enhanced ductility. It is hypothesized that the different preferred crack growth paths of the sublattices will enlarge the effective fracture yielding zone size of the n-IPL, which will be further amplified by the use of size-controlled constituents. n-IPLs are fabricated using two-photon lithography and designed in a micro-single edge notch bend (μ-SENB) configuration with relative densities $\overline{\rho}$ between 15% to 30%. Experiments demonstrate that n-IPL architecture with preserved size effects not only increases toughness but significantly delays crack initiation, creating a path-

way to engineering lightweight fracture-resistant structures from a single effective material.

5.2 Background

Lattices are an ideal model system for creating architected materials due to their straightforward definition, versatile design possibilities, and the availability of existing architectural libraries. The recent surge in additive manufacturing techniques has not only increased the use of lattice materials but also broadened the range of manufacturable designs. As lattices become more prevalent in real-world structural applications, research and development efforts are increasingly focusing on material properties beyond just strength and stiffness, like toughness. Due to their geometric complexity and the imperfections inherent in manufacturing processes, lattices are prone to defects such as missing or malformed struts. This concern is further compounded by the fact that the fracture toughness (K_{ic}) of cellular materials, including foams and lattices, is expressed as [45]:

$$K_{ic} = C\sigma_f\sqrt{\pi L}\bar{\rho}^{3/2} \tag{5.1}$$

where ($\bar{\rho}$) is the relative density, (L) is the cell size, σ_f is the fracture strength of the material, and C is a fitting constant. This shows that fracture toughness is expected to drop with relative density and cell size, meaning both nanolattices as well as lightweight lattices are expected to be fracture-prone as compared to their denser, macroscale counterparts, presenting a significant challenge. However, given the broad structural tunability, lattices offer the potential to architect new 'toughening mechanisms', much like is shown in the earlier parts of this dissertation.

Recent work on interpenetrating lattices explores toughening behavior in lattices composed of multiple 3D connected lattices, woven through the voids of each other, creating an effective multi-body material [136]. It was shown that as damage progresses unequally

through the two lattices, they make contact, re-distributing loads and dissipating energy via crack bridging, friction, and distributed fracture. Elastic anisotropy between the two sub-lattices results in two separate cracks of differing lengths in the two distinct sub-lattices, but load sharing is induced through contact, causing the development of an effective bridging zone that forces the two sub-lattice cracks to grow simultaneously and stably. What is remarkable is that this significant toughening is achieved via a single material and even though the lattices were made out of brittle constituents, they demonstrated a considerably enlarged fracture process zone and increased fracture energy. Notably, this toughening did not occur when similar lattices were combined. While some work has argued that ductile interpenetrating lattices are unlikely to be tougher [125], there was a fundamental missing insight that dissimilar lattices have different anisotropic FPZs that affect their resulting toughness. This work explores how anisotropic FPZs interact to create larger process zones and enhance the extrinsic size-affected toughening.

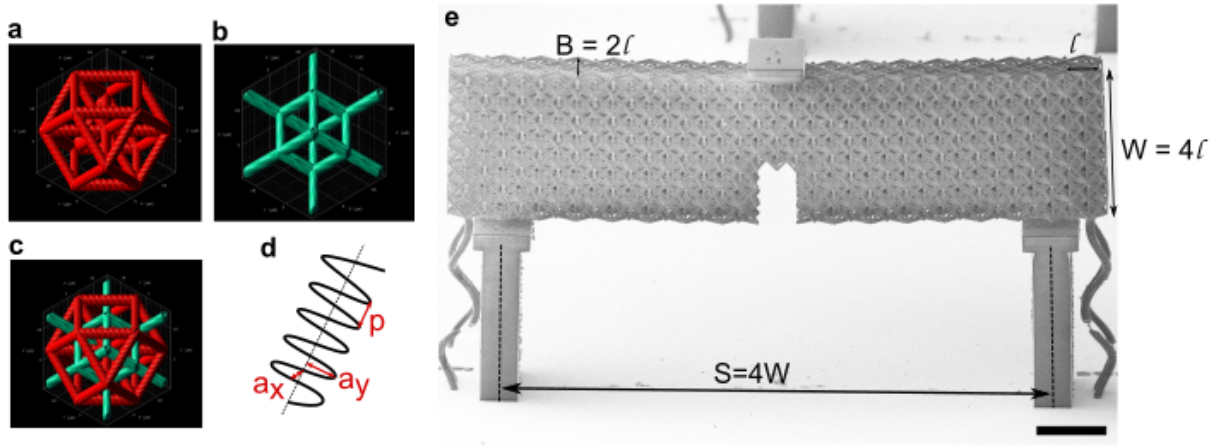

Figure 5.1: **Design of μSENB Interpenetrating Lattices Beams.** (a,b,c) Describe rendering of the OC, RD and (OC+RD) IPLs. (d) Helical write path for creating uniform lattice struts showing the x and y radii of the helix *ax* and *ay* respectively and the pitch *(p)*. (e) Final μSENB of the IPL beam showing the geometrical dimensions (Scale bar: 20μm).

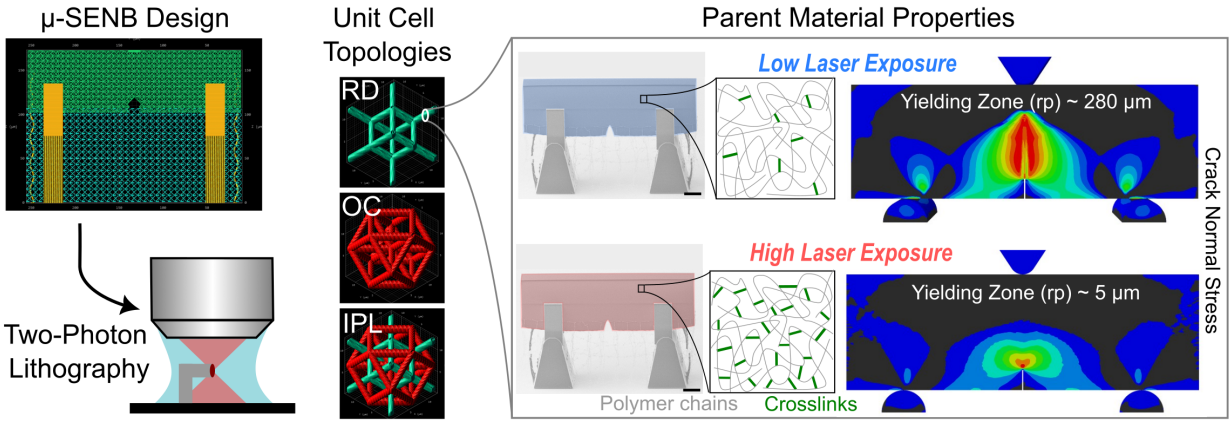

Figure 5.2: **Controlling Mechanical Behavior of Interpenetrating lattice beams** (a,b,c) Describe rendering of the OC, RD and (OC+RD) IPLs. (d) Helical write path for creating uniform lattice struts showing the x and y radii of the helix *ax* and *ay* respectively and the pitch *(p)*. (e) Final μSENB of the IPL beam showing the geometrical dimensions (Scale bar: 20μm).

5.3 Design

To understand the fracture behavior of interpenetrating lattices, three specimen types were created: Rhombic Dodecahedron (RD) lattice, Octet (OC) or Face-centered cubic(FCC) lattice, and an (RD+OC) Interpenetrating Lattice (IPL) as seen in Figure 5.1a,b,c. To create beams with final relative density equal to 25%, strut dimensions in all three lattices were kept constant and the unit cell size *(l)* was varied instead. This is because previous work has shown that surface roughness causes a significant reduction in effective properties of additively manufactured features as the feature size decreases, making comparisons between different lattices with different strut diameters inherently convoluted [121].

To create free standing μSENB specimens, a support lattice is written below the test beam to avoid stacking errors, as proposed by Gross et al. [51]. However, if the test beam is also a lattice, it would mean that both the support lattice and test lattice would get etched,

destroying the test beam. To avoid this, a helical laser trajectory was used to create thicker beams with uniformly cross-linked cross section which would survive the etching process as also proposed by Gross et al. [51] (Figure 5.1d). Beams had 4 unit cells across the thickness $W=4l$ and 2 unit cells across the width $B=2l$. The span length (S) was kept equal to 4 times the width $S=4W$ as defined in [59] and seen in Figure 5.1e. Notches were designed to be one unit cell wide and 1.5 times the unit cell width in height. Separate loading pads were also printed at the bottom of the beam where the beam touches the three-point bend supports and on the top center of the beam where the indenter head comes in contact. This is done to prevent local indentation as recommended in ASTM C393 for sandwich beams [60].

To study how fracture behavior changes with the activation of size-effects, two sample types were created. The lowest laser power was used to create RD, OC, and IPL lattices in which the struts have DC = 17%, and these will be denoted as $\mathrm{RD_{duc}}$, $\mathrm{OC_{duc}}$, and $\mathrm{IPL_{duc}}$. One batch of the DC 17 samples was tested as is, and the other was heated in a vacuum furnace at 200∘C to create lattices in which the struts have DC = 80%, and these will be denoted as $\mathrm{RD_{bri}}$, $\mathrm{OC_{bri}}$, and $\mathrm{IPL_{bri}}$ as shown in Figure 5.2.

5.4 Fabrication

The entire three-point bend assembly and the nano-Bouligand beams are designed in Python and imported into Quantum-X Professional DLW system (Nanoscribe GmbH). Specimens were fabricated on silicon substrates, which were first etched for 5 minutes in oxygen plasma (Plasma Etch - 25 system) and then functionalized using 3-(Trimethoxysilyl) propyl methacrylate to improve adhesion and prevent peeling off of supports during fracture tests. Subsequent writes were done using two-photon lithography (TPL) direct laser writing (DLW) system (Nanoscribe, GmbH). A proprietary acrylate-based resist, IP-Dip (Nanoscribe, GmbH), was used with a 63x objective to obtain high-precision sub-micron resolution writes. A one-hour

hold time was used to enable refractive index matching of the IP-Dip resin with the 63x objective. Printed structures were immersed in a propylene glycol monomethyl ether acetate (PGMEA) solution for 20 mins, then in ultrapure IPA for 30 mins followed by critical point drying (Autosamdri-931 system Tousimis). These were subsequently etched in a downstream oxygen plasma etcher (YES CV200 RFS downstream etcher) at 45°C with 65 W power, a pressure of 760 millitorr, and 100 SCCM O_2 flow [51].

5.5 Mechanical Testing

In-situ fracture tests were performed using the displacement-controlled mode in an Alemnis ASA nanoindentation system. Specimens were tested either to complete fracture, or to a displacement of 50-60 µm, and video data was captured for each test. Instantaneous load line stiffness was calculated using the unloading slope of the CSM data, and crack initiation was determined as the point where the unloading stiffness began to decrease. Crack lengths were obtained using a compliance calibration procedure [55] by correlating the crack initiation point with the instantaneous stiffnesses thereafter. The tool was installed in a Thermo-Fisher Scientific Apreo SEM, and testing was done with a 2 µm radius conductive diamond wedge tip. A loading rate of 60 nm/sec, a sinusoidal signal of amplitude 60 nm and frequency 6 Hz were superimposed to perform continuous stiffness measurement (CSM) and thereafter compute instantaneous crack lengths. All test videos were recorded using a 300 ns refresh time and 2-frame integration.

Load measured during nanomechanical testing always contains some thermal drift, which increases with time. To account for this, we kept the nanoindenter assembly installed for a time greater than 12 hours prior to testing for the drift to stabilize. We additionally added 'out-of-contact' segments before and after the compression step where the tip is not in contact with the sample to correct for any drift in the system. Thermal drift showed linear

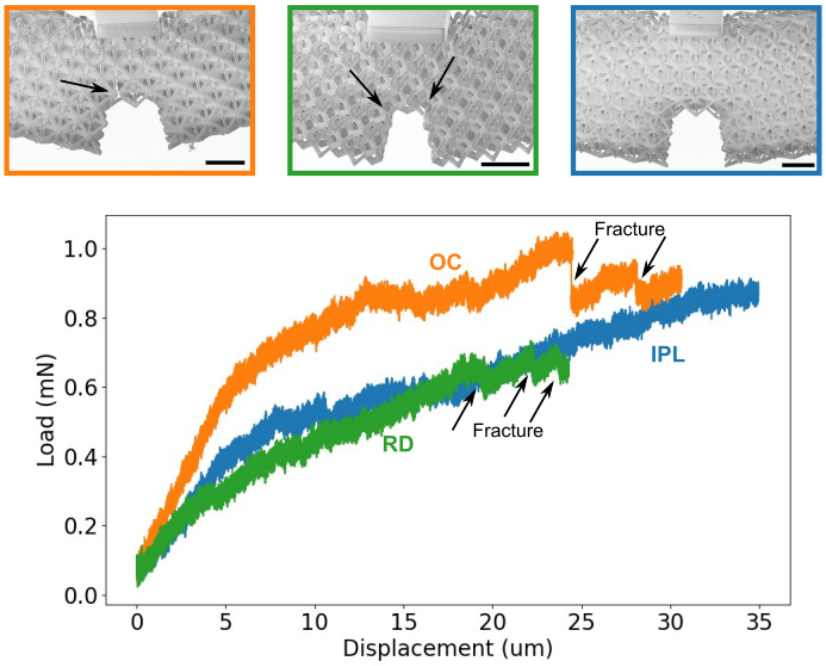

Figure 5.3: **Post fracture crack fronts and μSENB test data.** (Top) Left to right OC, RD and IPL beams respectively. Damage initiates in both the OC and RD beams, as seen by the broken struts. No damage is observed in the IPL beam (right). (Bottom) Load vs displacement data during fracture test in OC, RD and IPL lattices. Both OC and RD show load drops corresponding to strut failure, but the load in the IPL continues to increase.

correlation with time for short experiment times (less than 30 minutes) and was subsequently subtracted from the load data during data processing. Despite these efforts, CSM data can be noisy, and since that can significantly affect the computation of crack lengths and J-curves, an amplitude based Fast Fourier Transform (FFT) noise filtering algorithm was applied on the load-displacement data. Subsequent CSM Data was smoothed using the Savitzky-Golay filter by fitting a third order polynomial for every 300-400 data points.

5.6 Brittle Lattices

μSENB fracture tests were conducted on the OC, RD and IPL samples on the piezo-driven in-situ nanoindentation system (ASA, Alemnis AG) using the same procedure as described in Chapter 2. Although the goal was to test each specimen to fracture, due to technical challenges, all beams could only be tested to part of the failure displacement as visible in Figure 5.3.

Despite that, we observed interesting differences in the fracture behaviour of different samples. Figure 5.3 shows the post fracture crack fronts in the three lattices as well as the load-displacement response during fracture. Similar to White et al. in [135], we observe that the OC lattice has the highest stiffness and the RD lattice has the lowest stiffness with the (OC+RD) IPL showing an intermediate stiffness between the two. In terms of fracture, we see that with increasing displacement damage initiates in both the OC and RD lattices, resulting in fracture of individual struts near the crack tip. This happens at a displacement of ∼18μm in the RD beams and ∼24μm in the OC beam. In contrast, we do not see any damage initiate in the IPL beam and the load continues to increase.

5.7 Ductile Lattices

Preliminary experiments on lattices with DC=17% revealed enhanced strain to failure as compared to the lattices made of brittle constituents. This was true even for the single RD

and OC lattices, although the most significant impact was on the IPL lattices. Even at very high strains, IPL beam did not show any crack propagation, but simply continued to deflect under the applied load. This is shown in Figure 5.4

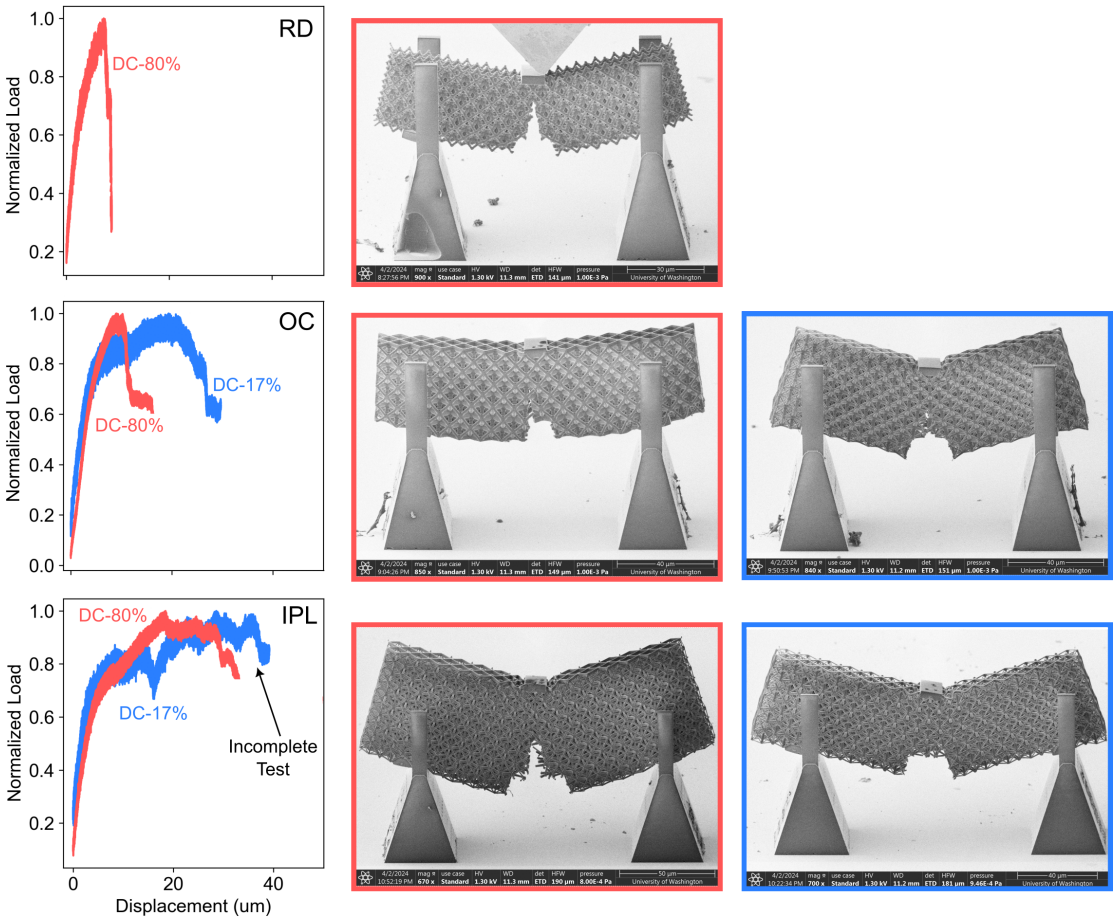

Figure 5.4: Comparing Fracture in Brittle and Ductile Architected Lattices

Chapter 6

SUMMARY AND OUTLOOK

6.1 Summary

This dissertation demonstrates the creation of fracture-resistant nanoarchitected materials that acquire their enhanced properties through a combination of small-scale fracture size effects and architectural toughening mechanisms. More broadly, we show that toughness at the nano/microscale is not an "intrinsic" material property, but one that can be affected by molecular or nanoscale heterogeneity in a unique and controllable way. This is primarily accomplished through a combination of nanofabrication methods like two-photon lithography and oxygen plasma etching that enable the creation of free-standing polymeric nanostructures and in-situ nanomechanical testing that allows visual and physical insight into how different structures break.

By isolating and changing the orientation of materials comprised of twisted polymeric nanofibers, we show that toughness is significantly improved by the activation of size-enhanced plastic energy dissipation and nanoscale heterogeneity. We further show that nanostructure in materials can be generated explicitly using fiber architecture or indirectly via spatial property gradients, and both of these can drastically alter toughening behaviors.

An important step was to systematically investigate the mechanistic origins of the size-enhanced ductility demonstrated by the polymeric nanofibers in the framework of a size-effect study. Through small-scale experiments and numerical modeling on polymeric beams of varying degrees of crosslinking, we found that ductile to brittle transitions can be explained via a fracture size effect framework where fracture behavior is governed by the size

of the fracture yielding zone with respect to the size of the structure. This work provided a crucial insight that ductility is a size-induced property that occurs when features are reduced below a characteristic fracture length scale and that strength, stiffness, and toughness alone are insufficient predictors of ductility. Understanding characteristic fracture lengths is thus crucial for designing any component where mechanical performance is a priority.

We then used this insight to demonstrate how the incorporation of size effects in the design of architected materials can fundamentally alter toughness. By creating μ-layered polymeric beams where layer thickness was controlled to be smaller than the size of the constituent material's fracture-yielding zone, we show that a combination of size-enhanced ductility and architectural heterogeneity amplify toughness significantly more than what is possible by their non-size-affected counterparts.

Lastly, we explore the world of interpenetrating lattices, comprising two separate lattice structures woven through the voids of another. Similar to the layered structures, these lattices are constructed with feature sizes that can activate and deactivate size-affected ductility. But the key idea here is to understand how architectural hierarchy, achieved by combining different preferred paths for crack propagation in both of the sub-lattices, amplifies toughness. We show that ductile nano-interpenetrating lattices significantly resist crack initiation and propagation as compared to both separate lattices and nano-interpenetrating lattices with brittle constituents, underscoring the role of feature size in fundamentally utilizing size effects to create architected materials with unprecedented properties.

6.2 Outlook

I believe the work in this dissertation enables the ability to make any material tough by utilizing the fundamental principles that govern intrinsic (material) and extrinsic (architectural) fracture size-effects.

This has direct implications for the printing of any additively manufactured material, particularly materials that are lightweight and made using a TPL process. There are inherent gradients in all materials, but additive manufacturing enables the intentional introduction of gradients based on print paths and layer thicknesses. It is now apparent that any internal stiffness gradient in a material can be beneficial for crack growth resistance and should be carefully considered in part design. While it is challenging to create high-density nanofibrous materials using the TPL process here due to proximity effects, other fabrication methods that allow for the creation of dense, separated nanofibers could also have marked improvements in toughness.For instance, tougher engineering composites can be created by controlling the fiber spacing or fiber diameter in a reinforced composite.

This work has long-term applications in sustainable materials development, wherein earth-abundant materials that are thought to be intrinsically brittle, like silica, can be made ductile and used in tough composites, much like what is found in natural materials. Processing or compositional changes such as heating, filler addition, or grain size modification inevitably alter process zone sizes and can drastically alter fracture behaviors. By characterizing fracture size effects, ductile to brittle transitions can be accounted for in such materials, and feature sizes in components can be controlled to prevent catastrophic failure. In the context of additively manufactured materials, there is a new potential to design feature sizes to match constituent characteristic length scales and maximize toughness while maintaining strength and stiffness. Moreover, the strength and stiffness of a structure can be controlled by altering the material composition, while the fracture behavior can be modified by adjusting the feature sizes within the architecture. There is, therefore, an enormous potential for fundamentally re-investigating the origins of fracture toughness and cascading multiple damage mechanisms in hierarchical architectures to develop highly tough and damage-tolerant materials with properties approaching that seen in natural structural materials.

Appendix A

QUANTIFYING TOUGHENING DUE TO NANO-HETEROGENEITY

To directly quantify the increase in material toughness caused by stiffness variation, the inhomogeneity-based fracture energy equation can be further reduced as follows:

$$J_{tip} = J_{far} + C_{inh} = J_{far}(1 + F_{inh}) \tag{A.1}$$

where F_{inh} only depends on the stiffness and thickness of different materials in the stack. F_{inh} can be further expressed as:

$$\mathrm{F_{inh}} = \mathrm{p_o} \int_0^{\mathrm{T}} \left(\frac{\mathrm{E_o}}{\mathrm{E(a+\varepsilon)}} - \frac{\mathrm{E_o}}{\mathrm{E(a-\varepsilon)}}\right)\frac{1}{\pi\varepsilon}\,\mathrm{d}\varepsilon \; - \mathrm{p_o'}\left(\frac{\mathrm{E_o}}{\mathrm{E(a)}} - \frac{1}{\mathrm{T}}\int_0^{\mathrm{T}} \frac{\mathrm{E_o}}{\mathrm{E(x)}}\,\mathrm{dx}\right) \tag{A.2}$$

Here T is the total stack thickness, a is the crack length, z is the coordinate perpendicular to the crack front propagation, ε is the relative coordinate ahead of the crack tip (ε = z - a), E(z) is the elastic modulus oscillation, and po and po' are defined as po = 3-4v/(4-4v) and po' = 1-2v/(2-2v) for plane strain [43].

The computation of F_{inh} thus requires a modulus function that describes how the stiffness changes through the thickness of the material. Previous studies have used a 1D sinusoidal function ($E(z)$) [43, 133]. In the nano-Bouligand materials studied here, these stiffness gradients exist at the voxel level, meaning the constituent fiber has a stiff core and soft edge. The combination of these fibers creates 3D stiffness gradients ($E(x, y, z)$) that require additional consideration to incorporate into a toughening model properly. To demonstrate the com-

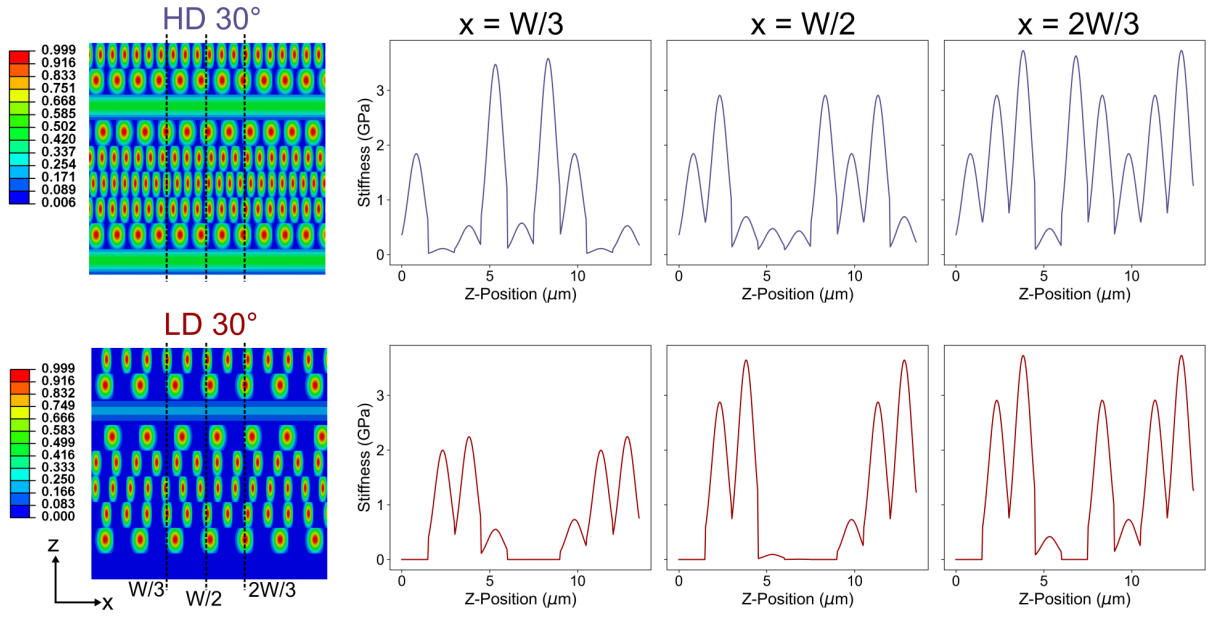

Figure A.1: **Variation in Stiffness Gradients** Cross-sections in HD-30° and LD-30° nano-Bouligand beams demonstrating the variation in stiffness. Line plots show variation in stiffness at a particular line taken along the beam width, demonstrating the complex variation of stiffness through the material.

plexity of the stiffness inhomogeneity, we modeled the stiffness variation in a voxel in both x (along beam width) and z (along beam height) directions as a gaussian function and generated corresponding stiffness gradient maps and stiffness line plots at different x-positions. These demonstrate that pre-existing F_{inh} and F_{inh} quantification methodologies using sinusoidal stiffness variation cannot truly capture the toughening due to the inhomogeneity in these materials. It should be noted that most existing analyses only exist for linear elastic materials.

In the nano-Bouligand materials here, the center of the nanofiber – i.e. the middle of the line write path – is the stiffest part of the material ($E = E_{max}$), the midpoint between nanofibers is the most compliant ($E = E_{min}$), and the void regions around the fibers have zero stiffness ($E = 0$). These spatial gradients in stiffness create a complex network of crack shielding and anti-shielding regions that become more inhomogeneous with increasing twist angles. In the HD nano-Bouligand beams, this inhomogeneity has an aggregate crack shielding effect ($C_{inh} < 0$) and leads to a delayed crack initiation, thereby causing both a higher initiation toughness and a higher J_{1L} with increasing twist angles (Figure 2.6). In the MD and LD beams, there is an even greater gradient between the layers, which should also create a crack shielding effect, but the high porosity significantly reduces the material activated during fracture and enables the crack to easily propagate along the zero-resistance void regions ($C_{inh} > 0$), resulting in a lower J_{1L}. It should be noted that all the materials in this study have a 3D spatial variation in stiffness (Figure A.1), meaning this J_{tip} analysis is overly simplified but provides a useful qualitative description of the observed phenomenon.

The authors have applied the above framework in Equation (A.2) using the stiffness line profiles in Figure A.1 to quantify and compare the toughening between some of the nano-Bouligand beams in this study. We obtained J_{tip}/J_{far} values for HD-0°, 5°, and 30° beams and show them in Figure A.2. A J_{tip}/J_{far} value less than 1 indicates material toughening,

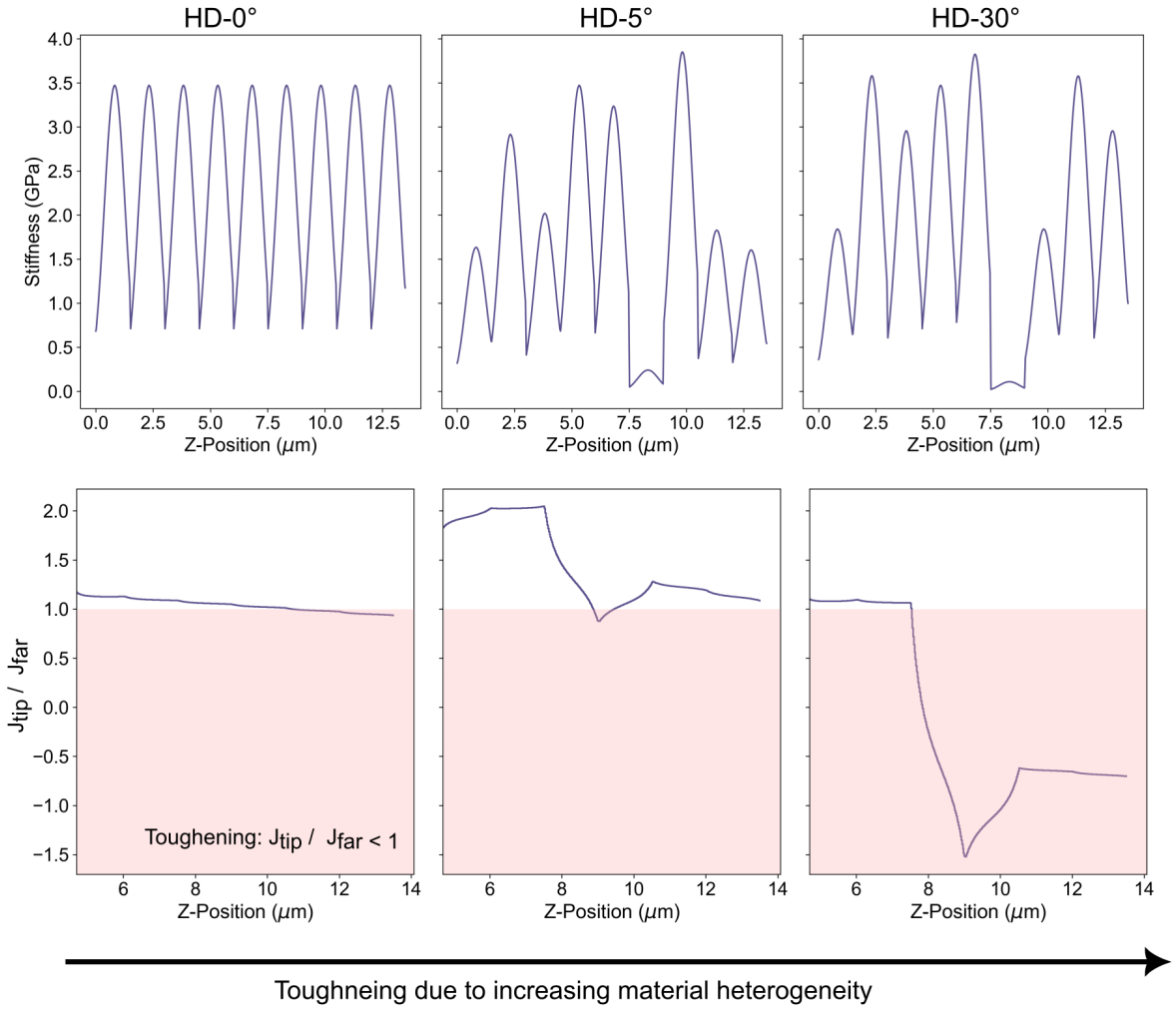

Figure A.2: (Top) Stiffness variation as a function of z-position (along beam height) for HD-0°, 5°, and 30° nano-Bouligand beams. (Bottom) Corresponding J_{tip}/J_{far} vs z-position showing increasing toughening with twist angle due to decreasing value of F_{inh}.

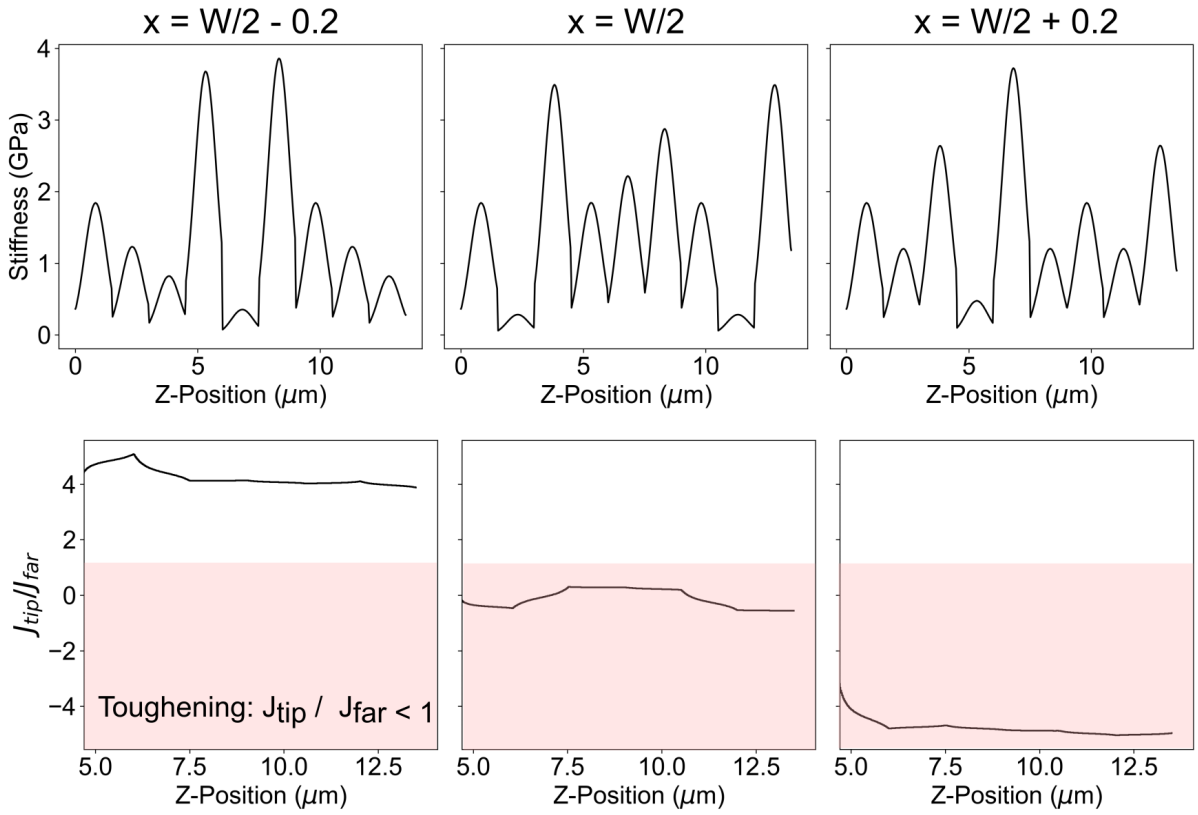

Figure A.3: (Top) Stiffness variation as a function of z-position (along beam height) for HD 30° nano-Bouligand beams. ±200 nm are chosen to demonstrate variation across the width of a voxel. (Bottom) Corresponding J_{tip}/J_{far} vs z-position showing high variability depending on what stiffness z-position is chosen.

with increasing toughness as F_{inh} decreases. It can be seen that the HD-0° beams have little to no toughening due to the heterogeneity, while the HD-30° have a pronounced toughening from the architecture. It should be noted that this analysis only represents F_{inh} for a single-line variation in stiffness. As seen in Figure A.3, for the same nano-Bouligand beam, we can get very different J_{tip}/J_{far} values depending on the z-position of the E profile. To fully understand the effect of inhomogeneity, a 3D theoretical framework, and numerical modeling are required.

Appendix B

NANOBOULIGAND RELATIVE DENSITY

Relative density calculations were made using CAD renderings of the material. Modeled voxel dimensions were measured from SEM images and bridging zones were incorporated to account for the additional cross-linking at layer intersections that occur due to proximity effects. The center-to-center distance between layers (l) is set equal to 1500 nm in all beams, creating a minimum overlap (δ) equal to 150 nm between two layers. The high laser exposure during fabrication results in the voxel having a slightly hyperbolic (peanut-shaped) cross-section rather than an elliptical one. Figure B.1 shows the fiber shape as well as the shape of the intersection region between fibers. Given the voxel size uncertainty and variation in bridging zone size, it is estimated that the calculated relative densities (Table B.1) have a variance of $\pm 5\%$, and introducing a twist causes less than 0.8% variation in the relative density.

	Measured Volume	Excess Plate	Corrected Fiber Volume	Beam Volume	Bridging region	Density
LD-0	64.68	5.2	59.48	124	130 nm	0.47967742
LD-30	63.63	5.2	58.43	124	130 nm	0.47120968
MD-0	86.79	8	78.79	124	200 nm	0.63540323
MD-30	86.4	8	78.4	124	200 nm	0.63225806
HD-0	110.23	10	100.23	124	250 nm	0.80830645
HD-30	109.86	10	99.86	124	250 nm	0.80532258

Table B.1: Relative Density Measurements from Solidworks

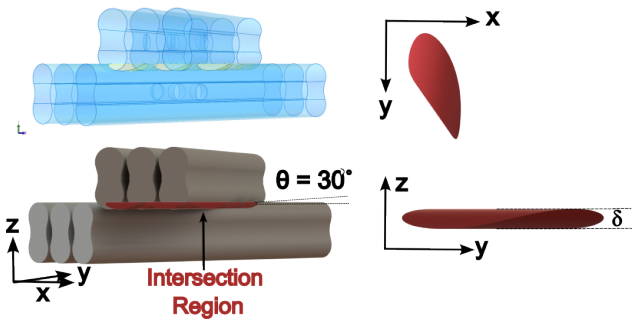

Figure B.1: **Intersection volume between fibers in a $\theta = 30^\circ$ nano-Bouligand beam.**

Appendix C

NANOMECHANICAL FRACTURE DATA ANALYSIS

The load-displacement and CSM data obtained from in-situ fracture tests were post-processed for thermal drift, noise, and testing instabilities to get a smooth and continuous J-R curve. First, the total drift during the test was calculated by using the initial and final out-of-contact segment and considering a linear drift function (The linear drift was verified by doing a 24 hr long in-situ hold experiment). This drift was then subtracted from the data. The initial knee and the final out-of-contact segment were subtracted. The data is then smoothened using an Fast-Fourier transform amplitude based filter as well as other data smoothing filters like Savitzky–Golay. The unloading segments of the CSM loading are then identified from the smoothened data to calculate unloading stiffness. At this point the Load-displacement data is reduced to peak to peak load-displacement data for ease of analysis. Instantaneous crack lengths are then calculated using Haggag's formulation[55]. J-integrals are then calculated based on ASTM-E1820 [41]. Finally, in-situ videos are trimmed and synced to the Load-displacement data.

```
1
2
3 #### Import Libraries
4 import numpy as np
5 from math import *
6 import matplotlib as mpl
7 import matplotlib.pyplot as plt
8 from scipy.signal import savgol_filter
```

```
from scipy.stats import linregress
from sympy import symbols, Eq, solve
from scipy.fft import fft, ifft, fftfreq, rfft
# import cv2
# import imageio
from scipy.stats import linregress

### Functions for Data Analysis
def Trim_data(Load_array, Disp_array, Time_array, condition1_load,
    condition2_disp, maxdisplacement = False):
    if max(Load_array)<0.3:
        C1=Load_array>0.11
    else:
        C1 = Load_array>condition1_load
    # if maxdisplacement:
    #     C2 = Disp_array==max(Disp_array)
    # else:
    #     C2 = np.around(Disp_array-condition2_disp, decimals = 1)==0


    if maxdisplacement:
        C2 = Disp_array==max(Disp_array)
    else:
        if condition2_disp<max(Disp_array):
            C2 = np.around(Disp_array-condition2_disp, decimals = 1)==0
        else:
            C2 = Disp_array==max(Disp_array)


    for i,a in enumerate(C1):
```

```
38          if a:
39              trim = i
40              break
41      for i,a in enumerate(C2):
42          if a:
43              trim_end = i
44              break
45      Newload_array = Load_array[trim:trim_end]
46      Tempdisp_array = Disp_array[trim:trim_end]
47      Temptime_array = Time_array[trim:trim_end]
48      Newdisp_array = Tempdisp_array-min(Tempdisp_array)
49      Newtime_array = Temptime_array-min(Temptime_array)
50
51      return(np.array(Newload_array), np.array(Newdisp_array), np.array(
        Newtime_array))
52
53  def Drift_correction(Time_array,Load_array, initial_points, final_points):
54      Point1 = [Time_array[initial_points], np.average(Load_array[0:
        initial_points])]
55      Point2 = [Time_array[final_points], np.average(Load_array[final_points
        :])]
56      slope = (Point2[1]-Point1[1])/(Point2[0]-Point1[0])
57      intercept = (Point2[0]*Point1[1]-Point1[0]*Point2[1])/(Point2[0]-
        Point1[0])
58      Drift = [slope*t+intercept for t in Time_array]
59      Corrected_Load = [L-D for L,D in zip(Load_array, Drift)]
60      return(np.array(Corrected_Load), Drift, [Point1, Point2])
61
62  def FFT(Load_array, Disp_array, Time_array, cutoff, amplitude=True,
        Plot_FFT= False, trimstart = 100, trimend = -150):
```

```
63      t = Time_array
64      x1 = Disp_array
65      x2 = Load_array
66      sampling_rate = int(len(t)/(t[-1]-t[0]))
67      N = (t[1]-t[0])*len(t)*sampling_rate
68      #Calculate FFTs
69      y1 = fft(x1) #Disp FFT
70      y2 = fft(x2) #Load FFT
71      xf = fftfreq(int(np.ceil(N)),1/sampling_rate)
72      PSD1 = [np.abs(i) for i in y1] #Power spectrum density for Disp
73      PSD2 = [np.abs(i)  for i in y2] #Power spectrum density for Load
74      if Plot_FFT:
75          plt.close('all')
76          plt.rc('xtick',labelsize=20)
77          plt.rc('ytick',labelsize=20)
78          fig, (ax21, ax22)= plt.subplots(1,2,figsize=(14,9), dpi=128)
79          ax21.plot(2*np.pi*xf[:len(PSD1)], PSD1, '.--')
80          ax22.plot(2*np.pi*xf[:len(PSD2)], PSD2, '.--')
81          ax21.set_xlabel('Frequency (Hz)')
82          ax21.set_ylabel('FFT Displacement')
83          ax22.set_xlabel('Frequency (Hz)')
84          ax22.set_ylabel('FFT Load')
85      indices =[]
86      PSD2clean=[]
87      y2clean=[]
88      if amplitude:
89          for i in range(len(PSD2)):
90              if PSD2[i].real>cutoff:  #Get this value y=data cutoff,
    usually between 15-30
91                  indices.append(1)
```

```
92              else:
93                  indices.append(0)
94          for i in range(len(indices)):
95              PSD2clean.append(PSD2[i]*indices[i])   #Use this to check how
    FFT looks after filtering
96              y2clean.append(y2[i]*indices[i])
97          ffilt_load = np.abs(np.fft.ifft(y2clean))  #Final Cleaned Load
    Data from inverse FFT
98      else:
99          for i in range(len(PSD2)):
100             if -cutoff<xf[i]<cutoff:   #8 Get this value y=data cutoff
101                 indices.append(1)
102             else:
103                 indices.append(0)
104         for i in range(len(indices)):
105             PSD2clean.append(PSD2[i]*indices[i])   #Use this to check how
    FFT looks after filtering
106             y2clean.append(y2[i]*indices[i])
107         ffilt_load = np.abs(np.fft.ifft(y2clean))
108     ###returning filtered load, old displacement and time - trimmed on
    both ends
109     return (ffilt_load[trimstart:trimend], x1[trimstart:trimend], t[
    trimstart:trimend])
110
111 def UnloaD_SegmentS(Load_array, Disp_array, Time_array,c):
112     L = Load_array
113     D = Disp_array
114     T = Time_array
115     a = b = 1
116     LD = len(D)-c
```

```
117     UL = []
118     while a and b:
119         a = next((i for i in range(b,LD) if all(L[i]>=x for x in L[i:i+c])
        and  all(D[i]>=x for x in D[i:i+c])),False)  #all(L[i]>=x for x in L[i
        :i+c]) and
120         b = next((i for i in range(a,LD) if all(L[i]<=x for x in L[i:i+c])
        and  all(D[i]<=x for x in D[i:i+c])),False)  #all(L[i]<=x for x in L[i
        :i+c]) and
121         if a and b and b>a+c: UL += [[a,b]]  #;  L_mod += list(L[a:b]) ;
        D_mod += list(D[a:b]); T_mod += list(T[a:b])
122     # D_mod_temp = [D[UL[i][0]:UL[i][1]] for i in range(len(UL))]
123     # L_mod_temp = [L[UL[i][0]:UL[i][1]] for i in range(len(UL))]
124     # T_mod_temp = [T[UL[i][0]:UL[i][1]] for i in range(len(UL))]
125     # D_unload = [j for x in D_mod_temp for j in list(x)]
126     # L_unload = [j for x in L_mod_temp for j in list(x)]
127     # T_unload = [j for x in T_mod_temp for j in list(x)]
128     L_val =[]; D_val =[]; T_val =[]
129     for a,b in UL:
130         L_val += [L[a]]; D_val += [D[a]]; T_val += [T[a]]
131     return(np.array(L_val), np.array(D_val), np.array(T_val), UL)  #np.
        array(L_unload), np.array(D_unload), np.array(T_unload),
132
133 def Unload_Slope(Load_array, Disp_array, Time_array,Unloading_Segments,
        window_length =7, polyorder=3):#window_length=41
134     L = Load_array
135     D = Disp_array
136     T = Time_array
137     UL = Unloading_Segments
138     #Find Modulus
139     CSM = []; R2 = []; CSM_final =[]
```

```
140     for a,b in UL:
141         fit = linregress(D[a+1:b-1],L[a+1:b-1]) #contains slope, intercept
        , rvalue, pvalue, stderr
142         CSM += [fit.slope]; R2 += [fit.rvalue**2]
143     for eta,i in enumerate(CSM):
144         if i<0:
145             CSM[eta] = 0
146     return (savgol_filter(CSM, window_length,polyorder), CSM)
147 
148 def Modulus(Load_array, Disp_array, Span, Width, Thickness,a,b):
149     Stress_i = ((3*Span)/(2*Width*Thickness*Thickness))*Load_array
150     Strain_i = (6*Thickness/(Span**2))*Disp_array
151     Strain = Strain_i-min(Strain_i)
152     Stress = Stress_i-min(Stress_i)
153     fit = linregress(Strain[a:b],Stress[a:b])
154     mod = fit.slope; C=fit.intercept
155     Y = [0, max(Stress)] #Stress[a]
156     X = [(y-C)/mod for y in Y]
157     return (mod, C,X,Y, Stress, Strain)
158 
159 def DynamicModulus(Load_array, Disp_array, a, b):
160     fit = linregress(Disp_array[a:b],Load_array[a:b])
161     mod = fit.slope; C=fit.intercept
162     # Y = [0, max(Stress)] #Stress[a]
163     # X = [(y-C)/mod for y in Y]
164     return (mod, C)
165 
166 def Plot_slope_fit(Stress,Strain,modulus, X,Y,point1, point2, File_name):
167     plt.plot(Strain[:int(2*len(Strain)/3)],Stress[:int(2*len(Strain)/3)],'
        .--', label = File_name+'raw')
```

```
168     plt.plot(Strain[point1],Stress[point1], 'o')
169     plt.plot(Strain[point2],Stress[point2], 'o')
170     plt.plot(X,Y,'.--', label = str(File_name)+'mod='+str(modulus))
171     plt.legend()
172 
173 def faW(a_faw,W_faw):
174     k = a_faw/W_faw
175     f_aW = 3*np.sqrt(abs(k))*(1.99-k-k*(2.15-3.39*k+2.7*k**3))/(2*(1+2*k)
    *(1-k)**(3/2))
176     return(f_aW)
177 
178 def U_var(s_var,F_value):
179     uvalue = 1/(1+np.sqrt(F_value/s_var))
180     return (uvalue)
181 
182 def a_Compliance_Calibration(CSM_slopes_array, ao,W,test_zero, Smooth,
    window_length =21, polyorder=3): ##41
183     Co= 1/max(CSM_slopes_array)                                    # Minimum
    Compliance (Compliance at crack initiation), KPa -1
184     cii = list(CSM_slopes_array).index(max(list(CSM_slopes_array)))
      #crack initiation index
185     Ux = symbols('Ux')
186     Equation_1 = solve(0.997 - 3.58*Ux  -1.51*Ux**2 -110.00*Ux**3 +
    1231.00*Ux**4  - 4400.00*Ux**5- ao*e**-6/(W*e**-6) ,Ux,dict=True)
187     Uxi2 = float(Equation_1[0][Ux])
188     F_val = (1/Co)*(1/Uxi2-1)**2
189     ### Now we use the calibrated parameters to calculate crack lengths
    using CSM stiffness
190     a_initialize = [ao]*cii
```

```
191     a_growth = [(0.997 - 3.58*U_var(s,F_val)  -1.51*U_var(s,F_val)**2
    -110*U_var(s,F_val)**3  + 1231*U_var(s,F_val)**4 - 4400*U_var(s,F_val)
    **5)*W for s in CSM_slopes_array[cii:]]
192     a_total = np.array(a_initialize + a_growth)
193     if test_zero:
194         ###Make sure solver is finding the closest zero
195         test = (0.997 - 3.58*Uxi2  -1.51*Uxi2**2 -110.00*Uxi2**3 +
    1231.00*Uxi2**4  - 4400.00*Uxi2**5)*W
196         print('Given crack length:',ao, ' and Equation solution is:' ,
    test)
197     print(len(a_total))
198     if Smooth:
199         a_total[np.isnan(a_total)] = 0
200         a_total = savgol_filter(a_total, window_length, polyorder)
201     return (a_total)
202
203 def a_increase(crack_lengths):
204     for neta,i in enumerate(crack_lengths[:-1]):
205         if i>crack_lengths[neta+1]:
206             crack_lengths[neta+1]=i
207     return(np.array(crack_lengths))
208
209 def J_integral(Load_array, Disp_array, Time_array, CSM_slopes_array,
    CSM_unload_array,crackinitiationindex, PeaktoPeak_Load,crack_lengths,
    ao,W,B,S,nu,E):
210     L=Load_array; D=Disp_array; T=Time_array
211     cii = crackinitiationindex# list(CSM_slopes_array).index(max(list(
    CSM_slopes_array)))     #crack initiation index
212     J_values = []
213     Jval=0
```

```
214     neta = 1.9  #empirical constant
215     gamma = 0.9 #empirical constant
216     Jp = 0      #Initiation value
217     K_prefactor = (1-nu**2)/E
218
219     ### This loop calculates elastic J value
220     K_ivalue = np.array([P_l*S*faW(a_faw,W)/(B*W**(3/2)) for P_l,a_faw in
    zip(PeaktoPeak_Load,crack_lengths )])
221
222     ### Calculating Incremental Plastic Area  #Units:mN*um
223     # Delta_Area = [((L[CSM_unload_array[index+1][0]]+L[p])*(D[
    CSM_unload_array[index+1][0]] - L[CSM_unload_array[index+1][0]]*
    CSM_slopes_array[[index+1][0]]-D[p]+L[p]*CSM_slopes_array[index]))/2
    for index,[p,q] in enumerate(CSM_unload_array[:-1])]
224     Delta_Area = [((L[CSM_unload_array[index+1][0]]+L[p])*(D[
    CSM_unload_array[index+1][0]] - L[CSM_unload_array[index+1][0]]/
    CSM_slopes_array[[index+1][0]]-D[p]+L[p]/CSM_slopes_array[index]))/2
    for index,[p,q] in enumerate(CSM_unload_array[:-1])]
225
226     #[((L[PData[f]['aUL'][index+1][0]]+L[p])*(D[PData[f]['aUL'][index
    +1][0]] - L[PData[f]['aUL'][index+1][0]]*PData[f]['aCSM (kN/m)'][[index
    +1][0]]-D[p]+L[p]*PData[f]['aCSM (kN/m)'][index]))/2 for index,[p,q] in
     enumerate(PData[f]['aUL'][:-1])]
227
228     ### This loop calculates plastic J value
229     for i in range(len(Delta_Area)):
230         Jp = Jval
231         Jval = (Jp+(neta/(W-crack_lengths[i]))*(Delta_Area[i]/B))*(1-gamma
    *(crack_lengths[i+1]-crack_lengths[i])/(W-crack_lengths[i]))
232         J_values.append(Jval)
```

```
233         ##Jval units are KJ/m2
234
235     ###Adding elastic and plastic parts to calculate total J, multiplying
    by 1000 to get values in J /m2
236     J_integral =np.array(J_values)*10**3+ K_ivalue[1:]**2*K_prefactor #
    #*10**3
237     J_integral[np.isnan(J_integral)] = 0
238     return (savgol_filter(J_integral, 51, 3),K_ivalue, np.array(Delta_Area
    ), J_integral)
239
240 def add(*A):
241     '''Return sum of input vectors'''
242     return [sum(x) for x in zip(*A)]
243
244 def mult(a, b):
245     '''Return a constant 'a' multiplied into a vector'''
246     return [a*x for x in b]
247
248
249 def poInt(a1, v1, a2, v2):
250     '''Returns the point of intersection of two lines in 2D'''
251     if not v1[0]:
252         s = (a1[0] - a2[0])/v2[0]
253     else:
254         s = (a1[1]-a2[1]+(a2[0]-a1[0])*v1[1]/v1[0])/(v2[1]-v2[0]*v1[1]/v1
    [0])
255     return add(a2,mult(s,v2))
256
257 ##(180,255)
```

```
258 def CTOD(image, cgth, initial_crack_length, thresh=150, smooth=3,
    Normal_detect = True, Extra_detect = False):
259     #Convert Image to Grayscale
260     imgGrey = cv2.cvtColor(image,cv2.COLOR_BGR2GRAY)
261 
262     #Threshold the Image to Alter Contrast
263     _,imgThresh = cv2.threshold(imgGrey, thresh, 200, cv2.THRESH_BINARY) #
    255
264 
265     # #Smooth the Image by Eroding then Dilating
266     kernel = np.ones((5,5),np.uint8)
267     imgErode = cv2.erode(imgThresh,kernel,iterations = smooth)
268     smoothImage = cv2.dilate(imgErode,kernel,iterations = smooth)
269     # cv2.imshow('eroded', imgErode)
270     # cv2.imshow('dilated', smoothImage)
271 
272     bEdge = [len(smoothImage)-np.argmin(x[::-1]) for x in smoothImage.T]
273 
274     # # NewbEdge=bEdge
275     for eta,n in enumerate(bEdge):
276         if n-bEdge[eta-1]>20:
277             bEdge[eta] = bEdge[eta-1]
278 
279     # bEdge_values = Edgesmooth(NewbEdge, thresholdvalue=3,incrementvalue
    =0.35)
280     # bEdge = bEdge_values[0]
281 
282     #Find Crack Tip
283     iL = len(bEdge); i1 = int(iL/4); i2 = int(iL/2); i3 = int(3*iL/4)
284     itip1 = int(iL/3); itip2 = int(2*iL/3);
```

```
285     bTip = min(bEdge[itip1:itip2])
286
287     bTip_x =bEdge[itip1:itip2].index(bTip)+itip1
288     iTips = [i1+i for i,x in enumerate(bEdge[i1:i3]) if x == bTip]
289     iTip = int(sum(iTips)/len(iTips))
290
291     ##Find Corners
292     # C1 = bEdge[bEdge_values[1]] ; iC1 = bEdge_values[1]
293     # C2 = bEdge[bEdge_values[2]] ; iC2 = bEdge_values[2]
294     C1 = max(bEdge[:i2]); iC1 = bEdge.index(C1)  ##
295     C2 = max(bEdge[i2:iL]); iC2 = i2+bEdge[i2:iL].index(C2) ##
296     # print('Corner1: ', C1, ', Crack Tip: ', iTip, ' Corner2: ', C2)
297     corner1 = [iC1, C1]; corner2 = [iC2, C2]
298
299     #Fit Line to Top Edges
300     eFit1 = linregress(range(iC1),bEdge[:iC1])
301     eFit2 = linregress(range(iC2,iL),bEdge[iC2:])
302
303     #Fitting bottom edge to a curve to find crack length
304     xbottom = [x for x in range(len(bEdge))]
305     ybottom = [eFit1.intercept+x*eFit1.slope for x in range(int(0), int(iL
    /2))]+[eFit2.intercept+x*eFit2.slope for x in range(int(iL/2), int(iL))
    ]
306
307     fitparams = np.polyfit(xbottom[:len(ybottom)], ybottom, 2)
308     cbeambase = [fitparams[0]*np.square(i) + fitparams[1]*i + fitparams[2]
     for i in xbottom]
309     # cbeambase = savgol_filter(ybottom, 71,3)
310
311     ##Estimating Crack Length
```

```
312     # clth =cbeambase[i2]-bTip  ###this is the crack length
313     clth =max(cbeambase)-bTip
314     cgth.append(clth)
315 
316     # bpoint = [int(iL/2),cbeambase[xbottom.index(int(iL/2))]]
317     # bpoint = [i2, cbeambase[i2]]
318     bpoint =  [np.argmax(cbeambase), max(cbeambase)] ##[xbottom[np.argmax(
    cbeambase)], max(cbeambase)]
319     return [0,bTip,bTip_x,i2],[bEdge,smoothImage],[xbottom,cbeambase,clth,
    cgth, bpoint],[corner1,corner2]
320 
321 
322 def Plotting(Files_list, input_dictionary, X_data_key, Y_data_key,
    Y_data2_key,XLabelname, YLabelname,YLabelname2 ,Naming_list, twin =
    False,lineWidth=1, markerSize=4, markerScale = 4, LabelSize = 18,
    linepattern = '.--', linepattern2 = '^--'):
323     PlotData = input_dictionary
324     plt.close('all')
325     plt.rc('xtick',labelsize=LabelSize)
326     plt.rc('ytick',labelsize=LabelSize)
327     fig,(ax1) = plt.subplots(nrows=1,ncols=1,figsize=(14,9), dpi=128)
328     if twin:
329         fig.subplots_adjust(hspace=.5,wspace=0.4)
330         ax2 = ax1.twinx()
331     for eta,temp in enumerate(Files_list):
332         Plot1 = ax1.plot(PlotData[temp][X_data_key], PlotData[temp][
    Y_data_key], linepattern,markersize = markerSize, linewidth = lineWidth
    ,label=Naming_list[eta])
333         if twin:
```

```
334             Plot2 = ax2.plot(PlotData[temp][X_data_key], PlotData[temp][
    Y_data2_key], linepattern2,markersize = markerSize, linewidth =
    lineWidth, label=Naming_list[eta])
335     ax1.set_xlabel(XLabelname, fontsize=LabelSize)
336     ax1.set_ylabel(YLabelname, fontsize=LabelSize)
337     ax1.legend(title = Y_data_key, fontsize=LabelSize, markerscale =
    markerScale)
338     if twin:
339         ax2.set_ylabel(YLabelname2, fontsize=LabelSize)
340         ax2.legend(title = Y_data2_key, fontsize=LabelSize , markerscale =
     markerScale)
341     plt.tight_layout()
342
343 def adjust_lightness(color, amount=0.5):
344     import matplotlib.colors as mc
345     import colorsys
346     try:
347         c = mc.cnames[color]
348     except:
349         c = color
350     c = colorsys.rgb_to_hls(*mc.to_rgb(c))
351     return colorsys.hls_to_rgb(c[0], max(0, min(1, amount * c[1])), c[2])
352
353 def Video_Sync(Folder, Playback_speed, Displacement_array, Load_array,
    Time_array, Crack_lengths_array, J_values_array, Five_subplots=True):
354     folder = Folder  #r"C:\\Users\\zspat\\OneDrive - UW\\PhD Research\\
    Results\\Nanoindentation\\Polymer Bouligand Project\\210518
    _Sweep71_Test9\\Synced Videos\\"
355     dFolder = Folder #"LD_a_J_Videosync\\"  #data subfolder
356     vFolder = Folder #"LD_a_J_Videosync\\"  #video subfolder
```

```
357     lCrop =0.3##0.1 #left crop
358     rCrop = 0.7###0.9 #right crop
359     tCrop = 0.06###0.01 #top crop
360     bCrop = 0.875###0.975 #bottom crop
361     lCrop2 =0.1 #left crop
362     rCrop2 = 0.9 #right crop
363     tCrop2 = 0.01###0.01 #top crop
364     bCrop2 = 0.975###0.975 #bottom crop
365     show = False
366     speedMult = 1
367     speedx = Playback_speed #60
368
369     ## Find Files
370     dataFiles = [x for x in os.listdir(dFolder) if '.txt' in x]
371     VNames = [(g.replace('.txt',' degree')).replace('_', ' ') for g in
    dataFiles]
372
373     ##Denote Test Type
374     Type = {f:[] for f in dataFiles}
375
376     ## Process Data
377     for eta,dFile in enumerate(dataFiles):
378         ### removing stuff to create plot title
379         name_final = dFile.replace('.txt', ' deg')
380
381         ## Check Data
382         # Check Video Filepath
383         videoFile = vFolder+dFile[:-4]+'.mp4'
384         if not os.path.isfile(videoFile):
385             print('The video file ' + videoFile + ' cannot be found.')
```

```
386             continue
387
388         # Name The New Video
389         newFile = vFolder + dFile[:-4]+'_Synced_'+str(speedx)+'x' + '
    _Video.avi'
390         if os.path.isfile(newFile):
391             print(newFile+' already exists')
392             continue
393         else:
394             print('Writing ' + newFile.replace(folder,'') +
395                   ', file ' + str(dataFiles.index(dFile)+1) + ' of ' + str
    (len(dataFiles)))
396
397         Displacement = Displacement_array
398         Load = Load_array
399         Time = Time_array
400         Crack_lengths = Crack_lengths_array
401         J_values = J_values_array
402
403         ## Read Video
404         #See https://docs.opencv.org/2.4/modules/highgui/doc/
    reading_and_writing_images_and_video.html
405         aVideo = cv2.VideoCapture(videoFile)
406         scale = 1
407         # Video Metadata
408         vidWidth = aVideo.get(3)*scale
409         vidHeight = aVideo.get(4)*scale
410         vidFPS = aVideo.get(5)
411         vidnFrames = aVideo.get(7)
412
```

```
413         ## Set Video Parameters
414         #Get max displacement points
415         vidMaxDispFrame = vidnFrames #input('What frame had the max
    displacement?: ')
416         dataDispMaxIdx = Displacement.argmax()
417 
418         #Set Starting Frame
419         dataTimeDiff = (Time[-1]-Time[0])
420         startFrame = 0
421 
422         #Set runtime values
423         dataTime = (Time[-1]-Time[0])
424         nFrames = min(int(dataTime*vidFPS),int(vidnFrames-startFrame))
425 
426         ## Create Combined Video
427         #Set new video
428         CombinedVideo = imageio.get_writer(newFile, fps=vidFPS)
429 
430         #Open Alemnis video
431         aVideo = imageio.get_reader(videoFile, 'ffmpeg')
432 
433         if Five_subplots:
434             #Set up plot
435             if not show: plt.ioff()
436             fig1 = plt.figure(figsize=(27,12),gridspec_kw={'width_ratios'
    :[1,1.2,1,1,1]})#, constrained_layout=True)
437             fig1.suptitle(VNames[eta], fontsize = 18, fontweight = 'bold')
438             gs = fig1.add_gridspec(2,3)
439             ax1 = fig1.add_subplot(gs[0, 0])
440             ax2 = fig1.add_subplot(gs[:2,2])
```

```
441             ax3 = fig1.add_subplot(gs[1, 0])
442             ax4 = fig1.add_subplot(gs[0, 1])
443             ax5 = fig1.add_subplot(gs[1, 1])
444 
445             #Check time
446             sTime = time.time()
447 
448             #Start making video
449             for frame in range(startFrame,nFrames+startFrame,speedMult):
450                 # Clear the Axes
451                 ax1.cla()
452                 ax2.cla()
453                 # ax3.cla()
454 
455                 # Determine Time Position
456                 pos = (np.abs(Time/speedx-(frame-startFrame)/vidFPS)).
    argmin() #Find video time closest to Alemnis time
457 
458                 # Plot Data
459                 ax1.plot(Displacement, Load, '.-', color='0.75')
460                 ax1.plot(Displacement[0:pos], Load[0:pos], '.-', color ='#
    aa5500')
461                 ax1.plot(Displacement[pos], Load[pos], 'o', color='#000000
    ')
462                 ax1.grid(axis ='both', which = 'both', linestyle = '--',
    linewidth =1)
463                 ax1.set_ylim(bottom = 0.)
464                 ax1.set_xlim(left = 0.)
465 
466                 # ax3=ax1.twinx()
```

```
467                 ax3.plot(Displacement, Crack_lengths, '.-', color='0.75')
468                 ax3.plot(Displacement[0:pos],  Crack_lengths[0:pos], '.-',
     color='#aa0000')
469                 ax3.plot(Displacement[pos],  Crack_lengths[pos], 'o',
    color='#000000')
470                 ax3.grid(axis ='both', which = 'both', linestyle = '-.',
    linewidth =1)
471                 ax3.set_ylim(bottom = 0.)
472                 ax3.set_xlim(left = 0.)
473
474                 Displacementx = Displacement[1:]
475                 ax5.plot(Displacementx, J_values, '.-', color='0.75')
476                 ax5.plot(Displacementx[0:pos-1],  J_values[0:pos-1], '.-',
     color ='#005500')
477                 ax5.plot(Displacementx[pos-1],  J_values[pos-1],  'o',
    color='#000000')
478                 ax5.grid(axis ='both', which = 'both', linestyle = '-.',
    linewidth =1)
479                 ax5.set_ylim(bottom = 0.)
480                 ax5.set_xlim(left = 0.)
481
482                 # Write Axis Labels
483                 s=15
484                 ax1.set_xlabel('Alemnis Displacement $(\mu m)$',fontweight
    ='bold', fontsize=s)
485                 ax1.set_ylabel('Load (mN)',fontweight='bold', fontsize=s)
486                 ax3.set_xlabel('Alemnis Displacement $(\mu m)$',fontweight
    ='bold', fontsize=s)
487                 ax3.set_ylabel('Crack Extension, $\Delta$a $(\mu m)$',
    fontweight = 'bold', fontsize=s)
```

```
488                 ax5.set_xlabel('Alemnis Displacement $(\mu m)$',fontweight
    ='bold', fontsize=s)
489                 ax5.set_ylabel('J Integral $(J/m^2)$', fontweight = 'bold'
    , fontsize=s)
490 
491                 ## Plot Video Frame
492                 image = aVideo.get_data(frame)
493                 ax2.axis('off')
494                 ax2.imshow(image[int(vidHeight*tCrop):int(vidHeight*bCrop)
    ,int(vidWidth*lCrop):int(vidWidth*rCrop),:])
495                 fig1.tight_layout()
496 
497                 ## Plot Video Frame
498                 image = aVideo.get_data(frame)
499                 ax4.axis('off')
500                 ax4.imshow(image[int(vidHeight*tCrop2):int(vidHeight*
    bCrop2),int(vidWidth*lCrop2):int(vidWidth*rCrop2),:])
501                 fig1.tight_layout()
502 
503                 ## Save Video Frame
504                 fig1.canvas.draw()
505                 w,h = fig1.canvas.get_width_height()
506                 alemnisFrame = np.frombuffer(fig1.canvas.tostring_rgb(),
    dtype='uint8')
507                 alemnisFrame.shape = (h, w, 3)
508                 CombinedVideo.append_data(alemnisFrame)
509 
510                 ## Output Time Passed
511                 if (frame-startFrame)%(30*speedMult)/speedMult == 0:
512                     eTime = round(time.time()-sTime,2)
```

```
513                     sTime = time.time()
514                     print('Frame ' + str(int((frame-startFrame)/speedMult)
    ) + ' out of ' +
515                           str(int(nFrames/speedMult)) + ' has been written
     after ' + str(eTime) + ' seconds.')
516
517             plt.close('all')
518             aVideo.close()
519             CombinedVideo.close() #release the newly created video
520             # for f,t in zip([880,932,988,1047],[200,200,200,600]): Beep(f
    ,t) #make some noise
521             print(newFile + ' has been written')
```

Listing C.1: Nanomechanical Fracture Data Analysis

Appendix D

INTERPENETRATING LATTICE DESIGN

To fabricate lattices with precise feature sizes that survive the oxygen etching, codes were developed to print latticed using both the piezo and galvo modes on the Nanoscribe. In the piezo mode, writing can be done in three dimensions and hence a helical laser trajectory was chosen to write lattices where struts are fully crosslinked. The print speed in this is really slow, often leading to over 6 hrs for a 24 um * 48 um* 200 um part. Hence, a galvo code was also developed in which only 2D layer by layer writing is possible, but is almost 50 times faster.

```
def power_adj(structure, x, y, z, power):
    '''

    Parameters
    ----------
    structure: list of structure lines
        DESCRIPTION: input the list that needs to have laser power
   adjustment
    x (range) : list [x1,x2] or multiple ranges [[x1,x2],[x3,x4]]
        DESCRIPTION: range over the x values
    y (range) : list [y1,y2] or multiple ranges [[y1,y2],[y3,y4]]
        DESCRIPTION: range over the y values
    z (range) : list [z1,z2] or multiple ranges [[z1,z2],[z3,z4]]
        DESCRIPTION: range over the z values
    power : integer
```

```
15          DESCRIPTION: laser power value
16
17      Returns
18      -------
19      list of new power adjusted lines of structure
20
21      '''
22      counter = 0
23      new_structure = [] #new power added list of the lines of the structure
24      for i in structure:
25          counter +=1
26
27          if type(x[0]) != list: # check if only one range is given
28
29              if x[0]<=i[0][0]<=x[1] and y[0]<=i[0][1]<=y[1] and z[0]<=i
    [0][2]<=z[1]: #check for each line if it falls under the range
30                  new_structure.append([[i[0][0], i[0][1], i[0][2], power],
    [i[1][0], i[1][1], i[1][2], power]]) # add 4th value of power
31
32              else:                                   # if the line is outside
    range, then do not change or add anything
33                  new_structure.append(i)
34
35
36          else:                                       # this is for multiple
    ranges
37              for j in range(len(x)):
38
39                  if x[j][0]<=i[0][0]<=x[j][1] and y[j][0]<=i[0][1]<=y[j][1]
     and z[j][0]<=i[0][2]<=z[j][1]:
```

```
                    new_structure.append([[i[0][0], i[0][1], i[0][2],
    power], [i[1][0], i[1][1], i[1][2], power]])
                    break #break the j for loop to prevent lines falling
    under multiple ranges to be duplicated

            if counter > len(new_structure): # if the line does not fall
    under any range
                new_structure.append(i)


     return new_structure
```

Listing D.1: Piezo power adjustment

```
def Lattice_crack(Lattice,a, w, ycenter, zheight):
    Newlattice = []
    for j,S in enumerate(Lattice):
        for k in S:
            # print(k[1], ycenter-w/2, ycenter+w/2)
            if (k[1]<(ycenter-w/2)) or (k[1]>(ycenter+w/2)):
                if S not in Newlattice:
                    Newlattice.append(S)
                    # print(j,S)
            if ((ycenter-w/2)<k[1]) or (k[1]<(ycenter+w/2)):
                if k[2]>=(zheight+a):
                    if S not in Newlattice:
                        Newlattice.append(S)
                        # print (j,S)
    for j,S in enumerate(Newlattice):
        for k in S:
            if ((ycenter-0.5)<k[1]<(ycenter+0.5)):
```

```
                if k[2]<(zheight+a):
                    if S in Newlattice:
                        Newlattice.remove(S)
                        # print (j,S)
    for j,S in enumerate(Newlattice):
        for k in S:
            if k[1]==ycenter:
                if k[2]<(zheight+a):
                    if S in Newlattice:
                        Newlattice.remove(S)
    return(Newlattice)
```

Listing D.2: IPL crack

```
### IPL Lattice
if Choosebeamtype == 'IPL':
    helices_IPL =[]
    finalhelix_IPL =[]
    UCbeam_IPL,Bravbeam_IPL,Vertbeam_IPL = UC_IPL(W_latticebeam_OC,
   W_latticebeam_RD)
    Structure_latticebeam_IPL = Lattice(UCbeam_IPL, X_latticebeam_IPL,
   crop_IPL, Bravbeam_IPL)
    for i in range(len(Structure_latticebeam_IPL)):
        for j in range(2):
            Structure_latticebeam_IPL[i][j][0] = Structure_latticebeam_IPL
   [i][j][0]+cx_latticebeam_IPL
            Structure_latticebeam_IPL[i][j][1] = Structure_latticebeam_IPL
   [i][j][1]+cy_latticebeam_IPL
            Structure_latticebeam_IPL[i][j][2] = Structure_latticebeam_IPL
   [i][j][2]+cz_latticebeam_IPL
      ## IPL Lattice crack
```

```
13      latticewithcrack_IPL = Lattice_crack_IPL(Structure_latticebeam_IPL,
    a_IPL, w_IPL, Width_latticebeam_IPL*W_latticebeam_OC/2+
    cy_latticebeam_IPL,cz_latticebeam_IPL)
14
15        ## Creating Helical Laser Path in IPL Lattice
16      for S in latticewithcrack_IPL: #Structure_latticebeam_IPL:#
17          if S[0][1]==S[1][1]:
18              ISpring = IellipticalHelix(ay_IPL,ax_IPL,p_IPL,points_IPL,S
    [0],S[1])
19              helices_IPL.append(ISpring)
20          else:
21              ISpring = IellipticalHelix(ax_IPL,ay_IPL,p_IPL,points_IPL,S
    [0],S[1])
22              helices_IPL.append(ISpring)
23      for i,S in enumerate(helices_IPL):
24          for j,a in enumerate(S):
25              finalhelix_IPL.append(a)
26      Final_beam_IPL = Structure_pad1 + Structure_pad2 + finalhelix_IPL +
    Structure_pad3 ##
27
28
29  if Choosebeamtype == 'IPL':
30      x_start = cx_latticebeam_IPL
31      y_start = cy_latticebeam_IPL
32      z_start = cz_latticebeam_IPL
33
34  shell_thickness = (Unitcellsize /2)+0.5
35  w = Width_beam
36  l = Length_beam
37  h = Height_beam
```

```
38
39 x_end = x_start+l
40 y_end = y_start+w
41 z_end = z_start+h
42
43 side_left = [[x_start-5, x_start+shell_thickness],[y_start-5, y_end+5], [
       z_start-5, z_end+5]]
44 side_right = [[x_end - shell_thickness, x_end+5],[y_start-5, y_end+5], [
       z_start-5, z_end+5]]
45 side_top = [[x_start-5, x_end+5],[y_end - shell_thickness, y_end+5], [
       z_start-5, z_end+5]]
46 side_bottom = [[x_start-5, x_end+5],[y_start-5, y_start + shell_thickness
       ], [z_start-5, z_end+5]]
47 side_upper = [[x_start-5, x_end+5],[y_start-5, y_end+5], [z_end -
       shell_thickness, z_end+5]]
48 side_lower = [[x_start-5, x_end+5],[y_start-5, y_end+5], [z_start-5,
       z_start + shell_thickness]]
49
50 if Choosebeamtype == 'IPL':
51     IPL_final = power_adj(Final_beam_IPL,[side_lower[0],side_left[0],
       side_top[0],side_right[0],side_bottom[0],side_upper[0]],[side_lower[1],
       side_left[1],side_top[1],side_right[1],side_bottom[1],side_upper[1]],[
       side_lower[2],side_left[2],side_top[2],side_right[2],side_bottom[2],
       side_upper[2]], LPshell)
```

Listing D.3: Helical lattice write for IPL

BIBLIOGRAPHY

[1] Joanna Aizenberg, James C Weaver, Monica S Thanawala, Vikram C Sundar, Daniel E Morse, and Peter Fratzl. Skeleton of euplectella sp.: structural hierarchy from the nanoscale to the macroscale. *Science*, 309(5732):275–278, 2005.

[2] Almut Albiez and Ruth Schwaiger. Size effect on the strength and deformation behavior of glassy carbon nanopillars. *Mrs Advances*, 4(2):133–138, 2019.

[3] Markus Alfreider, Darjan Kozic, Otmar Kolednik, and Daniel Kiener. In-situ elastic-plastic fracture mechanics on the microscale by means of continuous dynamical testing. *Materials and Design*, 148:177–187, jun 2018.

[4] AS Argon and RE Cohen. Toughenability of polymers. *Polymer*, 44(19):6013–6032, 2003.

[5] Akash Arora, Tzyy-Shyang Lin, Haley K Beech, Hidenobu Mochigase, Rui Wang, and Bradley D Olsen. Fracture of polymer networks containing topological defects. *Macromolecules*, 53(17):7346–7355, 2020.

[6] EJAM Arzt. Size effects in materials due to microstructural and dimensional constraints: a comparative review. *Acta materialia*, 46(16):5611–5626, 1998.

[7] Michael F Ashby and RF Medalist. The mechanical properties of cellular solids. *Metallurgical Transactions A*, 14(9):1755–1769, 1983.

[8] Johannes Ast, Matteo Ghidelli, Karsten Durst, Mathias Göken, Marco Sebastiani, and Alexander M Korsunsky. A review of experimental approaches to fracture toughness evaluation at the micro-scale. *Materials & Design*, 173:107762, 2019.

[9] Johannes Ast, Mikhail N Polyakov, Gaurav Mohanty, Johann Michler, and Xavier Maeder. Interplay of stresses, plasticity at crack tips and small sample dimensions revealed by in-situ microcantilever tests in tungsten. *Materials Science and Engineering: A*, 710:400–412, 2018.

[10] Tomas F Babuska, Mark A Wilson, Kyle L Johnson, Shaun R Whetten, John F Curry, Jeffrey M Rodelas, Cooper Atkinson, Ping Lu, Michael Chandross, Brandon A Krick,

et al. Achieving high strength and ductility in traditionally brittle soft magnetic intermetallics via additive manufacturing. *Acta Materialia*, 180:149–157, 2019.

[11] Tommaso Baldacchini, Maxwell Zimmerley, Chun-Hung Kuo, Eric O Potma, and Ruben Zadoyan. Characterization of microstructures fabricated by two-photon polymerization using coherent anti-stokes raman scattering microscopy. *The Journal of Physical Chemistry B*, 113(38):12663–12668, 2009.

[12] F Barthelat and HD Espinosa. An experimental investigation of deformation and fracture of nacre–mother of pearl. *Experimental mechanics*, 47:311–324, 2007.

[13] Francois Barthelat, Jee E Rim, and Horacio D Espinosa. A review on the structure and mechanical properties of mollusk shells–perspectives on synthetic biomimetic materials. *Applied scanning probe methods XIII: biomimetics and industrial applications*, pages 17–44, 2009.

[14] J. Bauer, A. Schroer, R. Schwaiger, and O. Kraft. Approaching theoretical strength in glassy carbon nanolattices. *Nature Materials*, 15(4):438–443, 2016.

[15] Jens Bauer, Anna Guell Izard, Yunfei Zhang, Tommaso Baldacchini, and Lorenzo Valdevit. Programmable mechanical properties of two-photon polymerized materials: From nanowires to bulk. *Advanced Materials Technologies*, 4(9):1900146, 2019.

[16] Jens Bauer, Anna Guell Izard, Yunfei Zhang, Tommaso Baldacchini, and Lorenzo Valdevit. Thermal post-curing as an efficient strategy to eliminate process parameter sensitivity in the mechanical properties of two-photon polymerized materials. *Optics Express*, 28(14):20362–20371, 2020.

[17] Jens Bauer, Lucas R Meza, Tobias A Schaedler, Ruth Schwaiger, Xiaoyu Zheng, and Lorenzo Valdevit. Nanolattices: an emerging class of mechanical metamaterials. *Advanced Materials*, 29(40):1701850, 2017.

[18] Jens Bauer, Almut Schroer, Ruth Schwaiger, and Oliver Kraft. Approaching theoretical strength in glassy carbon nanolattices. *Nature materials*, 15(4):438–443, 2016.

[19] Zdenek P Bažant. Size effect in blunt fracture: concrete, rock, metal. *Journal of engineering mechanics*, 110(4):518–535, 1984.

[20] Zdenek P Bazant. Size effect on structural strength: a review. *Archive of applied Mechanics*, 69:703–725, 1999.

[21] Zdenek P Bazant. Size effect. *International Journal of Solids and Structures*, 37(1-2):69–80, 2000.

[22] Zdeněk P Bažant. Scaling theory for quasibrittle structural failure. *Proceedings of the National Academy of Sciences*, 101(37):13400–13407, 2004.

[23] Zdenek P Bažant and Mohammad T Kazemi. Size effect in fracture of ceramics and its use to determine fracture energy and effective process zone length. *Journal of the American Ceramic Society*, 73(7):1841–1853, 1990.

[24] Zdenek P Bazant and MT Kazemi. Determination of fracture energy, process zone length and brittleness number from size effect, with application to rock and concrete. *International Journal of fracture*, 44:111–131, 1990.

[25] Zdenek P Bažant, Jia-Liang Le, and Marco Salviato. *Quasibrittle fracture mechanics and size effect: a first course*. Oxford University Press, 2021.

[26] Zdeněk P. Bažant and Qiang Yu. Universal size effect law and effect of crack depth on quasi-brittle structure strength. *Journal of Engineering Mechanics*, 135(2):78–84, 2009.

[27] Y Bouligand. Twisted fibrous arrangements in biological materials and cholesteric mesophases. *Tissue and Cell*, 4(2):189–217, 1972.

[28] Y. Bouligand. Twisted fibrous arrangements in biological materials and cholesteric mesophases. *Tissue and Cell*, 4(2):189–217, jan 1972.

[29] Florian Bouville, Eric Maire, Sylvain Meille, Bertrand Van de Moortèle, Adam J Stevenson, and Sylvain Deville. Strong, tough and stiff bioinspired ceramics from brittle constituents. *Nature materials*, 13(5):508–514, 2014.

[30] Florian Bouville, Eric Maire, Sylvain Meille, Bertrand Van De Moortèle, Adam J. Stevenson, and Sylvain Deville. Strong, tough and stiff bioinspired ceramics from brittle constituents. *Nature Materials*, 13(5):508–514, 2014.

[31] HR Brown. A model for brittle-ductile transitions in polymers. *Journal of Materials Science*, 17:469–476, 1982.

[32] J. A. Buckwalter, M. J. Glimcher, R. R. Cooper, and R. Recker. Bone biology. Part I: Structure, blood supply, cells, matrix, and mineralization, jan 1995.

[33] David Z Chen, XW Gu, Qi An, WA Goddard, and Julia R Greer. Ductility and work hardening in nano-sized metallic glasses. *Applied Physics Letters*, 106(6), 2015.

[34] Po-Yu Chen, Albert Yu-Min Lin, Joanna McKittrick, and Marc André Meyers. Structure and mechanical properties of crab exoskeletons. *Acta biomaterialia*, 4(3):587–596, 2008.

[35] Brian Cotterell. The past, present, and future of fracture mechanics. *Engineering fracture mechanics*, 69(5):533–553, 2002.

[36] Ahmad Khayer Dastjerdi, Reza Rabiei, and Francois Barthelat. The weak interfaces within tough natural composites: experiments on three types of nacre. *Journal of the mechanical behavior of biomedical materials*, 19:50–60, 2013.

[37] Gerhard Dehm, Balila Nagamani Jaya, Rejin Raghavan, and Christoph Kirchlechner. Overview on micro-and nanomechanical testing: New insights in interface plasticity and fracture at small length scales. *Acta Materialia*, 142:248–282, 2018.

[38] Sheila Devasahayam and Chaudhery Mustansar Hussain. Thin-film nanocomposite devices for renewable energy current status and challenges. *Sustainable Materials and Technologies*, 26:e00233, 2020.

[39] Aaliyah Z Dookhith, Nathaniel A Lynd, and Gabriel E Sanoja. Tailoring rate and temperature-dependent fracture of polyether networks with organoaluminum catalysts. *Macromolecules*, 56(1):40–48, 2022.

[40] QQ Duan, RT Qu, P Zhang, ZJ Zhang, and ZF Zhang. Intrinsic impact toughness of relatively high strength alloys. *Acta Materialia*, 142:226–235, 2018.

[41] ASTM E1820-18. Standard test method for measurement of fracture toughness. Technical report, 2011.

[42] Franz Dieter Fischer, Otmar Kolednik, Jozef Predan, Hajar Razi, and Peter Fratzl. Crack driving force in twisted plywood structures. *Acta biomaterialia*, 55:349–359, 2017.

[43] Peter Fratzl, Himadri S Gupta, Franz Dieter Fischer, and Otmar Kolednik. Hindered crack propagation in materials with periodically varying young's modulus—lessons from biological materials. *Advanced Materials*, 19(18):2657–2661, 2007.

[44] H. Gao, B. Ji, I. L. Jager, E. Arzt, and P. Fratzl. Materials become insensitive to flaws at nanoscale: Lessons from nature. *Proceedings of the National Academy of Sciences*, 100(10):5597–5600, 2003.

[45] Lorna J Gibson. Cellular solids. *Mrs Bulletin*, 28(4):270–274, 2003.

[46] Jiseok Gim, Noah Schnitzer, Laura M Otter, Yuchi Cui, Sébastien Motreuil, Frédéric Marin, Stephan E Wolf, Dorrit E Jacob, Amit Misra, and Robert Hovden. Nanoscale deformation mechanics reveal resilience in nacre of pinna nobilis shell. *Nature communications*, 10(1):1–8, 2019.

[47] Rubayn Goh, Scott PO Danielsen, Eric Schaible, Robert M McMeeking, and J Herbert Waite. Nanolatticed architecture mitigates damage in shark egg cases. *Nano letters*, 21(19):8080–8085, 2021.

[48] Julia R Greer and Jeff Th M De Hosson. Plasticity in small-sized metallic systems: Intrinsic versus extrinsic size effect. *Progress in Materials Science*, 56(6):654–724, 2011.

[49] Alan Arnold Griffith. Vi. the phenomena of rupture and flow in solids. *Philosophical transactions of the royal society of london. Series A, containing papers of a mathematical or physical character*, 221(582-593):163–198, 1921.

[50] Alan Arnold Griffith. The theory of rupture. *Proceedings of the First International Congress of Applied Mechanics: Technische Boekhandel en Drukkerij*, pages 55–63, 1924.

[51] Andrew J Gross and Katia Bertoldi. Additive manufacturing of nanostructures that are delicate, complex, and smaller than ever. *Small*, 15(33):1902370, 2019.

[52] Lessa Kay Grunenfelder, Steven Herrera, and David Kisailus. Crustacean-derived biomimetic components and nanostructured composites. *Small*, 10(16):3207–3232, 2014.

[53] Grace X Gu, Mahdi Takaffoli, and Markus J Buehler. Hierarchically enhanced impact resistance of bioinspired composites. *Advanced Materials*, 29(28):1700060, 2017.

[54] GV Guinea, JY Pastor, J Planas, and M Elices. Stress intensity factor, compliance and cmod for a general three-point-bend beam. *International Journal of Fracture*, 89:103–116, 1998.

[55] Fahmy M Haggag and John H Underwood. Compliance of a three-point bend specimen at load line. *International Journal of Fracture*, 26, 1984.

[56] Peter Bernhard Hirsch, SG Roberts, and J Samuels. The brittle-ductile transition in silicon. ii. interpretation. *Proceedings of the Royal Society of London. A. Mathematical and Physical Sciences*, 421(1860):25–53, 1989.

[57] Christian G Hoover and Zdeněk P Bažant. Comprehensive concrete fracture tests: size effects of types 1 & 2, crack length effect and postpeak. *Engineering Fracture Mechanics*, 110:281–289, 2013.

[58] Wei Huang, David Restrepo, Jae-Young Jung, Frances Y Su, Zengqian Liu, Robert O Ritchie, Joanna McKittrick, Pablo Zavattieri, and David Kisailus. Multiscale toughening mechanisms in biological materials and bioinspired designs. *Advanced Materials*, 31(43):1901561, 2019.

[59] ASTM International. *Standard test method for measurement of fracture toughness*. ASTM International, 2011.

[60] ASTM International. *Standard test method for core shear properties of sandwich constructions by beam flexure*. ASTM international, 2016.

[61] GR Irwin. Fracturing of metals. *ASM, Cleveland*, 147(19-9), 1948.

[62] Scott G Isaacson, Krystelle Lionti, Willi Volksen, Teddie P Magbitang, Yusuke Matsuda, Reinhold H Dauskardt, and Geraud Dubois. Fundamental limits of material toughening in molecularly confined polymers. *Nature materials*, 15(3):294–298, 2016.

[63] Inas Issa, Christoph Gammer, Stefan Kolitsch, Anton Hohenwarter, Peter J Imrich, Reinhard Pippan, and Daniel Kiener. In-situ tem investigation of toughening in silicon at small scales. *Materials today*, 48:29–37, 2021.

[64] Dongchan Jang, Lucas R Meza, Frank Greer, and Julia R Greer. Fabrication and deformation of three-dimensional hollow ceramic nanostructures. *Nature materials*, 12(10):893–898, 2013.

[65] Balila Nagamani Jaya, Christoph Kirchlechner, and Gerhard Dehm. Can microscale fracture tests provide reliable fracture toughness values? a case study in silicon. *Journal of Materials Research*, 30(5):686–698, 2015.

[66] Anastasiya V Kazantseva, Elena A Chernykh, Cameron Crook, Evan P Garcia, Dmitry A Fishman, Eric O Potma, Lorenzo Valdevit, Sergey S Kharintsev, and Tommaso Baldacchini. Nanoscale investigation of two-photon polymerized microstructures with tip-enhanced raman spectroscopy. *Journal of Physics: Photonics*, 3(2):024001, 2021.

[67] Ghennadiy Vsevolodovich Klevtsov, Ludmila Rafailovna Botvina, and Natal'ya Arturovna Klevtsova. Plastic zones formation under different types of loading conditions. *ISIJ international*, 36(2):215–221, 1996.

[68] Otmar Kolednik, J Predan, Franz Dieter Fischer, and P Fratzl. Improvements of strength and fracture resistance by spatial material property variations. *Acta materialia*, 68:279–294, 2014.

[69] SK Kudari, B Maiti, and KK Ray. The effect of specimen geometry on plastic zone size: a study using the j integral. *The Journal of Strain Analysis for Engineering Design*, 42(3):125–136, 2007.

[70] GJ Lake and AG Thomas. The strength of highly elastic materials. *Proceedings of the Royal Society of London. Series A. Mathematical and Physical Sciences*, 300(1460):108–119, 1967.

[71] Maximilien E Launey, Markus J Buehler, and Robert O Ritchie. On the mechanistic origins of toughness in bone. *Annual review of materials research*, 40:25–53, 2010.

[72] Maximilien E Launey, P-Y Chen, J McKittrick, and RO Ritchie. Mechanistic aspects of the fracture toughness of elk antler bone. *Acta biomaterialia*, 6(4):1505–1514, 2010.

[73] Kwang-Sup Lee, Ran Hee Kim, Dong-Yol Yang, and Sang Hu Park. Advances in 3d nano/microfabrication using two-photon initiated polymerization. *Progress in Polymer Science*, 33(6):631–681, 2008.

[74] L. H. Lee, J. F. Mandell, and F. J. McGarry. Fracture toughness and crack instability in tough polymers under plane strain conditions. *Polymer Engineering & Science*, 27(15):1128–1136, 1987.

[75] D. Leguillon and R. Piat. Fracture of porous materials - Influence of the pore size. *Engineering Fracture Mechanics*, 75(7):1840–1853, 2008.

[76] Torben Lenau and Michael Barfoed. Colours and metallic sheen in beetle shells—a biomimetic search for material structuring principles causing light interference. *Advanced Engineering Materials*, 10(4):299–314, 2008.

[77] Guodong Li, Qi An, Bo Duan, Leah Borgsmiller, Muath Al Malki, Matthias Agne, Umut Aydemir, Pengcheng Zhai, Qingjie Zhang, Sergey I Morozov, et al. Fracture toughness of thermoelectric materials. *Materials Science and Engineering: R: Reports*, 144:100607, 2021.

[78] Flavia Libonati and Markus J. Buehler. Advanced Structural Materials by Bioinspiration. *Advanced Engineering Materials*, 19(5), 2017.

[79] Flavia Libonati, Grace X Gu, Zhao Qin, Laura Vergani, and Markus J Buehler. Bone-inspired materials by design: toughness amplification observed using 3d printing and testing. *Advanced Engineering Materials*, 18(8):1354–1363, 2016.

[80] Flavia Libonati, Grace X. Gu, Zhao Qin, Laura Vergani, and Markus J. Buehler. Bone-Inspired Materials by Design: Toughness Amplification Observed Using 3D Printing and Testing. *Advanced Engineering Materials*, 18(8):1354–1363, 2016.

[81] Shaoting Lin, Jiahua Ni, Dongchang Zheng, and Xuanhe Zhao. Fracture and fatigue of ideal polymer networks. *Extreme Mechanics Letters*, 48:101399, 2021.

[82] Binghe Liu, Yikai Jia, Chunhao Yuan, Lubing Wang, Xiang Gao, Sha Yin, and Jun Xu. Safety issues and mechanisms of lithium-ion battery cell upon mechanical abusive loading: A review. *Energy Storage Materials*, 24:85–112, 2020.

[83] Shoji Maruo, Osamu Nakamura, and Satoshi Kawata. Three-dimensional microfabrication with two-photon-absorbed photopolymerization. *Optics letters*, 22(2):132–134, 1997.

[84] Cory Hage Mefford, Yao Qiao, and Marco Salviato. Failure behavior and scaling of graphene nanocomposites. *Composite Structures*, 176:961–972, 2017.

[85] Lorenzo Mencattelli and Silvestre T. Pinho. Realising bio-inspired impact damage-tolerant thin-ply CFRP Bouligand structures via promoting diffused sub-critical helicoidal damage. *Composites Science and Technology*, 182(April), 2019.

[86] Lorenzo Mencattelli and Silvestre T Pinho. Herringbone-bouligand cfrp structures: a new tailorable damage-tolerant solution for damage containment and reduced delaminations. *Composites Science and Technology*, 190:108047, 2020.

[87] Lucas R. Meza, Satyajit Das, and Julia R. Greer. Strong, lightweight, and recoverable three-dimensional ceramic nanolattices. *Science*, 345(6202):1322–1326, sep 2014.

[88] Lucas R Meza, Satyajit Das, and Julia R Greer. Strong, lightweight, and recoverable three-dimensional ceramic nanolattices. *Science*, 345(6202):1322–1326, 2014.

[89] Lucas R. Meza, Alex J. Zelhofer, Nigel Clarke, Arturo J. Mateos, Dennis M. Kochmann, and Julia R. Greer. Resilient 3D hierarchical architected metamaterials. *Proceedings of the National Academy of Sciences of the United States of America*, 112(37):11502–11507, 2015.

[90] He Ming-Yuan and John W Hutchinson. Crack deflection at an interface between dissimilar elastic materials. *International journal of solids and structures*, 25(9):1053–1067, 1989.

[91] M Mirkhalaf, A Khayer Dastjerdi, and F Barthelat. Overcoming the brittleness of glass through bio-inspiration and micro-architecture. *Nature communications*, 5(1):1–9, 2014.

[92] Mohammad Mirkhalaf, Tao Zhou, and Francois Barthelat. Simultaneous improvements of strength and toughness in topologically interlocked ceramics. *Proceedings of the National Academy of Sciences*, 115(37):9128–9133, 2018.

[93] Chengyang Mo and Jordan R Raney. Spatial programming of defect distributions to enhance material failure characteristics. *Extreme Mechanics Letters*, 34:100598, 2020.

[94] L. C. Montemayor, W. H. Wong, Y. W. Zhang, and J. R. Greer. Insensitivity to Flaws Leads to Damage Tolerance in Brittle Architected Meta-Materials. *Scientific Reports*, 6(January):1–9, 2016.

[95] Etienne Munch, Maximimilan E Launey, Daan H Alsem, Eduardo Saiz, Antoni P Tomsia, and Robert O Ritchie. Tough, bio-inspired hybrid materials. *Science*, 322(5907):1516–1520, 2008.

[96] Steven E. Naleway, Michael M. Porter, Joanna McKittrick, and Marc A. Meyers. Structural Design Elements in Biological Materials: Application to Bioinspiration. *Advanced Materials*, 27(37):5455–5476, 2015.

[97] Steven E Naleway, Michael M Porter, Joanna McKittrick, and Marc A Meyers. Structural design elements in biological materials: application to bioinspiration. *Advanced materials*, 27(37):5455–5476, 2015.

[98] Hoang T Nguyen, A Abdullah Dönmez, and Zdeněk P Bažant. Structural strength scaling law for fracture of plastic-hardening metals and testing of fracture properties. *Extreme Mechanics Letters*, 43:101141, 2021.

[99] M Niinomi and M Nakai. Biomedical implant devices fabricated from low young's modulus titanium alloys demonstrating high mechanical biocompatibility. *Mater Matters*, 9:39–46, 2014.

[100] Svetoslav Nikolov, Michal Petrov, Liverios Lymperakis, Martin Friák, Christoph Sachs, Helge Otto Fabritius, Dierk Raabe, and Jörg Neugebauer. Revealing the design principles of high-performance biological composites using Ab initio and multiscale simulations: The example of lobster cuticle. *Advanced Materials*, 22(4):519–526, jan 2010.

[101] Takayuki Nonoyama and Jian Ping Gong. Tough double network hydrogel and its biomedical applications. *Annual review of chemical and biomolecular engineering*, 12:393–410, 2021.

[102] Anar Nurizada and Kedar Kirane. Induced anisotropy in the fracturing behavior of 3d printed parts analyzed by the size effect method. *Engineering Fracture Mechanics*, 239:107304, 2020.

[103] Egon Orowan. Notch, brittleness and the strength of metals. 1945.

[104] Fredrik Östlund, Karolina Rzepiejewska-Malyska, Klaus Leifer, Lucas M Hale, Yuye Tang, Roberto Ballarini, William W Gerberich, and Johann Michler. Brittle-to-ductile transition in uniaxial compression of silicon pillars at room temperature. *Advanced Functional Materials*, 19(15):2439–2444, 2009.

[105] IA Ovid'Ko, RZ Valiev, and YT Zhu. Review on superior strength and enhanced ductility of metallic nanomaterials. *Progress in materials science*, 94:462–540, 2018.

[106] SN Patek, , and RL Caldwell. Extreme impact and cavitation forces of a biological hammer: strike forces of the peacock mantis shrimp odontodactylus scyllarus. *Journal of Experimental Biology*, 208(19):3655–3664, 2005.

[107] Zainab S Patel, Abdulaziz O Alrashed, Kush Dwivedi, Marco Salviato, and Lucas R Meza. Rethinking ductility—a study into the size-affected fracture of additively manufactured polymers. *Additive Manufacturing*, 84:104113, 2024.

[108] Zainab S Patel and Lucas R Meza. Toughness amplification via controlled nanostructure in lightweight nano-bouligand materials. *Small*, 2207779, 2023.

[109] R. Pippan, S. Wurster, and D. Kiener. Fracture mechanics of micro samples: Fundamental considerations. *Materials & Design*, 159:252–267, dec 2018.

[110] Reinhard Pippan, Stefan Wurster, and Daniel Kiener. Fracture mechanics of micro samples: Fundamental considerations. *Materials & Design*, 159:252–267, 2018.

[111] Carlos M Portela, A Vidyasagar, Sebastian Krödel, Tamara Weissenbach, Daryl W Yee, Julia R Greer, and Dennis M Kochmann. Extreme mechanical resilience of self-assembled nanolabyrinthine materials. *Proceedings of the National Academy of Sciences*, 117(11):5686–5693, 2020.

[112] J. William Pro and Francois Barthelat. Is the Bouligand architecture tougher than regular cross-ply laminates? A discrete element method study. *Extreme Mechanics Letters*, 41:101042, nov 2020.

[113] Yao Qiao and Marco Salviato. Strength and cohesive behavior of thermoset polymers at the microscale: A size-effect study. *Engineering Fracture Mechanics*, 213:100–117, 2019.

[114] Yao Qiao and Marco Salviato. Micro-computed tomography analysis of damage in notched composite laminates under multi-axial fatigue. *Composites Part B: Engineering*, 187:107789, 2020.

[115] Luca Quagliato, Soo Yeon Kim, and Seok Chang Ryu. Quasi-ductile to brittle transitional behavior and material properties gradient for additively manufactured sla acrylate. *Materials Letters*, 329:133121, 2022.

[116] Nicolas Rauner, Monika Meuris, Mirjana Zoric, and Joerg C Tiller. Enzymatic mineralization generates ultrastiff and tough hydrogels with tunable mechanics. *Nature*, 543(7645):407–410, 2017.

[117] James R Rice. A path independent integral and the approximate analysis of strain concentration by notches and cracks. 1968.

[118] James R Rice and GF0166 Rosengren. Plane strain deformation near a crack tip in a power-law hardening material. *Journal of the Mechanics and Physics of Solids*, 16(1):1–12, 1968.

[119] Robert O Ritchie. The conflicts between strength and toughness. *Nature materials*, 10(11):817–822, 2011.

[120] Jesus Rivera, Maryam Sadat Hosseini, David Restrepo, Satoshi Murata, Drago Vasile, Dilworth Y Parkinson, Harold S Barnard, Atsushi Arakaki, Pablo Zavattieri, and David Kisailus. Toughening mechanisms of the elytra of the diabolical ironclad beetle. *Nature*, 586(7830):543–548, 2020.

[121] Ashley M Roach, Benjamin C White, Anthony Garland, Bradley H Jared, Jay D Carroll, and Brad L Boyce. Size-dependent stochastic tensile properties in additively manufactured 316l stainless steel. *Additive Manufacturing*, 32:101090, 2020.

[122] Marco Salviato. Adding multi-material regions embracing the tip leads to significant capacity increase in structures weakened by v-notches under antiplane shear and torsion. *International Journal of Solids and Structures*, 250:111704, 2022.

[123] Ashish Kumar Saxena, Steffen Brinckmann, Bernhard Völker, Gerhard Dehm, and Christoph Kirchlechner. Experimental conditions affecting the measured fracture toughness at the microscale: Notch geometry and crack extension measurement. *Materials & Design*, 191:108582, jun 2020.

[124] Ashish Kumar Saxena, Steffen Brinckmann, Bernhard Völker, Gerhard Dehm, and Christoph Kirchlechner. Experimental conditions affecting the measured fracture toughness at the microscale: Notch geometry and crack extension measurement. *Materials & Design*, 191:108582, 2020.

[125] Authors Angkur Shaikeea, Huachen Cui, Mark O Masta, and Xiaoyu Rayne Zheng. Mechanical metamaterials: does toughness characterize fracture?

[126] Dahye Shin and Dongchan Jang. Crack-tip plasticity and intrinsic toughening in nano-sized brittle amorphous carbon. *International Journal of Plasticity*, 127:102642, 2020.

[127] Nobphadon Suksangpanya, Nicholas A. Yaraghi, David Kisailus, and Pablo Zavattieri. Twisting cracks in Bouligand structures. *Journal of the Mechanical Behavior of Biomedical Materials*, 76(June):38–57, 2017.

[128] Nobphadon Suksangpanya, Nicholas A Yaraghi, R Byron Pipes, David Kisailus, and Pablo Zavattieri. Crack twisting and toughening strategies in bouligand architectures. *International Journal of Solids and Structures*, 150:83–106, 2018.

[129] Ottman A Tertuliano, Bryce W Edwards, Lucas R Meza, Vikram S Deshpande, and Julia R Greer. Nanofibril-mediated fracture resistance of bone. *Bioinspiration & Biomimetics*, 16(3):035001, 2021.

[130] Ottman A Tertuliano and Julia R Greer. The nanocomposite nature of bone drives its strength and damage resistance. *Nature materials*, 15(11):1195–1202, 2016.

[131] S Wang, Y Yang, Li Min Zhou, and Y-W Mai. Size effect in microcompression of epoxy micropillars. *Journal of materials science*, 47(16):6047–6055, 2012.

[132] Shi-Qing Wang, Shiwang Cheng, Panpan Lin, and Xiaoxiao Li. A phenomenological molecular model for yielding and brittle-ductile transition of polymer glasses. *The Journal of chemical physics*, 141(9):094905, 2014.

[133] James C Weaver, Garrett W Milliron, Ali Miserez, Kenneth Evans-Lutterodt, Steven Herrera, Isaias Gallana, William J Mershon, Brook Swanson, Pablo Zavattieri, Elaine DiMasi, et al. The stomatopod dactyl club: a formidable damage-tolerant biological hammer. *Science*, 336(6086):1275–1280, 2012.

[134] Ulrike G.K. Wegst, Hao Bai, Eduardo Saiz, Antoni P. Tomsia, and Robert O. Ritchie. Bioinspired structural materials. *Nature Materials*, 14(1):23–36, 2015.

[135] Benjamin C White, Anthony Garland, Ryan Alberdi, and Brad L Boyce. Interpenetrating lattices with enhanced mechanical functionality. *Additive Manufacturing*, 38:101741, 2021.

[136] Benjamin C White, Anthony Garland, and Brad L Boyce. Toughening by interpenetrating lattices. *Matter*, 6(2):570–582, 2023.

[137] Jinrong Wu, Zhao Qin, Liangliang Qu, Hao Zhang, Fei Deng, and Ming Guo. Natural hydrogel in american lobster: A soft armor with high toughness and strength. *Acta Biomaterialia*, 88:102–110, 2019.

[138] Kaijin Wu, Zhaoqiang Song, Shuaishuai Zhang, Yong Ni, Shengqiang Cai, Xinglong Gong, Linghui He, and Shu-Hong Yu. Discontinuous fibrous bouligand architecture enabling formidable fracture resistance with crack orientation insensitivity. *Proceedings of the National Academy of Sciences*, 117(27):15465–15472, 2020.

[139] Souheng Wu. Control of intrinsic brittleness and toughness of polymers and blends by chemical structure: a review. *Polymer International*, 29(3):229–247, 1992.

[140] Stefan Wurster, Christian Motz, and Reinhard Pippan. Characterization of the fracture toughness of micro-sized tungsten single crystal notched specimens. *Philosophical Magazine*, 92(14):1803–1825, 2012.

[141] Xiaoxing Xia, Christopher M Spadaccini, and Julia R Greer. Responsive materials architected in space and time. *Nature Reviews Materials*, 7(9):683–701, 2022.

[142] Fei Xie, Qingjun Chen, and Jiwen Gao. Brittle-ductile transition in laser 3d printing of fe-based bulk metallic glass composites. *Metals*, 9(1):78, 2019.

[143] Shanshan Xu, Jean-Francois Tahon, Isabelle De-Waele, Grégory Stoclet, and Valerie Gaucher. Brittle-to-ductile transition of pla induced by macromolecular orientation. *eXPRESS Polymer Letters*, 14(11):1037–1047, 2020.

[144] Nicholas A. Yaraghi, Nicolás Guarín-Zapata, Lessa K. Grunenfelder, Eric Hintsala, Sanjit Bhowmick, Jon M. Hiller, Mark Betts, Edward L. Principe, Jae Young Jung, Leigh Sheppard, Richard Wuhrer, Joanna McKittrick, Pablo D. Zavattieri, and David Kisailus. A Sinusoidally Architected Helicoidal Biocomposite. *Advanced Materials*, 28(32):6835–6844, 2016.

[145] Sha Yin, Haoyu Chen, Ruiheng Yang, Qinghao He, Dianhao Chen, Lin Ye, Yiu-Wing Mai, Jun Xu, and Robert O Ritchie. Tough nature-inspired helicoidal composites with printing-induced voids. *Cell Reports Physical Science*, 1(7):100109, 2020.

[146] Sheng Yin, Wen Yang, Junpyo Kwon, Amy Wat, Marc A Meyers, and Robert O Ritchie. Hyperelastic phase-field fracture mechanics modeling of the toughening induced by bouligand structures in natural materials. *Journal of the Mechanics and Physics of Solids*, 131:204–220, 2019.

[147] Xuan Zhang, Andrey Vyatskikh, Huajian Gao, Julia R Greer, and Xiaoyan Li. Lightweight, flaw-tolerant, and ultrastrong nanoarchitected carbon. *Proceedings of the National Academy of Sciences*, 116(14):6665–6672, 2019.

[148] Xuan Zhang, Lei Zhong, Arturo Mateos, Akira Kudo, Andrey Vyatskikh, Huajian Gao, Julia R Greer, and Xiaoyan Li. Theoretical strength and rubber-like behaviour in micro-sized pyrolytic carbon. *Nature nanotechnology*, 14(8):762–769, 2019.

[149] SN Zhurkov and VE Korsukov. Atomic mechanism of fracture of solid polymers. *Journal of Polymer Science: Polymer Physics Edition*, 12(2):385–398, 1974.

[150] Yu Zou, Pawel Kuczera, Alla Sologubenko, Takashi Sumigawa, Takayuki Kitamura, Walter Steurer, and Ralph Spolenak. Superior room-temperature ductility of typically brittle quasicrystals at small sizes. *Nature communications*, 7(1):12261, 2016.